9. SITE 933[1]

Shipboard Scientific Party[2]

HOLE 933A

Date occupied: 12 April 1994

Date departed: 15 April 1994

Time on hole: 2 days, 18 hr, 15 min

Position: 5°5.801′N, 46°48.738′W

Bottom felt (drill pipe measurement from rig floor, m): 3376.8

Distance between rig floor and sea level (m): 10.90

Water depth (drill pipe measurement from sea level, m): 3365.9

Penetration (m): 254.20

Number of cores (including cores having no recovery): 27

Total length of cored section (m): 254.20

Total core recovered (m): 177.38

Core recovery (%): 69

Oldest sediment cored:
Depth (mbsf): 254.20
Nature: Silty clay
Earliest age: Pleistocene

Principal results: Site 933 (near proposed Site AF-9) is located on the eastern part of the Amazon Fan, on the eastern levee flank of the Yellow Channel-levee System, about 4 km from the channel. The site was intended to resample microfossil-rich sediment on the crest of the Bottom Levee Complex first sampled at Site 931. Site 933 also provided an opportunity to log the debris-flow interval that was not logged at Site 931 because of hole conditions. The site was selected from crossing seismic-reflection profiles (1943/10 April and 0242/11 April) from the *JOIDES Resolution* pre-site survey.

Hole 933A was cored by APC to 91.2 mbsf, then by XCB to 254.2 mbsf, with total hole recovery of 177.59 m (69.9%). ADARA temperature measurements were made at 53 and 82 mbsf, yielding a geothermal gradient of 46°/km. There was gas expansion in many cores. Methane was found throughout the hole; no higher molecular-weight hydrocarbons were detected.

Four lithologic units are recognized:

Unit I (0–0.52 mbsf) is an intensely bioturbated Holocene nannofossil-foraminifer clay, with about 50% carbonate.

Unit II (0.52–97.62 mbsf) consists of mud with interbedded laminae and beds of silt and very fine sand. Subunit IIA (0.52–14.35 mbsf) comprises moderately bioturbated and color-banded mud. Carbonate content ranges from 0.3% to 10.6%. This subunit is correlated with the Amazon to Blue Channel-levee systems. Subunit IIB (14.35–97.62 mbsf) consists of mud with thin beds of silt and fine sand. Several intervals with abundant silt and sand laminae and thin beds alternate with intervals, 3–8 m thick, of moderately bioturbated mud with only a few silt laminae. At 60–64 mbsf, a massive black clay contains abundant plant detritus, shell fragments, bathyal benthic foraminifers and rounded quartz sand grains. The section to 70 mbsf is correlated with the levee flank of the Yellow Channel-levee System, whereas the lower part of Subunit IIB corresponds to the levees of Channel-levee Systems 5 and 6.

Unit III (99.80–167.31 mbsf) consists of various types of overconsolidated mud, commonly showing deformational structures. The unit is interpreted as a mass-flow deposit comprising large deformed blocks of mud. Benthic foraminifers indicate a source for the blocks on the continental slope.

Unit IV (167.31–249.72 mbsf) consists of a sequence similar to Subunits IIA and IIB, forming the upper part of the levee cored at the bottom of Site 931. Bioturbated mud (Subunit IVA, to 179.03 mbsf) overlies mud with silt laminae and fine sand beds (Subunit IVB), which form a fining- and thinning-upward sequence of turbidites. The resistivity log showed a zone of anomalously low resistivity from the top of the unit to 190 mbsf, corresponding to a 1.2° borehole temperature anomaly and minor pore-water anomalies.

Foraminifers are few in Subunit IIA and rare in Subunit IIB. The Lake Mungo paleomagnetic excursion (30 ka) was observed at 81.5 mbsf. The upper part of the mass-flow deposit (Unit III) lacks *P. obliquiloculata* and *G. tumida,* but these species and rare *G. menardii* appear in the lower part of Unit III. These planktonic foraminifers and a bathyal (continental slope) assemblage of benthic foraminifers are reworked. Subunit IVA has a warm-water planktonic assemblage, including *G. tumida,* but lacking *G. menardii*. The absence of *P. lacunosa* and *E. huxleyi* constrains the age to 0.26 to 0.46 Ma. Unit IV at Site 933 is thus correlated with Unit V at Site 931 on the basis of seismic-reflection continuity, similar lithology, and biostratigraphy, and is assigned a middle Pleistocene age.

Pore-water data, the abundance of methane, and total organic carbon contents were similar to Sites 930–932. Sulfate is removed by 13 mbsf, but pore-water sulfate is also found in the lower part of the debris flow (Unit III) in concentrations of 1–2 mM. Total nitrogen, which averages 1.0%–1.2% in Unit II, drops to 0.06%–0.08% in the debris flow, with a high carbon:nitrogen atomic ratio. Chlorinity levels in the lower part of Unit III and in Subunit IVA are low (around 550 mM) compared with most of the section (around 560 mM) and are similar to the interglacial interval of Unit I.

In general, physical properties data also show trends similar to those established at Sites 930–932. Unit IV sediment has a higher water content than would be expected under normal consolidation, suggesting that dewatering has been inhibited. A pronounced elliptical reduction in the size of the borehole at 215 mbsf corresponds to an abrupt decrease in wet-bulk density from 2.0 to 1.9 g/cm^3 and corresponding changes in water content and porosity, indicating an overpressured formation. The GHMT log data show quite different total magnetic field character in Subunit IIB compared with Unit IV.

The preliminary data from Site 933 confirm the stratigraphic observations at Site 931, namely that the Bottom Levee Complex on the eastern Amazon Fan is of middle Pleistocene age. The overlying mass-flow deposit contains blocks of continental slope sediment. The levee flank sediment in Subunit IIB has abundant cross-lamination, in contrast to the lack of cross-laminated sand beds in the levee crest sediment of Subunit IVB.

[1]Flood, R.D., Piper, D.J.W., Klaus, A., et al., 1995. *Proc. ODP, Init. Repts.,* 155: College Station, TX (Ocean Drilling Program).

[2]Shipboard Scientific Party is as given in the list of participants in the contents.

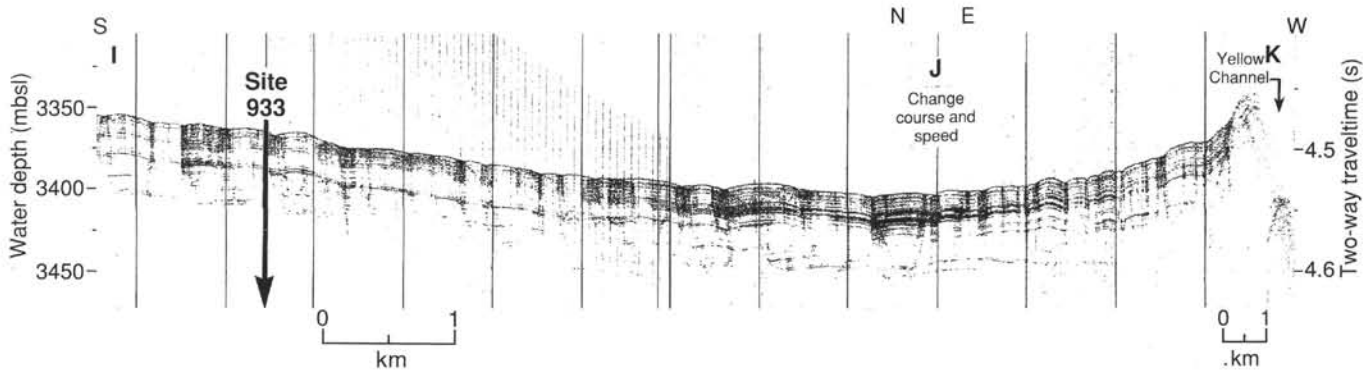

Figure 1. A 3.5-kHz profile through Site 933, showing the relationship of the site to the Yellow Channel. Note that west of point J, the ship accelerated to about twice the speed compared with the section between points I and J. Location is shown in Figure 1 of the "Site 931" chapter, this volume.

SETTING AND OBJECTIVES

Introduction

Site 933 (proposed Site AF-9) was relocated about 3 km south of its originally planned position to sample as complete a hemipelagic sequence as possible on the crest of the levee of the Bottom Levee Complex that was first sampled at Site 931. This relocated site was also intended to provide an opportunity to log the debris-flow interval that was not logged at Site 931 because of hole conditions.

Setting

Site 933 is located on the eastern part of the Amazon Fan, on the eastern (right) flank of the Yellow levee about 4 km from the channel (Fig. 1; see also Fig. 1 of "Site 931" chapter, this volume). The Yellow Channel-levee System is younger than Channel-levee System 5 cored at Site 931 and Channel-levee System 6B cored at Site 932 (Manley and Flood, 1988).

The revised site position was selected from crossing *JOIDES Resolution* pre-site survey seismic-reflection profiles (1943/10 April and 0232/11 April; Fig. 2). Site 933 showed the least erosion of the levee crest sediment of the entire 20-km-long zone of the early Pleistocene levee crest that has been surveyed by the *Ewing* and the *JOIDES Resolution*.

The surficial sediment at the site, interpreted from 3.5-kHz subbottom profiles (Fig. 1), shows a 12-ms-thick (10 m) acoustically stratified sequence that maintains an almost constant thickness toward the Yellow Channel. The underlying 20-ms (18 m) section is more acoustically transparent, but includes a few strong reflections. It thickens toward the Yellow Channel, and, at least in its lower part, exhibits sediment-wave architecture. The seismic-reflection data (Fig. 2) show below this unit a thick interval of levee-crest strata (about 80 ms thick) with increasing numbers of high-amplitude reflections toward the base. These overlie a thick acoustically incoherent unit with hyperbolic diffractions that is seismically correlated with the debris-flow unit at Site 931. The debris flow overlies the crest of the same levee that was sampled at the base of Site 931. Site 933 is located near the levee crest about 1.5 km west of the buried channel axis.

Objectives

The principal objectives of coring at Site 933 were:

1. Stratigraphic sampling of microfossil-rich sediment on top of the Bottom Levee Complex that occurred at about 350–360 mbsf in Hole 931B.
2. Sampling of the debris-flow deposit(s) on top of the middle Pleistocene levee.
3. Further sampling of the Bottom Levee Complex to characterize it mineralogically, paleontologically, and magnetically, at a site where less disturbance might be expected than at Site 933.

A secondary objective was to resample the near-surface hemipelagic sequence above Yellow, previously sampled at Sites 931 and 932.

The principal objectives of logging were to characterize the debris-flow unit (particularly using the FMS), to investigate the magnetic properties of the Bottom Levee Complex (with the GHMT), and to better understand the physical properties of the transition from the middle Pleistocene levee to the overlying debris flow.

OPERATIONS

Transit: Site 932 to Site 933 (AF-9)

The transit from Site 932 to Site 933 covered approximately 14 nmi in just over 1.5 hr. We proceeded directly to the GPS coordinates 05°05.917′N, 46°48.778′W and deployed a retrievable beacon at 1905 hr 12 April. This position was moved from that originally proposed as a result of the seismic-reflection data collected prior to drilling Site 932.

Hole 933A

We assembled a bottom-hole assembly similar to that used at the previous sites (Site 930–932) and ran the bit to the seafloor. The distance from sea level to rig floor, which depends on the ship's draft, was 10.90 m for Hole 933A.

We positioned the bit at 3373.0 mbrf and spudded Hole 933A at 0128 hr 13 April. Core 1H recovered 5.70 m of sediment (Table 1). The mud line was defined to be 3376.8 mbrf. We took Cores 1H through 10H from 0 to 91.2 mbsf (3376.8–3468.0 mbrf) and recovered 100.61 m of sediment (110% recovery). In many of the cores recovered at Site 933, sediment began to extrude from the core liner due to gas expansion once the liner was taken out of the core barrel. Core disturbance was minimized by drilling small holes in nearly all of the core liners to allow gas to escape.

Cores were oriented using the Tensor tool from Core 3H through 10H. ADARA heat-flow measurements were taken at Cores 6H and 9H. The liner of Core 8H was split and it was difficult to pull out of the core barrel. Overpull (when retrieving the core barrel from the sediment) was 20,000 lb at Core 6H (53.2 mbsf) and increased to 50,000 lb at Core 9H. A slim-nosed APC shoe was used on Core 10H

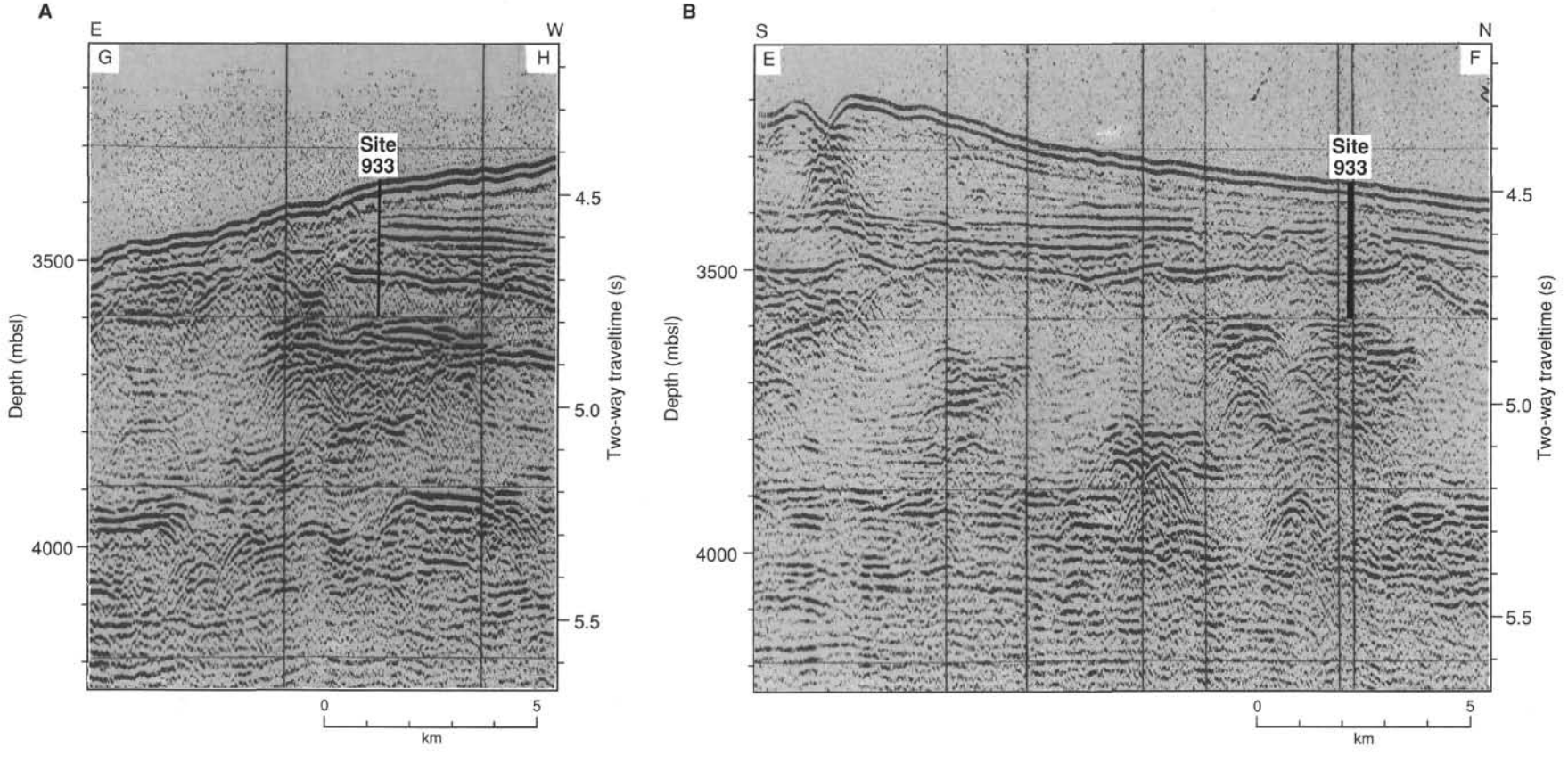

Figure 2. Seismic sections through Site 933. *JOIDES Resolution*, 1900–2010 UTC on 10 April 1994 (**A**) and 0105–0255 UTC on 11 April 1994 (**B**). Location is shown in Figure 1 of the "Site 931" chapter, this volume.

Table 1. Site 933 coring summary.

Core	Date (1994)	Time (UTC)	Depth (mbsf)	Length cored (m)	Length recovered (m)	Recovery (%)
155-933A-						
1H	April 13	0545	0.0–5.7	5.7	5.70	100.0
2H	April 13	0645	5.7–15.2	9.5	10.64	109.8
3H	April 13	0745	15.2–24.7	9.5	10.77	113.3
4H	April 13	0845	24.7–34.2	9.5	10.42	109.7
5H	April 13	0940	34.2–43.7	9.5	10.11	106.4
6H	April 13	1100	43.7–53.2	9.5	10.45	110.0
7H	April 13	1150	53.2–62.7	9.5	10.70	112.6
8H	April 13	1255	62.7–72.2	9.5	10.61	111.7
9H	April 13	1405	72.2–81.7	9.5	11.01	115.9
10H	April 13	1505	81.7–91.2	9.5	9.10	95.8
11X	April 13	1635	91.2–99.8	8.6	6.42	74.6
12X	April 13	1740	99.8–109.4	9.6	4.13	43.0
13X	April 13	1840	109.4–119.0	9.6	1.51	15.7
14X	April 13	2010	119.0–128.7	9.7	4.18	43.1
15X	April 13	2145	128.7–138.3	9.6	6.43	67.0
16X	April 13	2310	138.3–147.9	9.6	3.76	39.1
17X	April 14	0030	147.9–157.6	9.7	3.42	35.2
18X	April 14	0145	157.6–167.2	9.6	3.28	34.1
19X	April 14	0335	167.2–176.9	9.7	2.59	26.7
20X	April 14	0455	176.9–186.5	9.6	8.19	85.3
21X	April 14	0620	186.5–196.2	9.7	6.65	68.5
22X	April 14	0730	196.2–205.8	9.6	6.82	71.0
23X	April 14	0845	205.8–215.5	9.7	2.60	26.8
24X	April 14	1015	215.5–225.2	9.7	5.68	58.5
25X	April 14	1150	225.2–234.8	9.6	1.81	18.8
26X	April 14	1320	234.8–244.5	9.7	5.29	54.5
27X	April 14	1440	244.5–254.2	9.7	5.22	53.8
Coring totals				254.2	177.8	69.90

Note: An expanded version of this coring summary table that includes lengths and depths of sections, location of whole-round samples, and comments on sampling disturbance is included on the CD-ROM in the back pocket of this volume.

to determine if this would reduce the overpull; however, it was not reduced, and there was no change in recovery. The core barrel only partially completed its stroke during Core 10H. During retrieval of Core 10H (at about 1051 hr 13 April), the beacon self-released and ceased working. We deployed a backup beacon at 1055 hr 13 April.

XCB Cores 11X through 27X were taken from 91.2 to 254.2 mbsf (3468.0–3631.0 mbrf), coring 163.0 m and recovering 78.62 m (48.2% recovery). Drilling on the last core, Core 27X, appeared faster than on previous cores. The combined APC/XCB recovery at Site 933 was 69.9%. Hole angle, measured by the Tensor tool, was 2.8° at 24.7 mbsf, 3.0° at 53.2 mbsf, 3.2° at 72.2 mbsf, and 3.4° at 91.2 mbsf.

In preparation for logging, we pulled the drill pipe to 68.0 mbsf (3444.8 mbrf) and then moved back to the bottom of the hole. Only about 1 m of sediment had filled the bottom of the hole. We pumped the go-devil (to open the lockable float valve [LFV]), and the pipe was pulled to 86.6 mbsf (3463.4 mbrf). We then arranged the drill pipe to make it possible to pick up the drill pipe an additional 30 m to log the upper part of the hole. The Quad-combo, FMS, and GHMT logs were run (see "Downhole Logging" section, this chapter). The GHMT tool activated (closed) the LFV as it exited the drill pipe. The LFV had to be pumped open to allow the tool to reenter the pipe after logging. We pulled the bit above the seafloor at 0753 hr 15 April, and it cleared the rig floor at 1315 hr 15 April. We then recovered the beacon.

LITHOSTRATIGRAPHY

Introduction

Hole 933A recovered sediment from a maximum depth of 249.72 mbsf with virtually complete recovery from the seafloor to 97.62 mbsf, but with markedly less recovery farther downhole (Fig. 3). Expansion of methane gas during core recovery commonly affected the sediment by disrupting the primary sedimentary structures in many silt and sand beds and by producing void spaces within many of the core sections (see "Lithostratigraphy" section in the "Explanatory Notes" chapter, this volume).

Description of Lithostratigraphic Units

Unit I

Interval: 155-933A-1H-1, 0–52 cm
Age: Holocene
Depth: 0.00–0.52 mbsf

Unit I consists of a yellowish brown (5Y 5/4) nannofossil-foraminifer clay from 0.00 to 0.48 mbsf overlying a dark yellowish brown (10YR 3/4) diagenetic crust that marks the base of Unit I at this site. This diagenetic, iron-rich crust has been recovered at most other sites during Leg 155 at similar depths (see Fig. 6 of "Lithostratigraphy" section, "Site 930" chapter, this volume). Similar iron-rich crusts were previously analyzed and correlated throughout the Amazon Fan and adjacent Guiana Basin (e.g., Damuth, 1977; see "Introduction" chapter, this volume). The calcareous clay above the crust commonly shows extensive burrow mottling and has a carbonate content of 33% near the base of Unit I at 0.40 mbsf (see "Organic Geochemistry" section, this chapter).

Unit II

Interval: 155-933A-1H-1, 52 cm, through -11X-CC, 22 cm
Age: Holocene to late Pleistocene
Depth: 0.52–97.62 mbsf

Unit II consists predominantly of terrigenous dark olive gray (5Y 3/2) to very dark gray (5Y 3/1) silty clay. Laminae and thin beds of silt and very fine sand are common below about 18 mbsf within this unit (Figs. 3 and 4). The carbonate content of Unit II is slightly higher than 10% immediately below the base of Unit I (Sample 933A-1H-1, 79–80 cm) but is generally less than 3% downhole. Distinct color banding, mottles (on a centimeter scale), and blebs (soft micronodules approximately 1-mm scale) are common throughout much of Unit II. The bands and irregular mottles are generally black (N 2/0 where color boundaries are sharp, but 5Y 2.5/1 where less distinct in both contrast and boundaries; Fig. 5). These black stains are caused by diagenetic hydrotroilite, which imparts an ephemeral black color (N 2/0) to the sediment (see "Introduction" chapter, this volume). In general, darker banding and mottles do not appear to be associated with particular detrital grain sizes, although in some cases very thin silt laminae (less than 1 mm thick) are heavily stained (see thin laminae at 7, 20, and 87 cm in the whole-core photograph that includes Section 933A-2H-6 in the "Cores" section, following the site chapters of this volume). Unit II is subdivided into subunits based on the frequency of occurrence of common silt laminae, thin silt beds, and sandy silt or silty sand beds (Figs. 3 and 4).

Subunit IIA

Subunit IIA extends from the base of Unit I to a depth of 14.37 mbsf (155-933A-2H-6, 117 cm). This subunit consists of a dark gray (5Y 4/1) clay with distinct black (N 2/0) mottles (Fig. 5) that subtly changes downhole to dark olive gray (5Y 3/2) silty clay with mottles and black color banding by 6.25 mbsf (Section 155-933A-2H-1B, 26 cm; Fig. 4). [Note: There are two parts of Section 1 of Core 933A-2H; Section 1A is 29 cm long; Section 1B is 142 cm long.] The carbonate content of this subunit ranges from 0.3% to 10.6% (average is 4.9% for five samples) without any apparent systematic variation with depth.

Subunit IIB

Subunit IIB extends from 14.37 to 97.62 mbsf (155-933A-11X-CC, 22 cm) and is characterized by very dark gray (5Y 3/1) silty clay with numerous silt laminae and beds of silt and sand (Figs. 6 and 7).

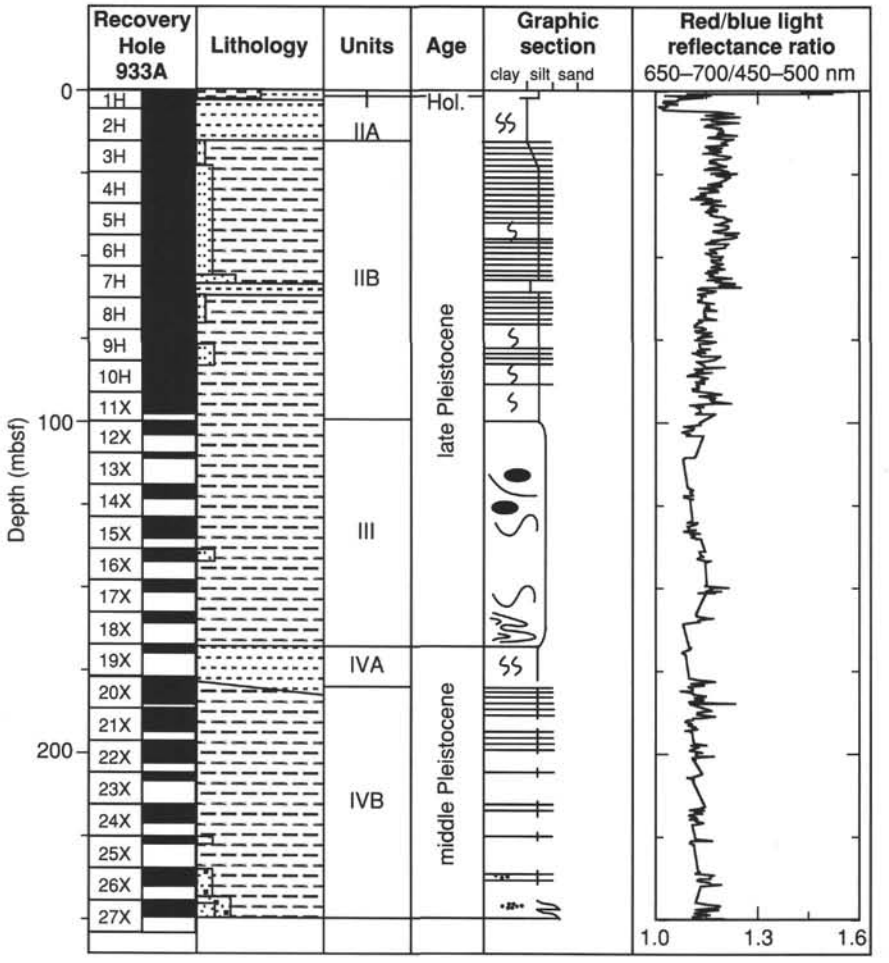

Figure 3. Composite stratigraphic section for Site 933 showing core recovery, a simplified summary of lithology, depths of unit boundaries, age, a graphic section with generalized grain-size and bedding characteristics, and downhole variations in light-reflectance values. The lithologic symbols are explained in Figure 1 of the "Explanatory Notes" chapter, this volume.

The silt, silty sand, and fine sand beds are typically interlaminated with mud, most commonly in their upper part. Parallel lamination was observed in most beds as well as in many of the thicker laminae (>5 mm). Cross-lamination is much less common and characterizes 20% or less of the beds. Sand and silt beds compose as much as 30% of some cored intervals (e.g., Section 933A-6H-3). Estimates of cumulative thickness of the coarse layers are difficult because of the disruption of these beds by gas expansion.

In the middle of Subunit IIB, just above 60 mbsf, a 0.65-m-thick zone of discontinuous color banding and streaks of very dark gray (5Y 3/2) silty clay with black (N 2/0) clay overlies a 3.89-m-thick bed (interval 933A-7H-5, 140 cm, through -8H, 44 cm) of massive black clay that contains fragments of plant material and shells (Fig. 8). The base of this massive clay bed is a distinct, angular contact; both a silt laminae and a silt bed that are less than 0.24 cm below the base of the massive clay have been vertically offset several centimeters (Fig. 9). This massive clay bed is interpreted as the deposit of a muddy debris flow that has sheared and deformed the underlying layers.

The occurrence of sand and silt layers in Subunit IIB is not uniform downhole, indicating several cycles of deposition (Fig. 4). Relatively few silt or sand beds (or laminae) occur between 40.20 and 44.26 mbsf, between 68.28 and 71.30 mbsf, between 83.26 and 87.35, and from 89.00 to the bottom of Subunit IIB (intervals 933A-5H-5, 0 cm, through -6H-2, 26 cm; 933A-8H-5, 73 cm, through -7, 75 cm; 933A-10H-2, 6 cm, through -5, 96 cm; and 933A-10H-6, 111 cm, through -11X-CC, 22 cm). These 3- to 8-m-thick intervals exhibit a general hemipelagic character, with few coarse laminae and interbeds. The relative paucity of coarse components in these intervals compared to the rest of this subunit indicates lateral shifts in the loci of coarse-sediment deposition and/or a lack of turbidity currents during these time intervals.

Unit III

Interval: 155-933A-12X-1, 0 cm, through -19X-1, 11 cm (upper contact not recovered)
Age: late Pleistocene
Depth: 97.62–167.31 mbsf

Unit III is 70 m thick, but recovery is relatively incomplete compared to the other units at Site 933 (Fig. 3). The top of this unit was not recovered, but must occur within the 2-m gap between Cores 933A-11X and -12X. The upper 12 m of Unit III (Sections 933A-12X-1 through -13X-1) is a very dark gray (5Y 3/1) massive silty clay with mud clasts. This unit is more silt-rich than Unit II. Unit III below this massive silty clay shows internal deformation in many of the core sections. Core 933A-14X consists of a very dark gray (5Y 3/1) very silty clay with some evidence for internal deformation in the form of a striped "wood-grain" or variegated structure, which also is present in interval 933A-17X-1, 78 cm, through -CC, 19 cm. Clearer examples of internal deformation that are less likely to be the result of drilling disturbance are found from 129.00 to 134.62 mbsf (interval 933A-15X-1, 30 cm, through -4, 142 cm) and from 158.20 to 160.14 mbsf (interval 933A-18X-1, 60 cm, through -2, 104 cm; Figs. 10 and 11). FMS images (back-pocket CD-ROM) confirm that Unit III deposits are variably tilted and folded in the subsurface.

Unit III is interpreted as a thick debris-flow deposit, with large, deformed mud clasts in a mud matrix forming much of the lower 50 m of the deposit.

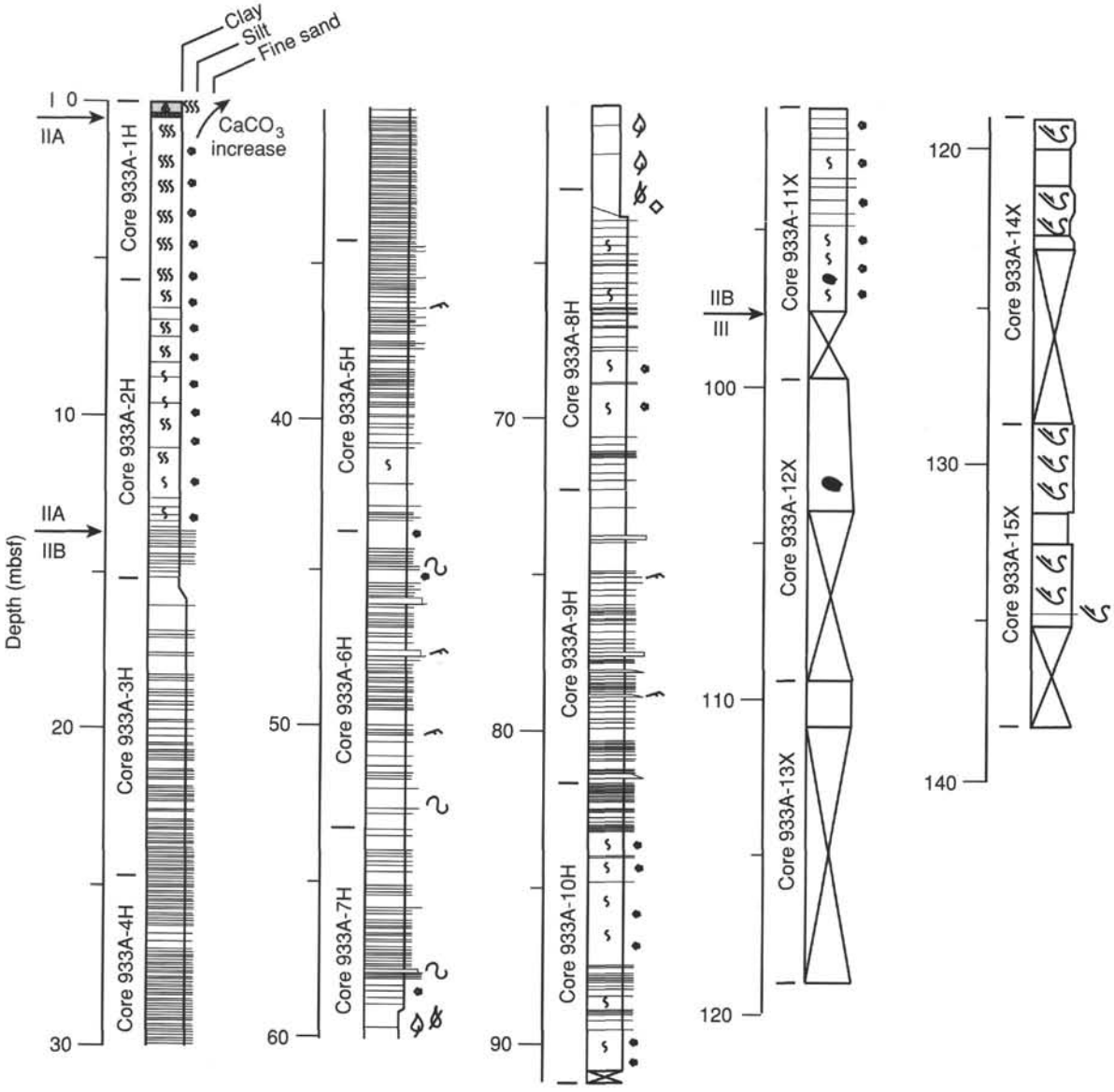

Figure 4. Graphic sedimentological columns for Site 933 showing grain-size variations (width of columns), bed thickness, and sedimentary structures; symbols and preparation of these columns are explained in the "Lithostratigraphy" section of the "Explanatory Notes" chapter, this volume. Arrows indicate the positions of unit and subunit boundaries. The upper part of the column is shown in strike section of the foldout (back pocket, this volume) for comparison of levee sequences on the middle and upper fan.

Unit IV

Interval: 155-933A-19X-1, 11 cm, through -27X-CC, 8 cm
Age: middle Pleistocene
Depth: 167.31–249.72 mbsf

Unit IV consists of very dark gray (5Y 3/1) mottled clay and silty clay with silt laminae and beds of silt and fine sand (Figs. 3 and 4). The boundary with Unit III is at or above an angular, distinct surface (Section 933A-19X-1 at 11 cm), but drilling deformation of the sediment above and below this interval indicates that the boundary could occur in the 2-m gap between the bottom of Core 933A-18X and the top of Core 933A-19X. Unit IV can be divided into two subunits based on the relative abundance of silt and sand.

Subunit IVA

This subunit consists of very dark gray (5Y 3/1) silty clay that is moderately bioturbated, mottled, and has small millimeter-scale blebs (?soft micronodules and/or coloration) of hydrotroilite (Fig. 5B). The sediment is uniform in character downhole to the contact with Subunit IVB at 179.03 mbsf (155-933A-20X-2, 63 cm).

Subunit IVB

Subunit IVB extends from a 0.15-m-thick, massive sand bed at 179.03 mbsf (interval 155-933A-20X-2, 63–78 cm) to the bottom of the hole and consists of very dark gray (5Y 3/1) silty clay with numerous silt laminae and fine sand beds. Core recovery was relatively good in the upper part of Subunit IVB from the top sand bed to 203.02 mbsf (base of Core 933A-22X-CC, 23 cm; Fig. 3). In this interval, about 90% of the coarser layers are fine sand and silt laminae, with the thicker laminae (>5 mm) commonly containing mud interlaminations. The rest of the coarse fraction generally comprises sand and silt beds with massive or parallel laminated structure. No cross-lamination was observed.

The core recovery in the lower part of Subunit IVB was poorer, and most sections show drilling disturbance that disrupts most sand

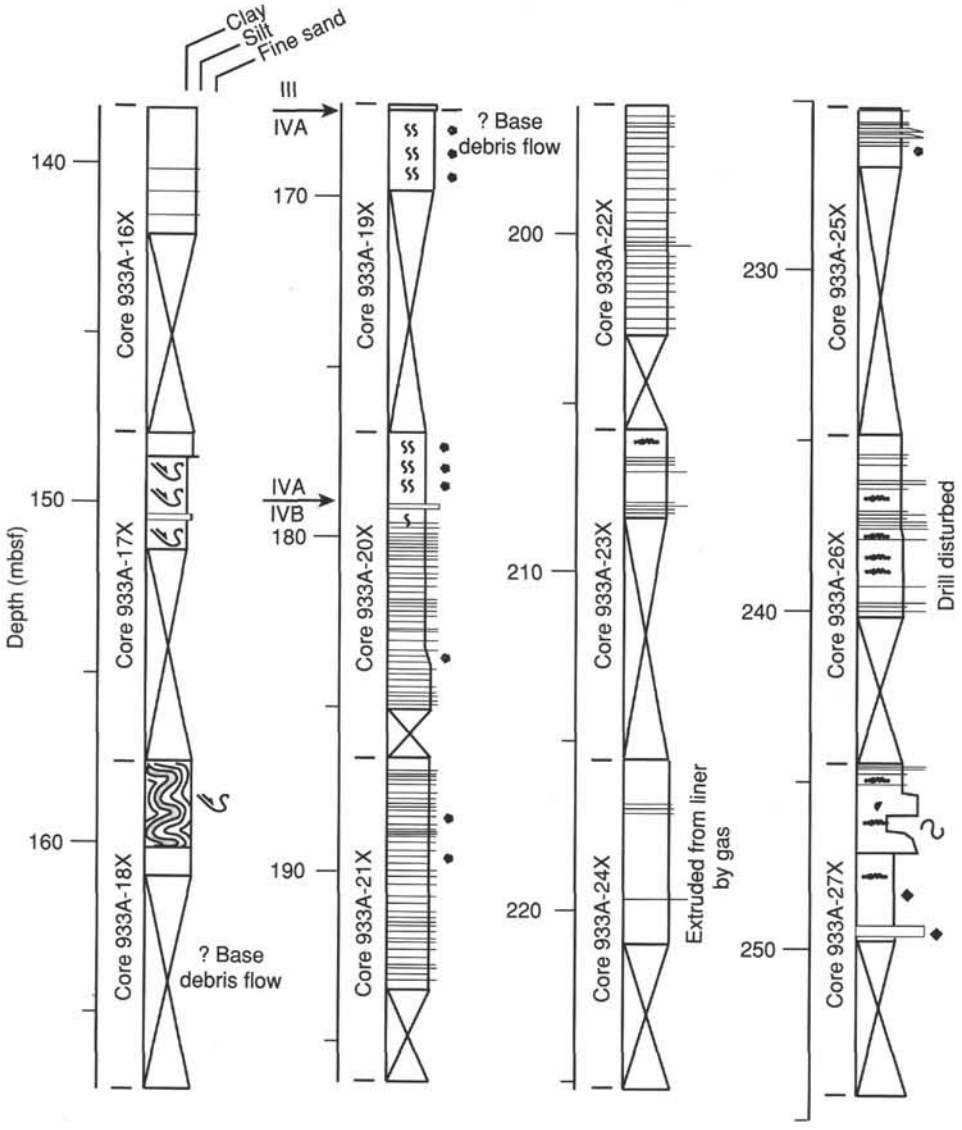

Figure 4 (continued).

and silt layers. Silt laminae are relatively rare; silt commonly occurs as streaks and blebs in silty clay. The coexistence of recognizable (i.e., relatively intact) sand beds and intervals with silty clay that is mixed with a high proportion of sand lenses and blebs suggests that there is more sand below 206.63 mbsf (Section 933A-23X-2 at 14 cm). This observation is consistent with the poor core recovery for this part of the subunit.

Mineralogy

Smear-slide Synthesis

Silty clay, the dominant lithology at this site, contains 20%–50% silt consisting of about 50%–60% quartz, 10%–20% feldspars, 5%–10% micas, and 5%–15% accessory minerals, mainly hornblende and pyroxene. Except for nannofossils and foraminifers in Unit I, biogenic particles are rare. Organic (plant) detritus is commonly present. Authigenic minerals include black hydrotroilite and rare blue-green vivianite. Most quartz grains (about 90%), feldspars, and ferromagnesian minerals are fresh and angular to subangular. The remainder of the quartz grains, as well as rare zircon and monazite grains, are subrounded. The subrounded quartz grains have a surface coating of iron-oxide. The two differently rounded quartz populations suggest at least two different provenance areas.

XRD Data

Bulk XRD analysis was performed on a sample of the dominant silty clay from most cores recovered in Hole 933A (Table 2). The common minerals throughout the cored succession, based on the relative intensities of their primary peaks (normalized to quartz intensity), are quartz, plagioclase, augite, and the clay minerals smectite, illite (+ mica), and kaolinite. Several samples contain K-feldspar and a few contain amphibole, apparently hornblende. Calcite was not identified. The clay mineral with the highest relative peak intensity is illite (+ mica). All clays decrease in relative abundance from Core 933A-1H through -11X (Fig. 12) and, farther downhole, increase from Core 933A-15X through -20X. These variations are most apparent in the illite (+ mica) intensities. The part of the succession with low relative abundances of clay minerals (Cores 933A-12X through -18X) corresponds to the Unit III debris flow.

Spectrophotometry

The light-reflectance data illustrate several lithologic distinctions at Site 933 (Fig. 3). The ratio of the red/blue wavelength bands records changes in the lithology presumably resulting from variations in the relative abundance of reduced and oxidized phases of iron.

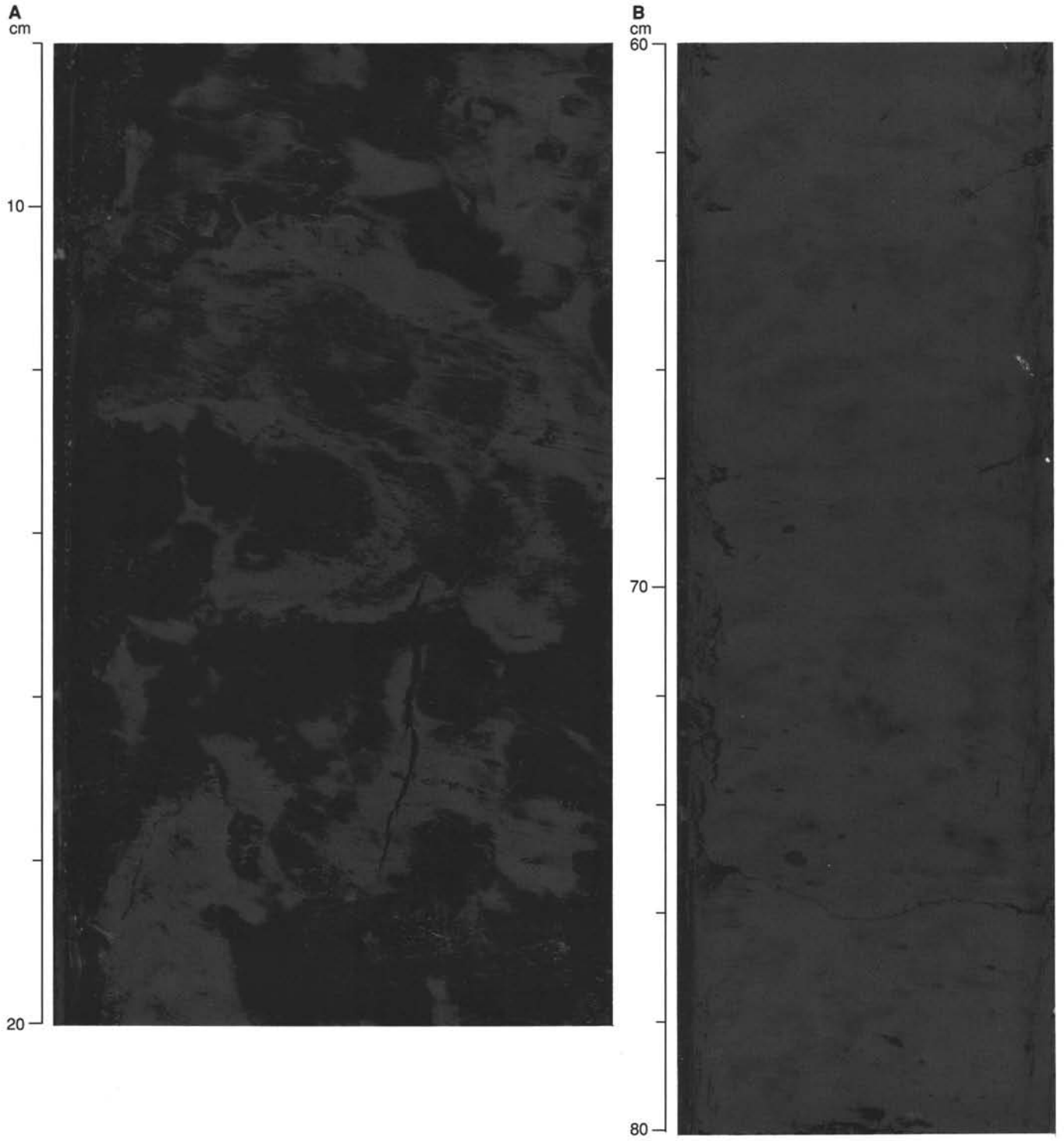

Figure 5. **A.** Example of sediment mottling marked by hydrotroilite (from lithologic Subunit IIA) showing very irregular, distinct boundaries with strong contrast between the black mottles (N 2/0) with the dark gray (5Y 4/1) background color (interval 933A-1H-4, 8–20 cm). **B.** Faintly mottled sediment from Subunit IIB showing less contrast between the black (5Y 2.5/1) mottles and the dark olive gray (5Y 3/1) silty clay background (interval 933A-10H-5, 60–80 cm).

Highest reflectance values in the red spectrum (650–700 nm) correlate with the brown calcareous clay of Unit I, whereas the lowest red/blue ratio occurs just below Unit I and corresponds to the dark gray clay with distinct black mottles (stained with hydrotroilite) in the upper part of Subunit IIA (Section 933A-2H-1A, 0 cm). The marked downhole increase in the red/blue ratio at about 6 mbsf appears to correspond to the first occurrence of black color banding (6.25 mbsf; Section 933A-2H-1B at 26 cm). It is difficult to assess whether this increase in long wavelength reflectance is primarily a result of high iron oxyhydroxide content in Subunit IIA below 6 mbsf or results from rapid oxidation of iron monosulfides shortly after the core was split. All of Unit II below 6 mbsf is characterized by this slightly en-

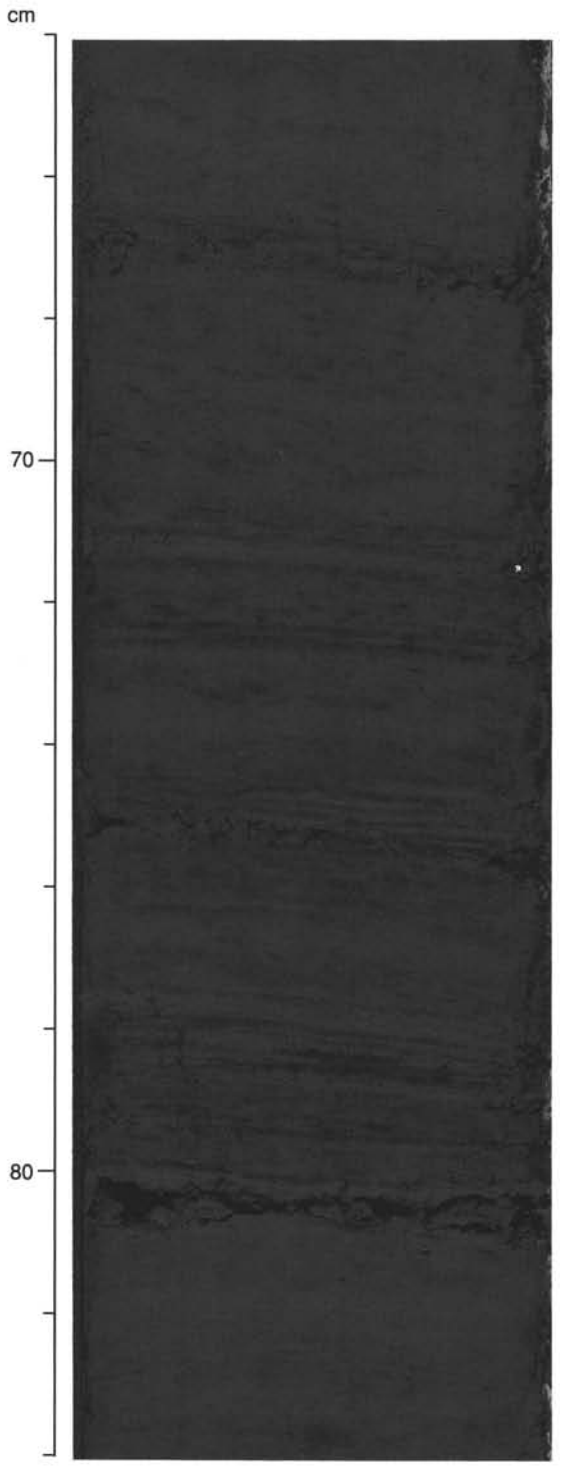

Figure 6. Silt and silty clay interlaminations in color-banded to mottled silty clay from Subunit IIB (interval 933A-5H-1, 64–84 cm).

hanced long wavelength reflectance (Fig. 3). The red spectrum reflectance decreases at 98 mbsf, marking the lithologic boundary between Unit II and Unit III. Thus, reflectance of the red spectrum tends to increase with higher proportions of silt and sand laminae or beds within the silty clay units. There were no significant changes in the red/blue ratio below 100 mbsf that marked lithologic boundaries. The light reflectance values for Unit IVB are generally in the same range as recorded for the lower part of Unit IIB.

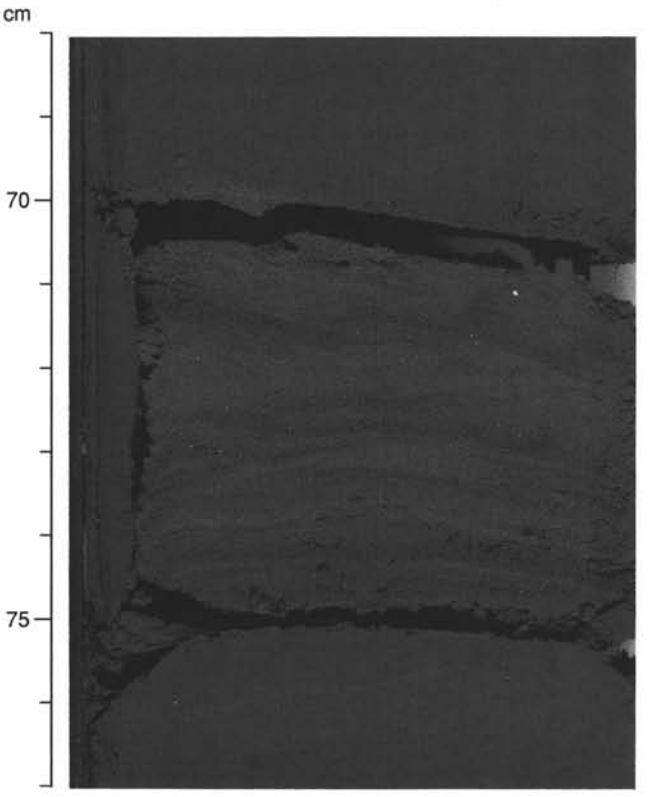

Figure 7. Silt bed displaying parallel and cross-lamination (Bouma T_{b-d} interval) in very dark gray (5Y 3/1) silty clay of Subunit IIB (interval 933A-6H-5, 68–77 cm).

Discussion

Units II and IV are generally of similar lithology, with their upper subunits lacking coarse-grained beds and their lower subunits characterized by common silt laminae, silt beds, and laminae and beds of very fine to fine sand. Both units are apparently turbidite sequences overlain by hemipelagic intervals, although no equivalent of Unit I (calcareous clay) was observed between Units III and IVA. Several features distinguish the turbidite Subunits IIB and IVB. Sand beds in Subunit IIB commonly exhibit cross-lamination. In the interval with the most sand and silt beds (Cores 933A-4H through -7H), approximately 20% (23 of 102 beds counted) of the silt and sand beds are cross-laminated. In Unit IVB through the interval where there was relatively good recovery of fine sand and silt layers (Cores 933A-20X through -23X), no cross-lamination was observed (0 of 100 beds counted). Recovery was poor in the lower part of Subunit IVB, but it appears that there is a higher proportion of sand beds and laminae relative to silt beds and laminae than in the upper part of this unit (Fig. 4). In general, Subunit IVB exhibits a fining- and thinning-upward sequence of turbidite deposits. Subunit IIB, in contrast, shows multiple cycles in the deposition of the sand and silt intervals (Figs. 3 and 4).

BIOSTRATIGRAPHY

Calcareous Nannofossils

Calcareous nannofossils recovered at Site 933 represent a stratigraphic interval from Holocene (CN15b) through the Pleistocene nannofossil Zone CN14b (Table 3). Nannofossils are abundant and well preserved in the pelagic highstand deposits of Holocene-age Unit I (0–0.52 mbsf). A highly diversified and well-preserved *Emil-*

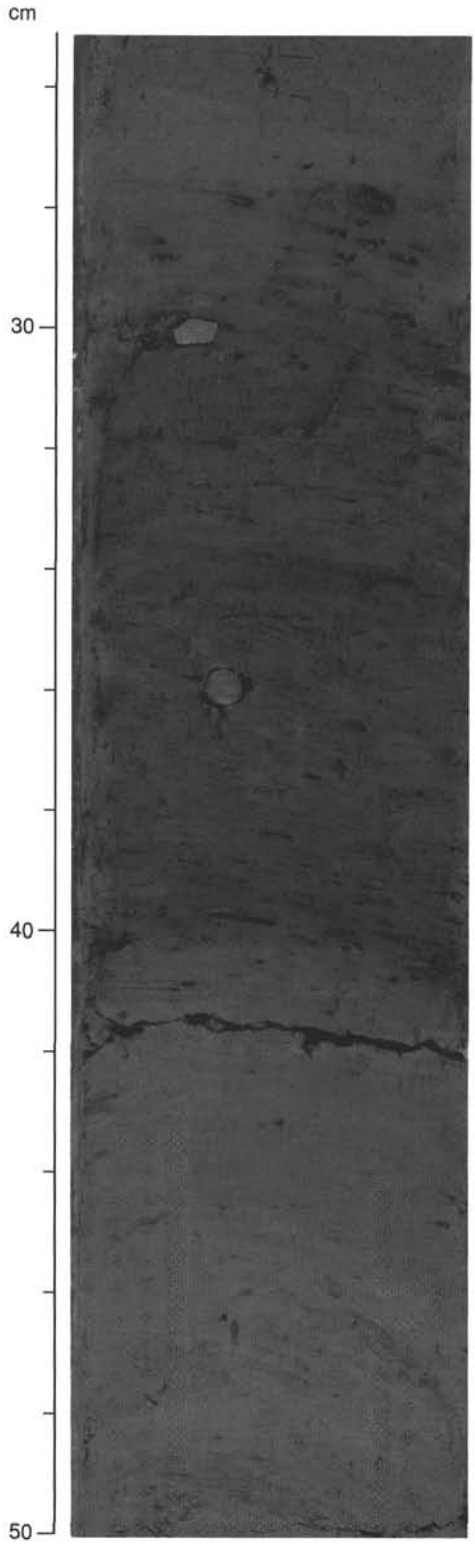

Figure 8. Angular contact (sloping to the right from 43 to 47 cm) between massive black (N 2/0) clay containing a shell fragment and rounded pebble, and dark olive gray (5Y 3/2) silty clay in Subunit IIB. The silt bed below the contact (at 47 cm) has been faulted (interval 155-933A-8H-2, 25–50 cm).

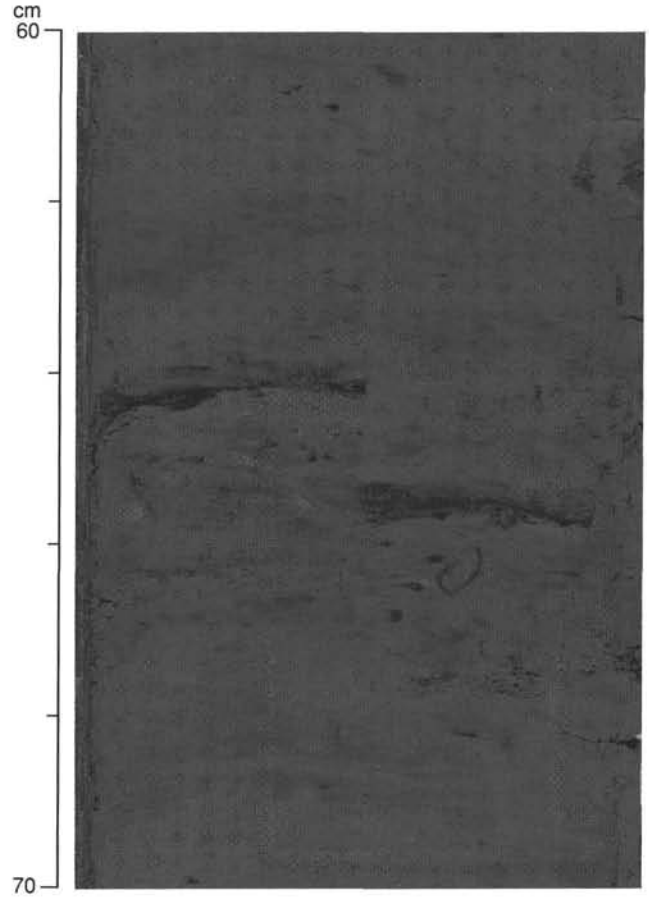

Figure 9. Minor fault offsetting silt laminae in the silty clay of Subunit IIB (interval 155-933A-8H-2, 60–70 cm).

iania huxleyi acme assemblage (Zone CN15b) occurs in the mud line sample. The pre-Holocene sequence of Unit II from 5.7 to 97.6 mbsf (Samples 933A-1H-CC, 23–24 cm, through -11X-CC, 21–22 cm) is a levee flank deposit consisting of clay with silt and silty sand beds. Nannofossils are poorly preserved when found. Nannofossils are also rare within the debris-flow unit, Unit III from 104 to 167 mbsf (Samples 933A-12X-CC, 20–21 cm, through -19X-1, 4 cm), but reappear in high abundance and fairly good preservation in the thin pelagic clay of Subunit IVA from 167.3 to 169.5 mbsf (Samples 933A-19X-1, 13 cm, through -19X-CC, 21–22 cm). This assemblage is dominated by species of the genus *Gephyrocapsa,* which have an average size of 4 to 5.5 µm. Because the stratigraphically important species *P. lacunosa* and *E. huxleyi* were not found, this unit is within nannofossil Zone CN14b (0.26–0.46 Ma). The *Gephyrocapsa* assemblage disappears from the sedimentary record between 169 and 185 mbsf (Samples 933A-19X-CC, 21–22 cm, and 933A-20X-CC, 185 cm). In the underlying Subunit IVB, calcareous nannofossils are rare and poorly preserved within the silty clay beds with numerous silt and sand laminae. Within Unit IVB, there are intervals of high carbonate content (e.g., Sample 933A-23X-2, 113 cm). These intervals consist of a matrix of carbonate particles (95%) containing a few poorly preserved nannofossils.

Planktonic Foraminifers

High abundances and a diverse assemblage of planktonic foraminifers characterize the Holocene in Unit I, whereas low abundances (<1%) and a lack of diversity are characteristic of the late

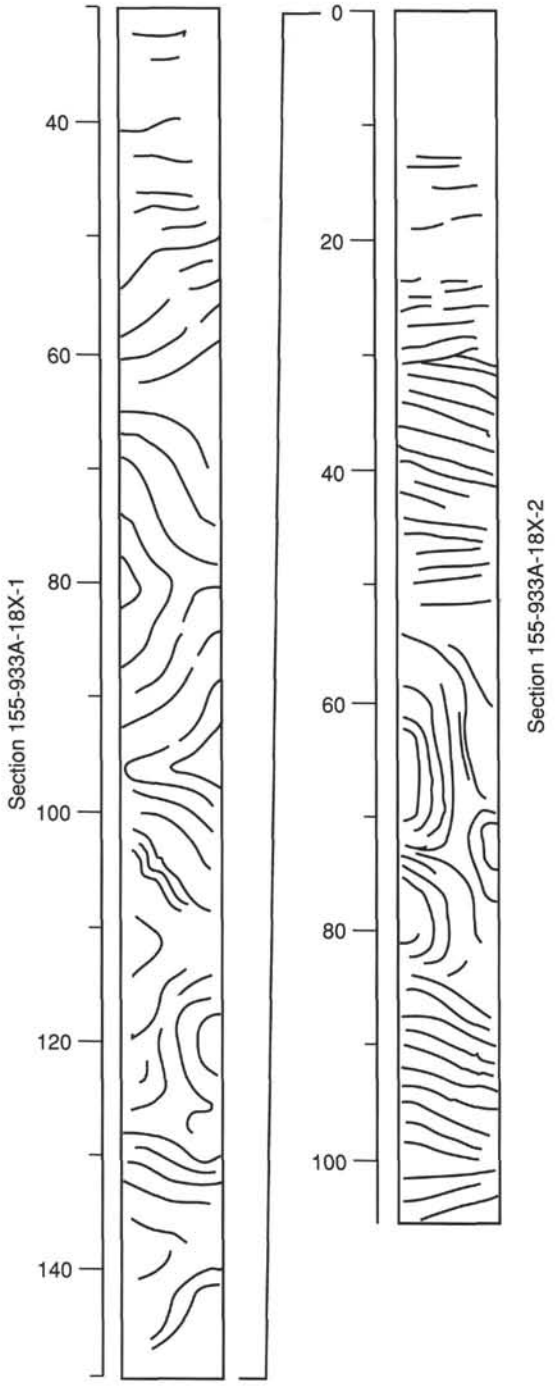

Figure 10. Line drawing of deformation observed in Unit III (interval 155-933A-18X-1, 30 cm, through -2, 104 cm).

Pleistocene sections below Unit I (Table 4). The boundary between Ericson Zones Z and Y (disappearance of *G. menardii* and *G. tumida*) based on core-catcher samples is between 6 and 16 mbsf (Samples 933A-1H-CC, 14–23 cm, and 933A-2H-CC, 32–41 cm; Fig. 13). However, given a possible downhole contamination of the core-catcher samples, this boundary is likely to be near the base of Unit I. Foraminifers are rare or absent from 73 to 90 mbsf (Samples 933A-8H-CC, 27–36 cm, through 933A-10H-CC, 39–48 cm). As Ericson zones are iteratively based on successive abundance shifts, detailed

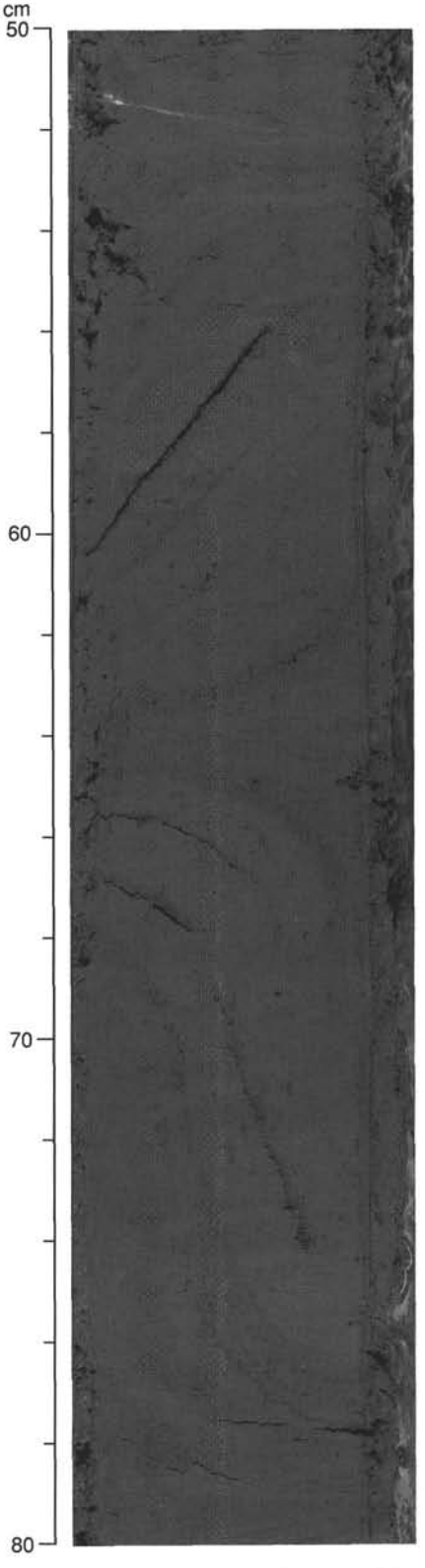

Figure 11. Contorted beds in silty clay of Unit III (interval 155-933A-18X-1, 50–80 cm).

Table 2. Relative peak intensities of the main minerals from representative samples for most cores recovered at Site 933.

Core, section, interval (cm)	Relative intensity of primary peaks								
	Smectite	Mica + Illite	Kaolinite	Quartz	Plagioclase	K-feldspar	Augite	Hornblende	Calcite
155-933A-									
1H-2, 50–51	13.5	32.4	14.4	100.0	9.8	*	4.6	*	*
2H-5, 30–31	12.1	25.6	17.1	100.0	17.4	9.2	3.6	*	*
4H-4, 50–51	12.2	26.0	14.7	100.0	8.2	5.0	2.7	*	*
5H-4, 52–53	13.7	26.5	15.7	100.0	11.6	6.5	3.5	*	*
6H-6, 69–70	16.1	24.8	11.8	100.0	10.2	5.2	3.6	*	*
7H-4, 49–50	16.6	29.8	15.8	100.0	9.2	8.4	3.8	*	*
8H-4, 51–52	13.8	27.3	14.0	100.0	9.0	5.4	4.1	*	*
9H-4, 47–48	14.5	20.7	11.7	100.0	9.3	10.1	3.5	*	*
10H-4, 54–55	13.2	26.1	17.2	100.0	10.3	4.8	2.5	2.5	*
11X-4, 40–41	7.9	15.8	8.4	100.0	7.8	*	2.4	*	*
12X-CC, 2–3	12.5	19.9	13.1	100.0	19.9	5.0	2.3	*	*
15X-4, 49–50	9.9	14.1	9.6	100.0	11.6	*	2.4	*	*
16X-3, 12–13	8.4	18.0	8.1	100.0	7.4	*	1.9	*	*
17X-2, 63–64	11.5	18.7	10.6	100.0	8.3	3.7	2.0	*	*
18X-2, 50–51	13.2	25.7	14.8	100.0	14.2	4.5	2.0	*	*
20X-4, 73–74	13.0	26.8	19.4	100.0	10.4	*	3.0	1.3	*
21X-4, 50–51	15.6	28.0	16.6	100.0	11.4	4.7	2.4	*	*
22X-3, 54–55	14.2	23.3	16.2	100.0	8.9	*	3.2	*	*
23X-2, 55–56	10.7	20.2	13.7	100.0	10.7	4.8	2.4	*	*
24X-3, 26–27	15.4	26.5	11.2	100.0	12.9	*	3.5	*	*
25X-1, 40–41	14.4	22.9	14.9	100.0	10.5	4.9	2.9	*	*
26X-2, 26–27	10.1	29.0	14.4	100.0	10.1	4.6	1.8	*	*
27X-1, 66–67	7.7	16.9	12.0	100.0	9.8	6.2	1.5	3.2	*

Notes: See "Lithostratigraphy" section in "Explanatory Notes" chapter, this volume, for XRD methods. * denotes non-detection.

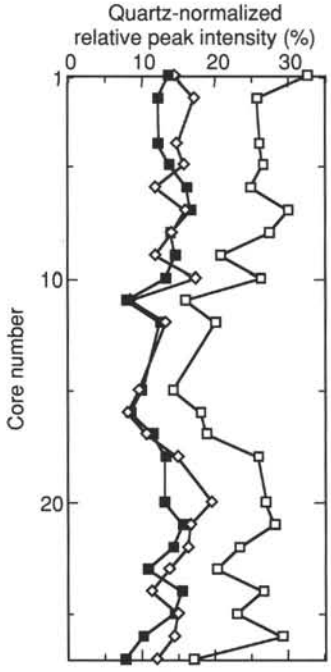

Figure 12. Relative abundances of clay minerals based on XRD analysis for representative samples from cores from Hole 933A. Closed squares = smectite; open squares = illite (+ mica); open diamonds = kaolinite.

interpretation of the sediment age below 73 mbsf is difficult in and below this foraminifer-barren zone. Cores 933A-12X through -19X in Unit III (99.8 to 167.3 mbsf) have been identified as a debris-flow deposit. The occurrences of *G. truncatulinoides* and left-coiling *G. tumida* planktonic foraminifer assemblage within this interval suggest this unit is of Pleistocene age. In Subunit IVA, 167–179 mbsf, the presence of *G. calida calida* (Samples 933A-19X-1, 11–13 cm; -19X-1, 57–63; -19X-2, 133–137 cm) is indicative of a middle to late Pleistocene age. The presence of relatively common *G. ruber* (pink) indicates an age younger than 0.46 Ma. The presence of *G. tumida flexuosa* further constrains the age to an interglacial between 0.1 and 0.46 Ma (isotopic Stages 5 to 11). Subunit IVB, 179–249.7 mbsf, contains *G. tumida,* suggesting interglacial conditions, but contains no age diagnostic taxa.

Benthic Foraminifers

Two types of benthic foraminifers were found sporadically in Hole 933A (Table 4). The first is an upper- to mid-bathyal group composed of *Bulimina marginata, Bolivina striatula,* and *Quinqueloculina sp.* The second is a deep-water, low-oxygen abyssal group composed of *Uvigerina* spp. and *Pyrgo* spp. In the first 25 mbsf, deep-water benthic foraminifers such as *Uvigerina* spp. were found, suggesting low oxygen conditions and in-situ deposition.

Upper- to mid-bathyal water benthic foraminifers were found in abundance from 97 mbsf to 167 mbsf, which corresponds to the debris-flow Unit III. This suggests that these bathyal benthic foraminifers had been transported to the deeper water at Hole 933A. Benthic foraminifers were absent in other sections of Hole 933A.

Siliceous Microfossils

Site 933 is barren of diatoms, except for the mud-line sample in Unit I where solution resistant species of marine pelagic diatoms are present. This assemblage includes warm-water species such as *Coscinodiscus africanus, A. curvatulus,* and *C. eccentricus.* Pre-Holocene diatoms of either marine or freshwater origin were not observed at Site 933. This is most likely due to the combined effects of dilution by the high sedimentation rates and dissolution. Siliceous sponge spicules are the only biogenic silica present in the pre-Holocene sections of Site 933 (Table 4). Radiolarians are present only as fragments in the mud-line samples of Hole 933A.

Palynology

Four samples were examined from Hole 933A. In general, low abundance and moderate preservation are characteristic of these samples. The assemblages observed tend to be dominated by spores and are not diagnostic of specific terrestrial environments. Wood particles have been observed in all sample slides in varying abundance. Dinoflagellates are not present in the samples examined.

Table 3. Calcareous nannofossil and siliceous microfossil abundance data for Hole 933A.

Core, section, interval (cm)	Top interval (mbsf)	Bottom interval (mbsf)	Calcareous nannofossils			Diatoms		Sponge spicules	Radiolarians	Ericson Zone (inferred from foraminifers)	Age (inferred from foraminifers)
			Abundance	Preservation	Zone	Marine	Fresh water				
155-933A-											
1H-1H-MI	0.00		a	g	CN15b	f	r	f	r	Z	Holocene
1H-CC, 23–24	5.69	5.70	f	m		b	b	f	b	Y	late Pleist.?
2H-CC, 41–42	16.12	16.13	vr	—		b	b	b	b	Y	late Pleist.
3H-CC, 50–51	25.96	25.97	vr	—		b	b	b	b	Y	late Pleist.
4H-CC, 54–55	35.11	35.12	tr	—		b	b	b	b	Y	late Pleist.
5H-CC, 57–58	44.30	44.31	tr			b	b	b	b	Y	late Pleist.
6H-CC, 25–26	54.14	54.15	b	—		b	b	b	b	Y	late Pleist.
7H-CC, 31–32	63.89	63.90	vr	—		b	b	f	b	Y	late Pleist.
8H-CC, 36–37	73.30	73.31	b	—		b	b	b	b	—	?
9H-CC, 83–84	83.20	83.21	b	—		b	b	b	b	—	?
10H-CC, 48–49	90.79	90.80	b	—		b	b	b	b	—	?
11X-CC, 21–22	97.61	97.62	b	—		b	b	b	b	Y	late Pleist.
12X-CC, 20–21	103.92	103.93	vr	—		b	b	r	b	RW	late Pleist.
13X-CC, 11–12	110.90	110.91	vr	—		b	b	f	vr	RW	late Pleist.
14X-CC, 21–22	123.17	123.18	r	—		b	b	b	b	RW	late Pleist.
15X-CC, 24–25	135.12	135.13	vr	—		b	b	b	b	RW	late Pleist.
16X-CC, 27–28	142.05	142.06	tr	—		b	b	b	b	RW	late Pleist.
17X-CC, 22–23	151.31	151.32	b	—		b	b	b	b	RW	late Pleist.
18X-CC, 28–29	160.87	160.88	vr	—		b	b	b	b	RW	late Pleist.
19X-1, 4	167.24		r	p		b	b	b	b	—	Pleist.
19X-1, 6–9	167.26	167.29	r	p		b	b	f	b	—	mid. Pleist.
19X-1, 13	167.33		f	p	CN14b	b	b	r	b	—	mid. Pleist.
19X-1, 27–29	167.47	167.49	r	p		b	b	b	b	—	mid. Pleist.
19X-2, 63	168.70		r	p		b	b	b	b	—	mid. Pleist.
19X-CC, 21–22	169.56	169.57	f	m		b	b	b	b	—	mid. Pleist.
20X-CC, 20–21	185.08	185.09	vr	—		b	b	b	b	—	?
21X-CC, 19–20	193.35	193.36	tr	—		b	b	f	b	—	mid. Pleist.
22X-4, 19			f	m							
22X-CC, 22–23	203.01	203.02	vr	—		b	b	b	b	—	mid. Pleist.
23X-1, 63	206.43		f	m		b	b	b	b	—	mid. Pleist.
23X-2, 113	207.62		f	m		b	b	b	b	—	mid. Pleist.
23X-CC, 40–41	208.39	208.40	tr	p		b	b	b	b	—	mid. Pleist.
24X-CC, 25–26	221.17	221.18	tr	—		b	b	b	b	—	mid. Pleist.
25X-CC, 30–31	227.00	227.01	tr	—		b	b	b	b	—	mid. Pleist.
26X-CC, 40–41	240.08	240.09	tr	—		b	b	b	b	—	mid. Pleist.
27X-CC, 7–8	249.71	249.72	b	—		b	b	b	b	—	mid. Pleist.

Stratigraphic Significance

In Unit I, there are high abundances of all the calcareous and siliceous microfossils (nannofossils, foraminifers, diatoms), and this interval is defined as Zone Z or Holocene. Palynomorphs are not present in this zone. The disappearance of *G. menardii* and *G. tumida* places the Ericson Z/Y boundary between two consecutive core-catcher samples at 6 and 16 mbsf. Given the possible downhole contamination of core-catcher samples (see discussion in "Biostratigraphy" section, "Site 934" chapter, this volume), this boundary is likely to be near the base of Unit I. In the dark olive green to dark gray silty clay of Unit II below the Holocene section, there are extremely low abundances of the siliceous and calcareous microfossil groups. This section is the Y Zone, based on the absence of *G. tumida*. Palynomorphs show low abundance in this zone.

The planktonic foraminifer assemblage within the debris-flow Unit III is of late Pleistocene age. Subunit IVA contains a rich interglacial foraminifer assemblage that, based on the presence of *G. tumida flexuosa* and *G. ruber* (pink), constrains the age to isotopic Stages 5 to 11. The nannofossil assemblage is from Zone CN14b (0.26–0.46 Ma).

PALEOMAGNETISM

Remanence Studies

Archive-half sections for all 10 APC cores from this site were measured using the pass-through cryogenic magnetometer. The declination values were distributed about 0° for the seven azimuthally oriented cores (Cores 933A-3H through -10H), indicating optimum performance of the Tensor tool at this site. Generally low inclination values at an AF demagnetization level of 20 mT imply near-complete removal of the vertical drill string overprint in most cores (Fig. 14).

Oscillations in declination, which may represent secular variation, occur from 56 to 68 mbsf in Hole 933A.

An apparent geomagnetic excursion was recorded in Section 933A-9H-8, at 81.6 mbsf. This record consisted of a rapid shift in inclination from moderate negative values to large positive values, within an interval of ~10 cm. These shifts were accompanied by oscillations in intensity. The pass-through magnetometer data in this zone was degraded by the occurrence of gas voids and sand layers. These disturbances complicated the remanence record such that the distinctive features used to identify the previous records of this apparent excursion (see Figs. 18 and 19 of "Site 930" chapter and Fig. 13 of "Site 932" chapter, this volume) could not be clearly resolved. However AF demagnetization of discrete clay samples to 50 mT confirmed that the fluctuations in remanence direction and intensity recorded by the pass-through magnetometer represented a geomagnetic polarity event.

Figure 15 shows the positions of the inferred excursions in Holes 930C, 932A, and 933A, with respect to fluctuations in remanence intensity. Intensity peaks that we correlate from hole to hole are labelled A through E. The pronounced intensity low that precedes the excursions is labelled L. The similar positions of the excursions with respect to the intensity variations suggest that the Hole 933A excursion is the same (i.e., Lake Mungo at ~30 ka) excursion.

Magnetic Susceptibility

Whole-core and discrete-sample magnetic susceptibilities were measured in the laboratory, and magnetic susceptibility was also measured during downhole logging using the GHMT tool. The patterns of both core and downhole data are broadly similar (Fig. 16). Overall, the debris-flow unit (Unit III) has the highest susceptibility. Both downhole logging and core data show a general increase in values toward the bottom of Subunit IVB. This increase within Subunit IVB is consistent with changes seen in bulk density.

Table 4. Foraminifer abundance data for Hole 933A.

Core, section, interval (cm)	Top interval (mbsf)	Bottom interval (mbsf)	*Globorotalia menardii*	*Globorotalia tumida*	*Globorotalia tumida flexuosa*	*Pulleniatina obliquiloculata*	*Globigerinoides ruber* (white)	*Globigerinoides ruber* (pink)	*Globorotalia hexagonus*	*Neogloboquadrina dutertrei*	*Globorotalia trilobus trilobus*	*Globorotalia inflata*	*Globorotalia truncatulinoides*	*Globigerina bulloides*	*Globigerinoides trilobus sacculifer*	*Orbulina universa*	*Globigerinita glutinata*	*Globigerinoides conglobatus*	*Globoquadrina conglomerata*	*Globortalia crassaformis*	*Neogloboquadrina pachyderma* (right)	*Globigerina rubescens*	*Globorotalia scitula*	*Globorotalia tosaensis*	Other planktonic foraminifers	Vivianite nodules	Overall foraminifer abundance	Preservation	Abundance of bathyal benthic foraminifers	Abundance of abyssal benthic foraminifers	Ericson Zone	Age
155-933A-																																
1H-CC, 14–23	5.60	5.69	F	F	B	F	C	F	B	C	C	B	F	B	F	R	B	B	B	B	B	B	B	B	B	C	G	B	F	Z	Holocene?
2H-CC, 32–41	16.03	16.12	B	B	B	B	R	B	B	F	R	B	F	B	R	B	B	B	B	B	B	B	B	B	R	B	F	M	B	R	Y	late Pleist.
3H-CC, 41–50	25.87	25.96	B	B	B	B	F	B	B	C	F	B	C	B	F	B	B	B	R	B	B	B	B	B	B	B	C	G	B	R	Y	late Pleist.
4H-CC, 45–54	35.02	35.11	B	B	B	B	F	B	B	C	F	B	C	B	C	B	B	B	B	B	B	B	B	B	B	A	F	G	B	B	Y	late Pleist.
5H-CC, 48–57	44.21	44.30	B	B	B	B	C	B	B	A	B	B	B	B	B	B	B	B	B	B	B	B	B	B	B	B	R	P	B	B	Y	late Pleist.
6H-CC, 16–25	54.05	54.14	B	B	B	B	F	B	B	C	C	B	C	B	F	B	B	R	B	B	B	B	B	B	R	B	F	M	B	B	Y	late Pleist.
7H-CC, 22–31	63.80	63.89	B	B	B	B	C	B	B	C	B	B	C	B	C	B	B	B	B	B	B	B	B	B	R	F	R	M	R	B	Y	late Pleist.
8H-CC, 27–36	73.21	73.30	B	B	B	B	B	B	B	B	B	B	B	B	B	B	B	B	B	B	B	B	B	B	B	C	B	?	B	B	?	?
9H-CC, 74–83	83.11	83.20	B	B	B	B	B	B	B	B	B	B	B	B	B	B	B	B	B	B	B	B	B	B	B	R	B	?	B	B	?	?
10H-CC, 39–48	90.70	90.79	B	B	B	B	B	B	B	B	B	B	B	B	B	B	B	B	B	B	B	B	B	B	B	R	B	?	B	B	?	?
11X-CC, 12–21	97.52	97.61	B	B	B	B	R	R	B	C	C	B	C	B	C	B	B	R	B	B	B	R	B	B	R	F	R	P	R	B	?	Pleist.
12X-CC, 11–20	103.83	103.92	B	B	B	B	F	F	R	B	C	F	F	C	B	C	B	B	B	B	B	B	B	B	B	R	C	M	R	B	RW	Pleist.
13X-CC, 2–11	110.81	110.90	B	B	B	B	C	B	B	C	C	B	C	B	B	B	B	B	B	B	B	B	B	B	B	R	R	M	R	B	RW	Pleist.
14X-CC, 12–21	123.08	123.17	B	B	B	B	C	B	B	C	F	B	F	B	F	B	B	B	B	B	B	B	B	B	B	F	R	M	F	B	RW	Pleist.
15X-CC, 15–24	135.03	135.12	B	B	B	C	B	B	B	C	C	B	C	B	B	B	B	B	B	B	B	B	B	B	B	R	R	P	R	B	RW	Pleist.
16X-CC, 18–27	141.96	142.05	B	R	B	F	C	B	B	F	F	B	C	B	F	R	B	B	B	B	B	B	B	B	B	F	C	M	R	B	RW	Pleist.
17X-CC, 13–22	151.22	151.31	B	C	B	F	C	B	B	C	F	B	C	B	B	R	B	B	B	B	B	B	B	B	B	C	F	M	B	B	RW	Pleist.
18X-CC, 19–28	160.78	160.87	B	C	B	F	C	B	B	F	F	B	F	B	B	R	B	B	B	B	B	B	B	B	B	R	F	M	R	B	RW	Pleist.
19X-1, 6–9	167.26	167.29	C	C	R	C	C	R	R	C	C	B	R	B	F	R	B	R	B	R	B	B	B	B	R	F	R	C	G	R	B	RW	Pleist.
19X-1, 11–13	167.31	167.33	C	C	B	C	C	R	R	C	C	B	R	B	R	B	B	R	B	R	B	B	B	B	R	B	B	C	M	B	B	?	mid. Pleist.
19X-1, 27–29	167.47	167.49	F	C	R	B	C	F	R	A	C	B	B	B	F	R	B	B	B	R	B	B	B	B	R	B	B	C	G	B	R	?	mid. Pleist.
19X-CC, 12–21	169.47	169.56	B	C	B	B	F	B	B	F	F	B	B	B	B	F	B	B	R	B	B	B	B	B	B	B	F	M	B	B	?	mid. Pleist.
20X-1, 28–33	177.18	177.23	B	B	B	B	B	B	B	B	B	B	B	B	B	B	B	B	B	B	B	B	B	B	B	B	B	P	B	B	?	?
20X-CC, 11–20	184.99	185.08	B	C	B	B	C	B	B	F	B	B	B	B	B	R	B	B	R	B	B	B	B	B	B	C	F	M	B	B	?	mid. Pleist.
21X-CC, 10–19	193.26	193.35	B	C	B	B	C	B	B	F	B	B	B	B	B	R	B	B	R	B	B	B	B	B	B	A	R	P	B	B	?	mid. Pleist.
22X-CC, 13–22	202.92	203.01	R	F	B	B	F	B	B	C	B	B	B	B	B	R	B	R	R	B	B	B	B	B	R	A	R	M	F	B	?	mid. Pleist.
23X-CC, 31–40	208.30	208.39	B	C	B	B	C	B	B	F	R	B	B	B	B	R	B	R	B	B	B	B	B	B	R	A	F	M	B	B	?	mid. Pleist.
24X-CC, 16–25	221.08	221.17	B	C	B	B	C	B	B	C	B	B	B	B	B	F	B	B	B	B	B	B	B	B	B	C	R	M	B	B	?	mid. Pleist.
25X-CC, 21–30	226.91	227.00	B	C	B	B	F	F	B	C	C	B	B	B	B	R	B	B	B	B	B	B	B	B	B	A	R	M	B	B	?	mid. Pleist.
26X-CC, 31–40	239.99	240.08	F	C	B	B	C	B	B	C	B	B	B	B	B	R	B	B	B	B	B	B	B	B	B	R	R	M	B	B	?	mid. Pleist.
27X-CC, 1–7	249.62	249.71	C	C	B	B	C	B	B	B	B	B	B	B	B	B	B	B	B	B	B	B	B	B	B	F	R	G	B	B	?	mid. Pleist.

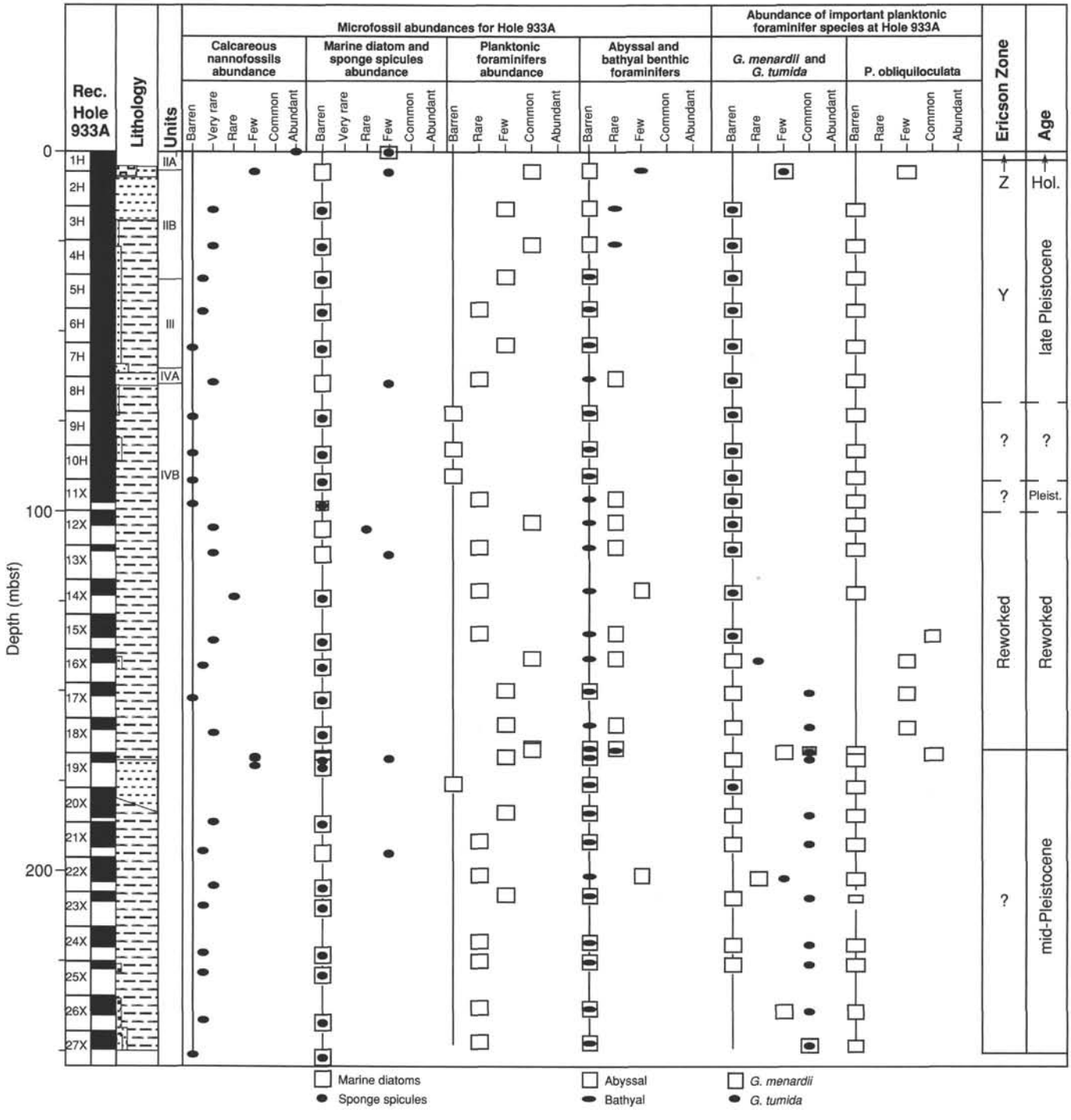

Figure 13. Biostratigraphic summary for Site 933.

ORGANIC GEOCHEMISTRY

Volatile Hydrocarbons

Headspace methane concentrations at Site 933 increase rapidly below the sediment surface to a maximum value of 13,000 ppm at 13.41 mbsf (Table 5; Fig. 17). Methane concentrations remain fairly constant below this depth, ranging from 4,000 ppm to 7,000 ppm with a low value at 109.40 mbsf (1,631 ppm). Vacutainer methane values are up to two orders of magnitude higher than headspace concentrations (Fig. 17), ranging from 17,000 ppm to 975,000 ppm in Hole 933A. Higher molecular weight hydrocarbons were not detected, indicating a predominantly biogenic methane source at Site 933.

Carbon, Nitrogen, and Sulfur Concentrations

Carbonate, calculated as $CaCO_3$, concentrations are high in the top 0.79 mbsf, ranging from 11% to 33% (Table 6; Fig. 18). Carbonate decreases to less than 2% at 1.20 and 4.98 mbsf and then increases

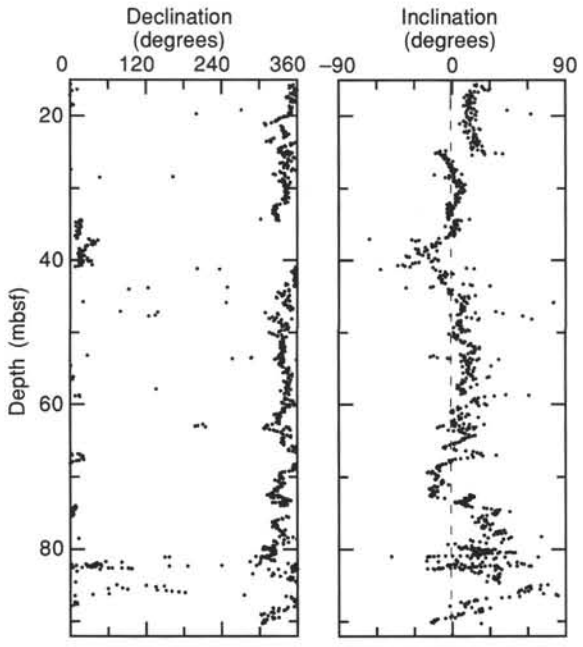

Figure 14. Declination and inclination values, after AF demagnetization to 20 mT, for APC cores from Hole 933A. Declinations have been corrected to true azimuth from Tensor orientation tool data.

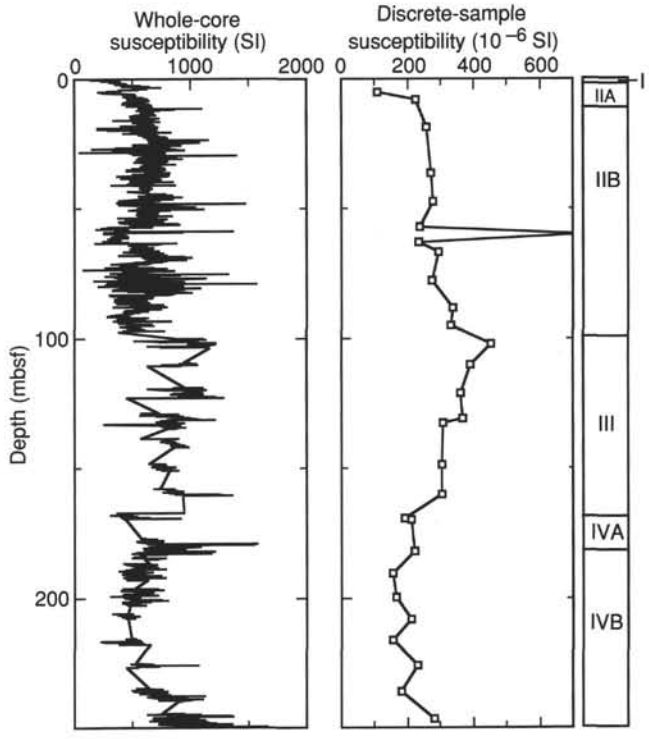

Figure 16. Whole-core and discrete-sample magnetic susceptibilities for Hole 933A.

at 8.84 mbsf (8%) and 8.88 mbsf (4%). Throughout the rest of Hole 933A, carbonate concentrations remain fairly low (<3.5%), except at 94.13 mbsf where they reach 7%. TOC concentrations are low (<0.3%) above 0.79 mbsf, steadily increasing below this depth to 1% at 24.47 mbsf (Table 6; Fig. 18). Between 24.47 and 79.51 mbsf, TOC concentrations average 1% and then decrease to less than 0.8% at 100.40 mbsf, remaining at this level for the rest of Hole 933A. One sample in a sand layer, at 45.79 mbsf, displays a very low TOC concentration (0.09%; Fig. 18). In addition, noticeably lower TOC concentrations are found in bioturbated zones, such as 0.40–8.88 mbsf and 86.88–94.13 mbsf.

Total nitrogen concentrations show a similar profile to TOC (Fig. 18), with relatively low values (0.10%), in the top 5 mbsf, increasing to 0.13% at 18.87 mbsf. TN concentrations remain fairly constant (0.13%–0.15%) between 18.87 mbsf and 79.51 mbsf. Below this depth, TN decreases markedly to values less than 0.06% at 102.99 and 103.40 mbsf. TN concentrations increase slightly below this interval, ranging between 0.07% and 0.09%. Most of the variability in this section is due to relatively low values (<0.08%) found in silt layers. Total sulfur concentrations are low (<0.15%) throughout Hole 933A except for elevated values at 5.98 mbsf (0.8%), 102.99 mbsf (1%), 120.37 mbsf (0.7%), and 168.43 mbsf (0.4%). These samples are from sediment with high abundances of iron sulfide.

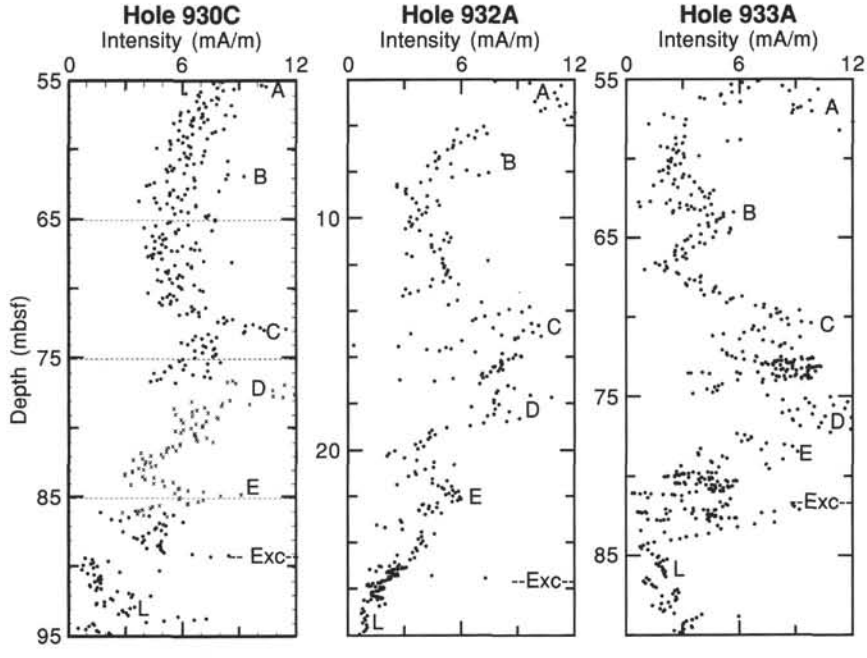

Figure 15. Variations in remanence intensity for correlatable zones within Holes 930C, Hole 932A, and Hole 933A. The beginning points of the geomagnetic excursions (Lake Mungo Excursion at ~30 ka) are noted as "Exc" in each hole. Correlatable intensity peaks are designated by letters A through E. Intensity lows preceding the excursions are labeled L. All points in Hole 930C and Hole 932A represent values after AF demagnetization to 25 mT, except x's, which represent intensities after AF demagnetization to 20 mT. All points in Hole 933A were demagnetized to 20 mT.

Table 5. Gas concentrations in sediments from Site 933.

Core, section, interval (cm)	Depth (mbsf)	Sed. temp.* (°C)	Methane HS (ppm)	Methane VAC (ppm)
155-933A-				
1H-3, 0–5	3.00	2	8	
2H-6, 0–5	13.41	3	12,985	
3H-6, 0–5	21.58	3	6,084	455,662
4H-6, 0–5	32.20	3	5,180	303,282
5H-6, 0–5	41.70	4	5,529	476,211
6H-7, 0–5	51.50	4	4,539	
7H-7, 0–5	61.18	5	4,539	602,994
8H-6, 0–5	69.05	5	5,716	719,163
9H-2, 0–5	72.99	5	5,648	974,916
10H-5, 0–5	86.39	6	5,580	955,251
11X-4, 0–5	95.70	6	6,380	19,294
12X-3, 0–5	102.80	6	4,513	
13X-1, 0–5	109.40	7	1,631	538,985
14X-3, 0–5	122.00	7	3,312	17,220
15X-4, 0–5	133.20	8	6,500	
16X-3, 0–5	141.30	8	6,218	
17X-2, 0–5	149.40	8	4,813	
18X-2, 0–5	159.10	9	3,960	71,536
19X-1, 0–5	167.20	9	10,929	
20X-3, 0–5	179.90	10	5,891	
20X-6, 0–5	184.40	10	7,756	
22X-5, 0–5	201.79	10	4,926	
24X-2, 0–5	216.56	11	5,669	
25X-1, 0–5	225.20	11	4,339	
26X-2, 0–5	236.30	12	6,616	
27X-4, 0–5	249.00	12	5,530	

Notes: HS = Headspace; VAC = Vacutainer. Geothermal gradient = 42°C/km. Bottom-water temperature = 2°C. *See "In-situ Temperature Measurements" section, this chapter.

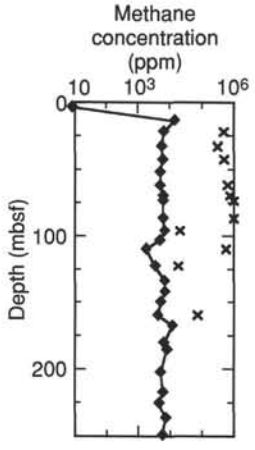

Figure 17. Methane concentrations at Site 933. Headspace (diamond) and vacutainer (×) samples are plotted.

As at previous sites, the carbonate-rich Unit I corresponds to the Holocene period when terrigenous input to the fan was reduced. In addition, a second deeper zone of relatively high carbonate content and low TOC and TN was observed at 8.8 mbsf, corresponding to Unit IIA.

Unit IIB (14.35–97.62 mbsf) is characterized by fairly high TN concentrations, although a sharp decrease in TN occurs approximately 10 m above the lithostratigraphic boundary between Units IIB and III. Unit III exhibits low TN concentrations. The debris flow is further distinguished from the other lithostratigraphic units in Hole 933A by its relatively high [C/N]a ratios (12 to 17; Table 6). These characteristics are similar to those observed in the debris flow at Site 931. Although TN concentrations in Unit IV are similar to those of Unit III, [C/N]a ratios clearly distinguish them.

Because of high inorganic nitrogen contents (see discussion in previous site chapters), it is difficult to assess whether the differences in [C/N]a ratios among the lithologic units at Site 933 are solely due to changes in organic matter sources. However, the downhole trends obtained clearly indicate that differences in organic matter composition exist among lithologic units.

INORGANIC GEOCHEMISTRY

Interstitial Water Analysis

Interstitial water analyses were performed on 13 sediment samples from Hole 933A. Samples were taken approximately every 10 m for the upper 40 mbsf and approximately every 40 m thereafter (Table 7; Fig. 19).

Salinities of the water samples range from 32.0 to 34.0 (Fig. 19A). The two shallowest samples, at 2.95 and 13.15 mbsf, have the highest salinities. Below 13.15 mbsf, salinity varies between 32 and 33.

Chloride concentrations rise from 554 to 560 mM over the first 20 m of the hole (Fig. 19B). They are constant from 21.53 to 68.95 mbsf, then decrease slowly to a minimum of 549 to 550 mM from 141.20 to 182.80 mbsf. Below this depth, the values rise again to around 557 mM over the interval 201.69–248.90 mbsf.

Pore-water pH ranges from 7.35 to 7.97 (Fig. 19C). The highest pH is measured in the shallowest sample (2.95 mbsf). By 21.53 mbsf, the pH drops to 7.35, after which there is a trend toward slightly higher values downhole.

Pore-water alkalinity varies from 9.23 to 17.42 mM. Maximum concentrations are measured in the shallow samples (2.95 and 13.15 mbsf). Alkalinity then decreases rapidly to 9.97 mM at 32.15 mbsf (Fig. 19D) and remains around 10 mM thereafter, with a slightly higher value of 14.71 mM at 182.80 mbsf.

Dissolved magnesium and calcium concentrations decrease quickly from seawater concentrations to around 40 mM and 5 mM, respectively, over the upper 13.15 mbsf (Fig. 19E and 19F). Below 13.15 mbsf, the values are relatively constant. Magnesium concentrations do decrease slightly below 141.20 mbsf, to around 35 mM for the remainder of the hole. Calcium concentrations increase near the bottom of the hole, with a local maximum of 7.6 mM at 236.20 mbsf.

Pore-water sulfate concentration is 11.78 mM at 2.95 mbsf. By 13.15 mbsf, sulfate concentration has fallen to zero, and remains so downhole (Fig. 19G), with the exception of a value of 1.99 mM at 141.20 mbsf, which is likely a sampling artifact.

Ammonium concentrations increase quickly with depth from 0.96 mM at 2.95 mbsf to 7.83 mM at 41.65 mbsf (Fig. 19H). Thereafter, ammonium fluctuates between values of 5.92 mM and 9.66 mM with a trend toward increasing concentrations downhole.

Pore-water phosphate concentration is a maximum in the shallowest sample, 139.9 µM at 2.95 mbsf (Fig. 19I). The concentration drops to 4.0 µM by 13.15 mbsf, and remains between 0 and 9.2 µM through 141.20 mbsf. Phosphate increases to 35.9 µM at 182.80 mbsf, but decreases again to between 13.2 and 17.3 µM below 201.69 mbsf.

The minimum dissolved silica concentration, 229 µM, was measured in the shallowest sample (Fig. 19J). The concentration increases to 470 µM by 21.53 mbsf, and thereafter ranges between 382 and 545 µM with no discernible downhole trend.

Dissolved potassium concentrations decrease from 11.8 mM at 2.95 mbsf to 7.7 mM at 32.15 mbsf (Fig. 19K). The concentration increases again to 9.6 mM at 41.65 mbsf, then shows a trend toward slightly lower values downhole to around 6 mM near the bottom of the hole.

Dissolved sodium concentrations are relatively constant throughout the hole, ranging from 461 to 473 mM, and show no trend with depth (Fig. 19L).

Pore-water iron concentrations are about 19 µM in the upper 13.15 mbsf, increasing to 64.5 µM at 21.53 mbsf (Fig. 19M). Below 21.53 mbsf, the concentration decreases to 34.0 µM. There is a trend of decreasing values downhole.

Table 6. Elemental and organic carbon compositions of sediments from Site 933.

Core, section, interval (cm)	Depth (mbsf)	IC (%)	$CaCO_3$* (%)	TC (%)	TOC (%)	TN (%)	TS (%)	[C/N]a	Lith. unit
155-933A-									
1H-1, 40–41	0.40	3.98	33.2	4.11	0.13	0.10	0.08	2	I
1H-1, 79–80	0.79	1.27	10.6	1.51	0.24	0.10	0.14	3	
1H-1, 120–121	1.20	0.04	0.3	0.58	0.54	0.11	0.22	6	
1H-4, 48–49	4.98	0.19	1.6	0.67	0.48	0.10	0.82	6	
2H-2, 143–144	8.84	0.96	8.0	1.63	0.67	0.12	0.12	7	
2H-2, 147–148	8.88	0.51	4.2	1.02	0.51	0.11	0.10	5	
3H-4, 29–30	18.87	0.28	2.3	1.25	0.97	0.12	0.10	9	
3H-4, 35–36	18.93	0.25	2.1	1.17	0.92	0.13	0.11	8	
3H-7, 139–140	24.47	0.27	2.2	1.27	1.00	0.13	0.00	9	
4H-3, 50–51	28.20	0.30	2.5	1.34	1.04	0.14	0.10	9	
4H-6, 48–50	32.68	0.27	2.2	1.29	1.02	0.13	0.10	9	
5H-3, 12–13	37.32	0.28	2.3	1.26	0.98	0.13	0.11	9	
5H-6, 100–101	42.70	0.42	3.5	1.44	1.02	0.13	0.07	9	II
6H-3, 29–30	45.79	0.06	0.5	0.15	0.09	0.01	0.06	10	
6H-5, 50–51	49.00	0.25	2.1	1.38	1.13	0.15	0.10	9	
7H-3, 84–85	56.02	0.33	2.7	1.39	1.06	0.13	0.20	9	
8H-1, 29–30	62.99	0.32	2.7	1.25	0.93	0.13	0.17	8	
8H-4, 49–50	66.54	0.37	3.1	1.39	1.02	0.13	0.14	9	
9H-4, 52–53	76.01	0.28	2.3	1.29	1.01	0.12	0.15	10	
9H-6, 52–53	78.73	0.11	0.9	1.01	0.90	0.14	0.09	8	
9H-6, 130–131	79.51	0.09	0.7	0.96	0.87	0.12	0.00	8	
10H-2, 49–50	83.69	0.25	2.1	1.09	0.84	0.08	0.10	12	
10H-5, 49–50	86.88	0.16	1.3	0.88	0.72	0.06	0.05	15	
11H-2, 143–144	94.13	0.85	7.1	1.60	0.75	0.07	0.00	13	
11H-3, 63–64	94.83	0.18	1.5	1.06	0.88	0.07	0.00	16	
12H-1, 60–61	100.40	0.32	2.7	1.00	0.68	0.06	0.00	14	
12H-3, 19–20	102.99	0.24	2.0	0.99	0.75	0.05	1.01	16	
12H-3, 60–61	103.40	0.24	2.0	1.03	0.79	0.05	0.11	17	
14H-1, 137–138	120.37	0.23	1.9	1.02	0.79	0.06	0.68	15	
14X-2, 52–53	121.02	0.26	2.2	1.07	0.81	0.08	0.11	12	
15X-2, 101–102	131.21	0.28	2.3	0.98	0.70	0.06	0.12	13	III
15X-3, 12–13	131.82	0.34	2.8	1.16	0.82	0.07	0.09	14	
15X-3, 142–143	133.12	0.13	1.1	1.10	0.97	0.09	0.27	13	
16X-1, 90–91	139.20	0.29	2.4	1.18	0.89	0.08	0.08	13	
17X-2, 55–56	149.95	0.28	2.3	1.04	0.76	0.09	0.09	10	
18X-1, 140–141	159.00	0.30	2.5	1.12	0.82	0.08	0.07	12	
19X-2, 36–37	168.43	0.30	2.5	0.93	0.63	0.08	0.37	9	
20X-3, 109–110	180.96	0.23	1.9	1.02	0.79	0.08	0.07	11	
20X-3, 106–107	180.99	0.40	3.3	1.13	0.73	0.08	0.11	11	
21X-2, 56–57	188.56	0.42	3.5	1.17	0.75	0.07	0.12	12	
21X-4, 61–62	191.40	0.28	2.3	1.05	0.77	0.09	0.09	10	
22X-2, 52–53	197.81	0.38	3.2	1.12	0.74	0.11	0.08	8	IV
22X-4, 85–86	201.14	0.40	3.3	1.14	0.74	0.07	0.00	12	
23X-2, 105–106	207.54	0.32	2.7	1.09	0.77	0.10	0.06	9	
24X-4, 98–99	220.40	0.34	2.8	1.15	0.81	0.09	0.06	11	
25X-1, 131–132	226.51	0.38	3.2	1.15	0.77	0.08	0.00	11	
26X-1, 73–74	235.53	0.37	3.1	1.13	0.76	0.08	0.00	11	

*Calculated assuming all IC is calcite.

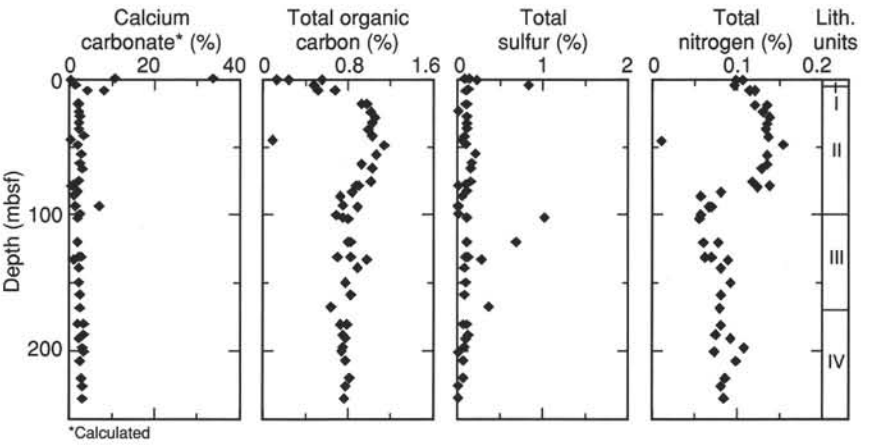

Figure 18. Concentration profiles of calcium carbonate, total organic carbon, total sulfur, and total nitrogen in Hole 933A.

Dissolved manganese concentrations are 22.0 µM at 2.95 mbsf (Fig. 19N). The concentration decreases to 3.5 µM at 13.15 mbsf and remains less than 5 µM downhole.

Sediment Geochemistry

Six mud samples were analyzed for major- and trace-element geochemistry (Tables 8 and 9). Samples were collected at approximately 15-m intervals through lithologic Unit IIB; one sample was taken from lithologic Unit III. The geochemistry of muds from Unit IIB is similar to that of muds from previous sites, with SiO_2 from 60 to 62 wt%, and Al_2O_3 between 21 and 23 wt%. CaO abundances are relatively constant between 0.7 and 1.0 wt%, consistent with a mineralogy dominated by silicates. Within the resolution of the analyses, the composition of Unit IIB muds is uniform downcore.

Table 7. Interstitial water chemistry, Site 933.

Core, section, interval (cm)	Depth (mbsf)	Salinity	pH	Alkalinity (mM)	Cl^- (mM)	Mg^{2+} (mM)	Ca^{2+} (mM)	K^+ (mM)	HPO_4^{2-} (μM)	SO_4^{2-} (mM)	NH_4^+ (mM)	H_4SiO_4 (μM)	Na^+ (mM)	Fe^{2+} (μM)	Mn^{2+} (μM)
155-933A-															
1H-2, 145–150	2.95	34.0	7.97	16.72	554	45.1	8.8	11.8	88.9	11.6	0.96	229	473	19.5	22.0
2H-5, 145–150	13.15	34.0	7.56	17.42	556	40.2	5.6	9.2	4.0	0.0	4.11	379	469	18.3	3.5
3H-5, 145–150	21.53	33.0	7.35	12.68	560	41.1	5.3	8.1	9.2	0.0	5.74	470	466	64.5	4.0
4H-5, 145–150	32.15	32.5	7.46	9.97	560	41.0	5.7	7.7	0.6	0.0	7.03	441	462	34.0	5.0
5H-5, 145–150	41.65	32.5	7.39	9.71	561	39.7	5.0	7.9	1.5	0.1	7.83	417	466	37.6	5.0
8H-5, 140–150	68.95	32.5	7.42	9.74	559	39.1	5.0	9.6	0.0	0.0	6.23	423	465	41.4	4.0
11X-3, 140–150	95.60	32.5	7.55	10.22	556	38.8	4.4	9.1	3.6	0.3	6.72	382	465	54.0	3.5
14X-2, 140–150	121.90	33.0	7.55	11.24	553	39.9	5.2	8.0	0.6	1.0	7.15	517	461	35.6	4.5
16X-2, 140–150	141.20	32.5	7.59	9.23	549	38.8	5.4	6.1	1.5	2.0	5.92	489	462	42.5	4.5
20X-4, 140–150	182.80	32.5	7.76	14.71	550	35.8	5.0	7.3	35.9	0.7	7.63	494	470	13.7	2.5
22X-4, 140–150	201.69	32.5	7.67	11.72	557	34.2	4.9	6.7	13.2	0.1	9.66	395	474	8.1	2.0
26X-1, 140–150	236.20	33.0	7.58	11.33	558	34.1	7.6	6.3	17.3	0.4	8.63	483	472	20.5	3.0
27X-3, 140–150	248.90	32.0	7.68	10.15	557	35.7	6.5	6.2	10.7	0.2	9.06	545	468	17.9	3.5

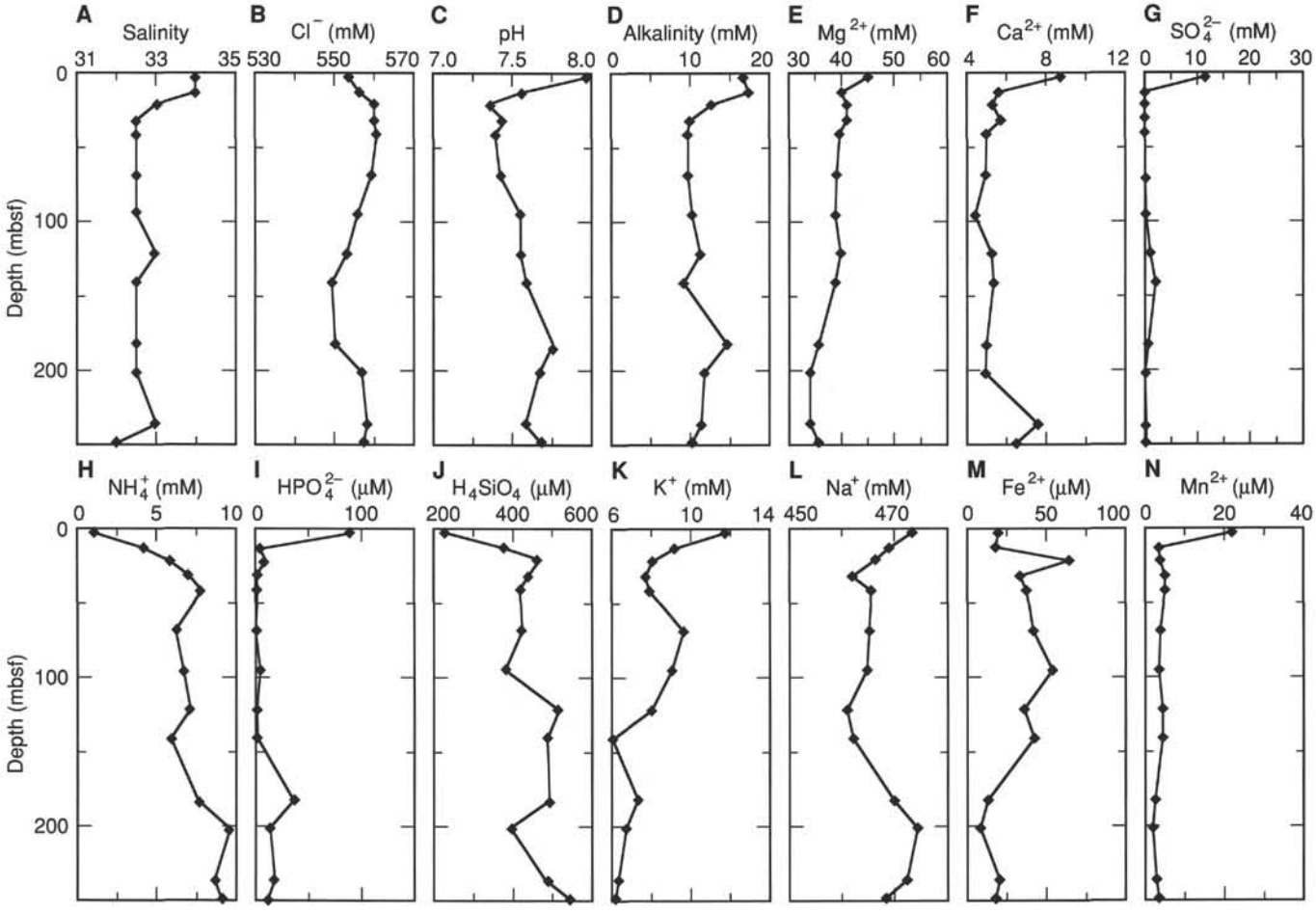

Figure 19. Downcore variation in pore-water chemistry: **A.** Salinity. **B.** Chloride. **C.** pH. **D.** Alkalinity. **E.** Magnesium. **F.** Calcium. **G.** Sulfate. **H.** Ammonium. **I.** Phosphate. **J.** Silica. **K.** Potassium. **L.** Sodium. **M.** Iron. **N.** Manganese.

The sample from Unit III is significantly higher than Unit IIB muds in SiO_2 (67 wt%) and lower in Al_2O_3 (19 wt%) as well as many other elements and oxides (e.g., Fe_2O_3, MgO, Ce, Cr, and Rb; Tables 8 and 9). Unit III is a very silty clay and has been interpreted as a mass-flow deposit. The geochemical composition of this sample reflects a greater quartz-rich silt fraction than for muds of Unit IIB.

PHYSICAL PROPERTIES

Index Properties

Index properties were determined for sediment from lithologic Units II through IV in Hole 933A (Table 10). The decrease in water content with depth in Hole 933A displays transitions that mark the boundaries between lithologic units in a pattern similar to that at Site 931 (Fig. 20). Unit II (0.52–97.62 mbsf) displays a uniform, exponential decrease in water content from 53% at its top to 29% at its base. A distinct 4% decrease in water content marks the upper 4 m of Unit III (99.80–167.31 mbsf). The debris-flow deposits of Unit III are characterized by greater variability in water content than the laminated and thin-bedded silty clays of Units II and IV. Water content increases sharply from 23% at the base of Unit III to 34% at the top of Unit IV (167.31–249.72 mbsf). Water content decreases downhole in Unit IV to 24% at the base of Hole 933A. The water content profile in Unit IV is marked by one discontinuity, an increase of approximately 3% at 215 mbsf.

Table 8. Major element composition (wt%) of sediment samples, Site 933.

Core, section, interval (cm)	Depth (mbsf)	Lithology	SiO_2	TiO_2	Al_2O_3	Fe_2O_3	MnO	MgO	CaO	Na_2O	K_2O	P_2O_5	Total	LOI
155-933A-														
3H-7, 143–146	24.51	Mud	60.68	1.10	22.43	8.45	0.12	2.24	0.96	1.52	2.98	0.26	100.73	8.81
5H-6, 102–107	42.72	Mud	59.63	1.06	22.40	8.12	0.10	2.18	0.84	1.59	3.01	0.19	99.12	8.41
7H-3, 86–91	56.04	Mud	60.94	1.07	22.57	8.08	0.10	2.19	0.81	1.48	3.09	0.20	100.53	8.60
9H-6, 132–136	79.53	Mud	61.88	1.02	21.44	8.14	0.12	1.98	0.85	1.48	3.03	0.18	100.12	7.76
11X-3, 64–69	94.84	Mud	61.53	1.05	22.11	7.49	0.09	2.11	0.67	1.50	3.13	0.20	99.88	7.43
15X-2, 90–95	131.10	Mud	66.70	0.94	18.86	6.70	0.08	1.76	0.95	1.32	2.68	0.17	100.16	6.91

Notes: Total iron is reported as Fe_2O_3. LOI = loss on ignition.

Table 9. Trace element composition (ppm) of sediment samples, Site 933.

Core, section, interval (cm)	Depth (mbsf)	Lithology	Ba	Ce	Cr	Cu	Nb	Ni	Rb	Sr	V	Y	Zn	Zr
155-933A-														
3H-7, 143–146	24.51	Mud	500	113	65	33	23	34	126	151	74	40	126	215
5H-6, 102–107	42.72	Mud	495	105	66	33	21	34	129	146	66	35	125	201
7H-3, 86–91	56.04	Mud	489	114	68	33	22	34	132	148	75	36	128	213
9H-6, 132–136	79.53	Mud	490	104	64	33	22	35	130	162	92	37	124	224
11X-3, 64–69	94.84	Mud	496	100	64	31	22	33	136	141	75	36	124	217
15X-2, 90–95	131.10	Mud	449	98	54	24	20	27	114	153	70	36	105	266

Porosity variation in Hole 933A essentially parallels the variation in water content (Fig. 20). The change in porosity from the top to the bottom of Units II, III, and IV are 75% to 52%, 51% to 45%, and 58% to 46%, respectively.

Variation in wet-bulk density in Hole 933A primarily reflects differences in water content (Fig. 20) as a result of the narrow range in grain density. Grain density averages 2.75 g/cm^3, and the bulk of the values is between 2.70 and 2.80 g/cm^3. Wet-bulk density increases with depth from 1.47 to 1.87 g/cm^3 in Unit II, 1.92 to 2.04 g/cm^3 in Unit III, and 1.79 to 2.04 g/cm^3 in Unit IV. The discontinuity in water content and porosity profiles in Unit IV is more pronounced in the wet-bulk density data. At 215 mbsf, wet-bulk density decreases from about 2.00 to 1.90 g/cm^3. As at the previous Amazon Fan sites, the GRAPE records for most of the section at Site 933 reflect the general trends in wet-bulk density but are characterized by densities that are 0.2 to 0.4 g/cm^3 lower than the discrete-sample values.

The pattern displayed by the index properties at Site 933, like that at Site 931, is representative of fine-grained sediment consolidating under its own weight. Low and variable water content of Unit III is consistent with the interpretation of a debris-flow origin for the sediment. This unit contains a mixture of sediment types, including some materials that consolidated elsewhere before being transported downslope. Fine-grained sediment below Unit III has a higher water content, most likely as a result of dewatering being inhibited by either rapid deposition of the debris flow or low permeability of the overlying debris-flow deposits. The likelihood that sediment of Unit IV is underconsolidated and characterized by excess pore pressure is indicated by the deformation of the borehole. At 215 mbsf, there is a pronounced, elliptical reduction in borehole size, which is typical for overpressured formations (see "Downhole Logging" section, this chapter). This borehole anomaly coincides with the discontinuities in the water content, porosity, and wet-bulk density profiles in Unit IV. High pressures implied at this depth may contribute to the overall higher water content of Unit IV.

Compressional-wave Velocity

Two velocity measurements with the DSV were made in the upper 2 m of Core 933A-1H. Below 2 mbsf, sediment fractures resulting from gas expansion made velocity measurements on split sections impossible. The average of the DSV measurements is 1501 m/s. Usable PWL data were obtained over the upper 6 m of Hole 933A. The average of these data is also 1501 m/s. The DSV and PWL give an average corrected in-situ sediment velocity of 1498 m/s.

Shear Strength

Measurements of undrained shear strength (Table 11) were made on all cores recovered from Hole 933A except Cores 933A-2H, -3H, and -12X through -14X. Unconfined compressive strength measurements were made on all cores below Core 933A-10H, except for Cores 933A-13X and -14X. These cores were unsuitable for strength measurements because the sediment was either too coarse grained or too highly disturbed.

The shear strength profile for Hole 933A can be divided into two parts (Fig. 21). The upper part, from near the seafloor to 101 mbsf, is characterized by a relatively consistent increase in shear strength with depth. Over this interval, undrained shear strength increases from 4.6 to 48.4 kPa, and there is good agreement between measurements of undrained shear strength and unconfined compressive strength. Below 101 mbsf, the strength data display a greater variability and more poorly defined trends with depth. In general, higher strength values are associated with sediment of Unit III. Maxima in undrained shear strength and unconfined compressive stress occur in this interval at approximately 141 mbsf. Below the base of Unit III (167.31 mbsf), there is a gradual, but highly variable, increase in strength.

The trends in the shear strength profile reflect a general relationship of increasing strength with increasing bulk density. The increase in variability of the strength measurements below 100 mbsf may in part reflect effects of core disturbance, but it also reflects the increased occurrence of failure by fracture in the strength tests.

Resistivity

Longitudinal and transverse resistivity was determined for Hole 933A (Table 12). Variation of longitudinal resistivity with depth is similar to that of the index properties, with changes roughly coinciding with lithologic unit boundaries (Fig. 22). In Unit II, resistivity increases from 0.26 Ωm at 1 mbsf to 0.60 Ωm at 75 mbsf, before decreasing to approximately 0.40 Ωm in the lower 10 m of the unit. Unit III is marked by little change in longitudinal resistivity with depth, with most of the values clustering between 0.45 and 0.50 Ωm. The resistivity decreases sharply to 0.36 Ωm at the top of Unit IV.

Table 10. Index properties at Site 933.

Core, section, interval (cm)	Depth (mbsf)	Water content (%)	Wet-bulk density (g/cm^3)	Grain density (g/cm^3)	Dry-bulk density (g/cm^3)	Porosity (%)	Void ratio
155-933A-							
1H-1, 102–104	1.02	53.2	1.47	2.72	0.69	75.1	3.01
1H-2, 76–78	2.26	51.1	1.48	2.75	0.72	73.7	2.81
1H-3, 77–79	3.77	47.8	1.55	2.73	0.81	70.9	2.43
1H-4, 75–77	5.25	38.0	1.57	3.06	0.98	64.7	1.83
2H-1, 111–113	6.81	44.2	1.59	2.77	0.89	68.1	2.14
2H-2, 57–59	7.98	44.3	1.61	2.79	0.90	68.4	2.16
2H-3, 61–63	9.52	43.7	1.62	2.88	0.91	68.5	2.18
2H-4, 64–66	11.05	42.8	1.62	2.74	0.93	66.7	2.00
2H-5, 65–67	12.56	41.0	1.65	2.71	0.97	64.8	1.84
2H-6, 95–97	14.36	40.4	1.67	2.77	1.00	64.7	1.83
2H-7, 52–54	15.43	39.3	1.69	2.76	1.03	63.6	1.75
3H-2, 82–84	16.40	39.3	1.66	2.71	1.01	63.1	1.71
3H-3, 78–80	17.86	38.0	1.73	2.78	1.07	62.4	1.66
3H-4, 52–54	19.10	38.0	1.70	2.70	1.05	61.8	1.62
3H-5, 70–72	20.78	37.7	1.73	2.76	1.08	62.0	1.63
3H-6, 58–60	22.16	37.3	1.70	2.69	1.07	61.0	1.56
3H-7, 141–143	24.49	37.8	1.63	2.70	1.01	61.5	1.60
3H-8, 45–47	25.03	36.2	1.76	2.75	1.12	60.4	1.52
4H-1, 85–87	25.55	37.0	1.75	2.76	1.10	61.3	1.58
4H-2, 39–41	26.59	37.0	1.72	2.68	1.08	60.6	1.54
4H-3, 54–56	28.24	36.0	1.76	2.77	1.12	60.3	1.52
4H-4, 31–32	29.50	35.5	1.75	2.72	1.13	59.3	1.46
4H-5, 73–75	31.43	35.9	1.75	2.76	1.12	60.1	1.51
4H-6, 49–51	32.69	35.3	1.77	2.75	1.14	59.4	1.46
4H-7, 68–70	34.38	35.7	1.76	2.69	1.13	59.3	1.46
5H-1, 48–50	34.68	36.0	1.75	2.71	1.12	59.8	1.49
5H-2, 69–71	36.39	35.5	1.75	2.76	1.13	59.7	1.48
5H-3, 144–146	38.64	34.3	1.70	2.75	1.11	58.4	1.40
5H-4, 103–105	39.73	33.8	1.78	2.77	1.18	58.0	1.38
5H-5, 63–65	40.83	34.1	1.78	2.73	1.17	58.0	1.38
5H-6, 59–61	42.29	34.3	1.78	2.79	1.17	58.7	1.42
5H-7, 9–11	43.29	34.9	1.75	2.72	1.14	58.7	1.42
6H-2, 55–57	44.55	35.1	1.76	2.72	1.14	59.0	1.44
6H-3, 93–95	46.43	32.7	1.83	2.73	1.23	56.4	1.30
6H-5, 58–60	49.08	34.6	1.77	2.70	1.16	58.2	1.39
6H-6, 61–63	50.61	33.7	1.80	2.69	1.19	57.2	1.33
6H-7, 39–41	51.89	33.7	1.80	2.81	1.20	58.3	1.40
6H-8, 25–27	53.25	33.3	1.79	2.70	1.19	56.8	1.31
7H-1, 19–21	53.39	35.0	1.77	2.70	1.15	58.6	1.42
7H-2, 19–21	53.87	34.3	1.78	2.69	1.17	57.7	1.37
7H-3, 59–61	55.77	33.4	1.78	2.70	1.19	56.9	1.32
7H-4, 32–34	57.00	32.7	1.82	2.75	1.23	56.6	1.30
7H-5, 83–85	59.01	32.4	1.80	2.69	1.22	55.7	1.26
7H-6, 89–91	60.57	33.0	1.82	2.79	1.22	57.4	1.35
7H-7, 83–85	62.01	32.7	1.83	2.76	1.23	56.7	1.31
7H-8, 76–78	63.44	32.3	1.85	2.77	1.25	56.3	1.29
8H-1, 16–18	62.86	30.1	1.84	2.71	1.29	53.3	1.14
8H-2, 14–16	63.19	29.3	1.87	2.71	1.33	52.3	1.09
8H-2, 94–96	63.99	33.6	1.80	2.75	1.20	57.5	1.35
8H-3, 114–116	65.69	31.8	1.83	2.77	1.25	55.8	1.26
8H-4, 109,111	67.14	32.3	1.83	2.76	1.24	56.2	1.28
8H-5, 64,66	68.19	30.7	1.84	2.73	1.28	54.1	1.18
8H-6, 66,68	69.71	30.3	1.85	2.73	1.29	53.6	1.16
8H-7, 56,58	71.11	32.5	1.83	2.80	1.24	56.8	1.32
8H-8, 73,75	72.78	31.8	1.84	2.79	1.26	55.9	1.27
9H-2, 38,40	72.87	31.7	1.82	2.74	1.24	55.4	1.24
9H-3, 111–113	75.10	32.8	1.81	2.77	1.22	56.9	1.32
9H-4, 129–131	76.78	30.9	1.83	2.71	1.26	54.3	1.19
9H-5, 79–81	77.78	31.6	1.82	2.71	1.25	55.0	1.22
9H-6, 29–31	78.50	30.4	1.86	2.76	1.29	54.1	1.18
9H-7, 108–110	80.79	31.3	1.82	2.72	1.25	54.8	1.21
10H-1, 111–113	82.81	29.0	1.91	2.78	1.35	52.6	1.11
10H-2, 91–93	84.11	30.2	1.87	2.79	1.30	54.1	1.18
10H-4, 79–81	85.68	29.8	1.88	2.80	1.32	53.6	1.16
10H-5, 101–103	87.40	29.3	1.87	2.73	1.32	52.5	1.10
10H-6, 61–63	88.50	27.2	1.96	2.77	1.42	50.2	1.01
10H-7, 54–56	89.93	28.2	1.91	2.78	1.37	51.6	1.06
10H-1, 141–143	92.61	29.8	1.87	2.75	1.32	53.2	1.14
10H-2, 33–35	93.03	29.5	1.85	2.71	1.31	52.5	1.11
10H-3, 84–86	95.04	30.4	1.85	2.76	1.29	54.1	1.18
10H-4, 98–100	96.68	29.8	1.86	2.77	1.31	53.4	1.15
10H-5, 18–20	97.38	28.9	1.87	2.73	1.33	52.0	1.08
12X-1, 117–119	100.97	27.7	1.92	2.77	1.39	50.8	1.03
12X-2, 108–110	102.38	25.6	1.95	2.73	1.45	47.8	0.92
12X-3, 66–68	103.46	23.7	2.01	2.76	1.53	45.5	0.84
13X-1, 77–79	110.17	24.4	1.97	2.73	1.49	46.2	0.86
14X-1, 140–142	120.40	25.0	1.72	2.72	1.29	46.9	0.88
14X-2, 42–44	120.92	27.3	1.91	2.74	1.39	50.1	1.00
14X-3, 43–45	122.43	25.2	1.97	2.70	1.47	47.1	0.89
15X-1, 132–134	130.02	25.5	1.98	2.78	1.47	48.2	0.93
15X-2, 136–138	131.56	25.4	2.00	2.78	1.49	48.1	0.93
15X-3, 112–114	132.82	26.9	1.94	2.77	1.42	49.8	0.99
15X-4, 75–77	133.95	23.1	2.02	2.71	1.55	44.2	0.79
15X-5, 15–17	134.85	21.8	2.05	2.72	1.60	42.5	0.74
16X-1, 83–85	139.13	22.8	2.04	2.76	1.57	44.3	0.80
16X-2, 79–81	140.59	22.2	2.06	2.77	1.60	43.5	0.77
16X-3, 22–24	141.52	21.3	2.11	2.78	1.66	42.3	0.73

Table 10 (continued).

Core, section, interval (cm)	Depth (mbsf)	Water content (%)	Wet-bulk density (g/cm^3)	Grain density (g/cm^3)	Dry-bulk density (g/cm^3)	Porosity (%)	Void ratio
17X-1, 72–74	148.62	23.4	2.02	2.77	1.55	45.2	0.83
17X-2, 73–75	150.13	21.9	2.05	2.71	1.60	42.5	0.74
17X-3, 10–12	151.00	23.7	2.03	2.79	1.55	45.8	0.85
18X-1, 37–39	157.97	24.1	2.00	2.76	1.52	46.1	0.86
18X-2, 87–89	159.97	22.5	2.04	2.78	1.58	44.1	0.79
18X-2, 128–130	160.38	20.8	2.08	2.73	1.65	41.1	0.70
18X-2, 147–149	160.57	23.2	2.04	2.72	1.56	44.6	0.80
19X-1, 51–53	167.71	33.9	1.79	2.76	1.18	58.1	1.38
19X-2, 89–91	168.96	31.1	1.87	2.78	1.29	55.1	1.23
20X-1, 74–76	177.64	30.8	1.85	2.76	1.28	54.5	1.20
20X-2, 49–51	178.89	30.1	1.86	2.75	1.30	53.6	1.16
20X-3, 77–79	180.67	28.5	1.90	2.79	1.36	52.0	1.08
20X-4, 77–79	182.17	28.7	1.90	2.78	1.36	52.1	1.09
20X-5, 79–81	183.69	28.3	1.90	2.73	1.36	51.4	1.06
20X-6, 18–20	184.58	27.8	1.94	2.78	1.40	51.2	1.05
21X-1, 89–91	187.39	29.2	1.89	2.73	1.34	52.4	1.10
21X-2, 95–97	188.95	29.3	1.88	2.71	1.33	52.3	1.09
21X-3, 98–100	190.48	28.4	1.91	2.80	1.37	52.0	1.08
21X-4, 53–55	191.32	28.1	1.92	2.78	1.38	51.5	1.06
21X-5, 30–32	192.59	28.1	1.95	2.78	1.40	51.5	1.06
22X-1, 73–75	196.93	27.0	1.92	2.73	1.40	49.7	0.99
22X-2, 79–81	198.08	27.3	1.96	2.80	1.42	50.7	1.03
22X-3, 79–81	199.58	26.2	1.97	2.74	1.45	48.7	0.95
22X-4, 60–62	200.89	27.6	1.96	2.78	1.42	50.9	1.04
22X-5, 65–67	202.44	26.4	1.99	2.78	1.46	49.3	0.97
23X-2, 6–8	206.55	26.2	2.01	2.79	1.48	49.1	0.97
23X-2, 121–123	207.70	26.2	1.99	2.83	1.47	49.5	0.98
24X-1, 49–51	215.99	29.1	1.90	2.79	1.34	52.8	1.12
24X-2, 75–77	217.31	26.6	1.84	2.74	1.35	49.3	0.97
24X-3, 81–83	218.73	27.6	1.91	2.74	1.38	50.5	1.02
24X-4, 123–125	220.65	27.2	1.97	2.80	1.43	50.5	1.02
25X-1, 122–124	226.42	26.9	1.93	2.72	1.41	49.4	0.98
26X-1, 124–126	236.04	26.8	1.92	2.73	1.40	49.5	0.98
26X-2, 116–118	237.46	24.6	2.00	2.76	1.51	46.8	0.88
26X-3, 69–71	238.53	24.7	2.00	2.77	1.51	47.1	0.89
27X-1, 44–46	244.94	24.4	1.99	2.74	1.51	46.3	0.86
27X-2, 40–42	246.40	25.5	1.98	2.77	1.48	48.1	0.93
27X-3, 129–131	248.79	23.9	2.04	2.77	1.55	46.0	0.85

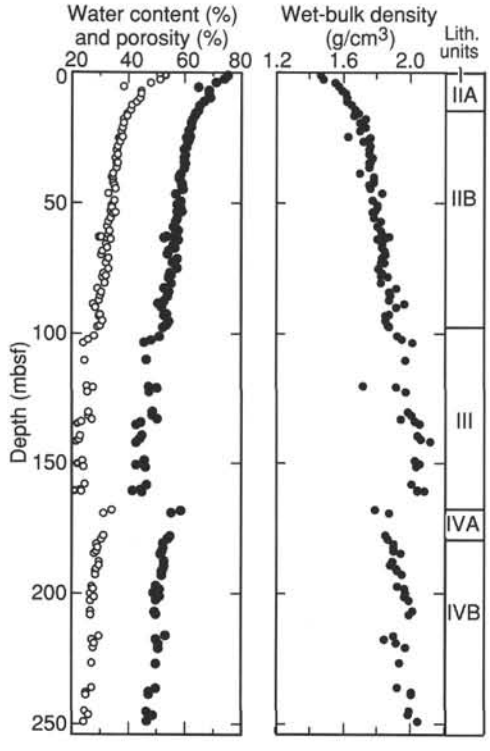

Figure 20. Water content (open circles), porosity (solid circles), and wet-bulk density in Hole 933A.

With increasing depth in Unit IV, resistivity increases to a maxima of 0.58 Ωm at 208 mbsf. Below the discontinuity in bulk properties at 215 mbsf most of the longitudinal resistivity values are between 0.45 and 0.55 Ωm and do not display a consistent relationship with depth. The general pattern in the resistivity measurements is an inverse correlation with porosity. Exceptions to this relationship are the decrease in resistivity at the base of Unit II and the decrease in resistivity at the top of Unit IV.

Differences among the lithologic units are also displayed in the variation of the anisotropy of resistivity (Fig. 22). Similar to the pattern observed at Site 931, the laminated and thin-bedded silty clays of Units II and IV at Site 933 are characterized by a greater anisotropy than the debris-flow deposits of Unit III. The trend in the anisotropy of Units II and IV is toward more negative values. The anisotropy is better developed in Unit II than in Unit IV. Average values of the anisotropy are –4.2% and –1.2% for Units II and IV, respectively.

DOWNHOLE LOGGING

Logging Operations and Quality of Logs

At Site 933, we acquired a suite of high-quality logs using the Quad-combination, Formation MicroScanner (FMS), and geological high-sensitivity magnetic (GHMT-A) tool strings. After coring and drilling were completed in Hole 933A, the borehole was circulated with seawater to remove debris and to clear any possible borehole irregularities. The hole was conditioned with sepiolite drilling mud mixed with seawater. The base of the bottom-hole assembly (BHA) was set at 3463.4 mbrf (86.6 mbsf) and raised to 68.6 mbsf during logging of the upper portion of the hole.

Table 11. Strength measurements at Site 933.

Core, section, interval (cm)	Depth (mbsf)	Unconfined compressive strength* (kPa)	Undrained shear strength (kPa)
155-933A-			
1H-1, 100	1.00		4.6
1H-2, 77	2.27		5.7
1H-3, 78	3.78		6.5
1H-4, 76	5.26		11.8
4H-1, 86	25.56		16.5
4H-2, 40	26.60		15.0
4H-3, 55	28.25		14.5
4H-4, 31	29.51		13.4
4H-5, 74	31.44		15.9
4H-6, 50	32.70		18.3
4H-7, 69	34.39		18.7
5H-1, 49	34.69		23.5
5H-2, 70	36.40		24.9
5H-3, 145	38.65		14.3
5H-4, 104	39.74		13.7
5H-5, 64	40.84		15.6
5H-6, 60	42.30		22.5
5H-7, 10	43.30		22.7
6H-2, 56	44.56		33.7
6H-3, 94	46.44		25.2
6H-5, 59	49.09		32.8
6H-6, 62	50.62		20.9
6H-7, 40	51.90		24.0
6H-8, 26	53.26		18.1
7H-1, 20	53.40		28.3
7H-2, 20	53.88		35.9
7H-3, 60	55.78		30.3
7H-4, 33	57.01		25.2
7H-5, 84	59.02		32.5
7H-6, 90	60.58		38.5
7H-7, 84	62.02		41.6
8H-1, 17	62.87		45.5
8H-2, 15	63.20		44.1
7H-8, 77	63.45		49.2
8H-2, 95	64.00		35.1
8H-3, 115	65.70		32.8
8H-4, 110	67.15		32.2
8H-5, 65	68.20		29.1
8H-6, 65	69.70		39.0
8H-7, 57	71.12		37.3
8H-8, 74	72.79		31.1
9H-2, 39	72.88		41.3
9H-3, 112	75.11		30.6
9H-4, 130	76.79		39.9
9H-5, 80	77.79		26.6
9H-6, 30	78.51		34.2
9H-7, 109	80.80		23.5
10H-1, 112	82.82	98.1	30.6
10H-2, 91	84.11	88.3	34.5
10H-4, 85	85.74	78.5	50.1
10H-5, 103	87.42	107.9	47.5
10H-6, 61	88.50	78.5	44.4
10H-7, 55	89.94	88.3	38.8
11X-1, 142	92.62	58.8	39.6
11X-2, 34	93.04	49.0	39.6
11X-3, 85	95.05	78.5	40.5
11X-4, 91	96.61	88.3	48.4
12X-1, 117	100.97	103.0	
15X-1, 134	130.04	98.1	51.8
15X-2, 136	131.56	166.7	72.1
15X-3, 114	132.84	176.5	86.3
15X-4, 75	133.95	152.0	67.9
15X-5, 17	134.87	152.0	62.2
16X-1, 83	139.13	161.8	72.1
16X-2, 80	140.60	225.6	108.6
16X-3, 23	141.53	235.4	90.5
17X-1, 73	148.63	103.0	34.5
17X-2, 74	150.14	147.1	48.7
17X-3, 12	151.02	137.3	48.4
18X-1, 39	157.99	58.8	16.1
18X-2, 87	159.97	107.9	41.0
18X-2, 130	160.40	58.8	53.5
18X-2, 147	160.57	147.1	33.1
19X-1, 51	167.71	39.2	
19X-2, 90	168.97	88.3	48.1
20X-1, 77	177.67	58.8	28.6
20X-2, 50	178.90	58.8	39.6
20X-3, 77	180.67	98.1	47.5
20X-4, 77	182.17	98.1	43.6
20X-5, 79	183.69	117.7	56.9
20X-6, 19	184.59	137.3	62.0
21X-1, 90	187.40	68.6	33.7
21X-2, 96	188.96	49.0	26.6
21X-3, 99	190.49	78.5	48.1
21X-4, 54	191.33	152.0	70.7
21X-5, 31	192.60	137.3	61.7
22X-1, 74	196.94	58.8	37.3
22X-2, 80	198.09	88.3	42.7
22X-3, 80	199.59	88.3	41.6
22X-4, 61	200.90	107.9	48.1
22X-5, 66	202.45	137.3	65.9
23X-2, 7	206.56	112.8	39.0
23X-2, 122	207.71	127.5	61.1
24X-1, 50	216.00		22.1
14X-2, 76	217.32		48.9
24X-3, 82	218.74	147.1	43.0
24X-4, 124	220.66	122.6	49.2
25X-1, 123	226.43	152.0	58.0
26X-1, 105	235.85	103.0	47.0
26X-2, 117	237.47	127.5	67.0
26X-3, 70	238.54	147.1	71.3
27X-1, 45	244.95	93.2	44.7
27X-2, 42	246.42	122.6	55.7
27X-3, 130	248.80	142.2	53.5

Note: *Unconfined compressive strength (q_u) can be used to approximate undrained shear strength (S_u) by the relationship $q_u = 2S_u$.

The Quad combination was lowered into the hole and it was paused at the mud line for 5 min to measure the mud-line borehole temperature. A bridge was encountered at about 220 mbsf, but the Quad combination was able to push through it and was lowered to 250 mbsf, 4 m above TD. During the first upgoing run, the high-temperature lithodensity tool (HLDT) pad did not open until halfway up the hole. This reduced the quality of the bulk density (RhoB) and photoelectric effect (PEF) logs between 250 and ~150 mbsf. The second run provided high-quality logging data for the interval between 245 and 123 mbsf (Table 13).

The FMS tool string provided high-resolution resistivity images of the borehole wall between 238 and 73 mbsf. We conducted a second run in an attempt to obtain more complete coverage of the borehole, which appeared to be nearly circular, based on the caliper log. The orthogonal calipers showed a measurement difference of only about 2 or 3 cm. The resistivity pads, however, apparently tracked the same path, except for a short interval (193–238 mbsf).

When we lowered the geological high-sensitivity magnetic tool (GHMT-A), it encountered a bridge at 216 mbsf. A borehole deviation of about 4.5°, combined with the relatively low weight and larger diameter of this tool string, may have prevented its passage beyond this bridge. Good quality GHMT-A logs were obtained from two passes between 214 and 86 mbsf (Table 13).

The caliper log shows that for most of the logged interval, the borehole varied in diameter from ~10 to 12 in. (26.5–30.5 cm). The interval between 104 and 122 mbsf was slightly narrower than the bit diameter (9.875 in., 25.1 cm), probably as a result of swelling clays. At the base of the logged interval (233–210 mbsf), the borehole was significantly narrower than the bit diameter. Except for a few thin, washed-out intervals between 75 and 90 mbsf, the borehole generally was in good condition, which allowed us to obtain good-quality logs.

Results

The logged interval shows distinct downhole trends in physical and chemical properties and is useful to delineate lithologic boundaries (Fig. 23). We divided the logged section into three logging stratigraphic units (logging units) based on trends in the logging curves.

Logging Unit 1 (68.6–97 mbsf) is characterized by (1) a subtle downhole increase in resistivity (1.2–1.3 Ωm), (2) an overall downhole increase in background gamma-ray counts, sonic velocity, and density, and (3) a downhole decrease in porosity and magnetic susceptibility (Fig. 23). A 13-m interval (77–90 mbsf), characterized by distinctly low gamma-ray counts and widely fluctuating values in velocity, density, and porosity, is associated with silty-sand turbidites in

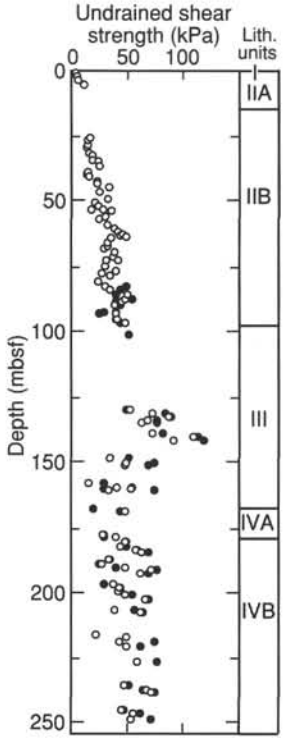

Figure 21. Undrained shear strength (open circles) and assumed undrained shear strength derived from unconfined compressive strength (solid circles) in Hole 933A.

lithostratigraphic Subunit IIB (see "Lithostratigraphy" section, this chapter). This variability occurs within the few thin, washed-out intervals and may result partly from hole size variations.

The base and top of logging Unit 2 (97–164 mbsf) are characterized by sharp changes in logging values. Above ~125 mbsf, resistivity is about 1.75 Ωm; values gradually increase downhole to 2.2 Ωm near the base of this logging unit. A similar downward trend also is observed in the velocity and density logs; their maximum values are recorded at the base of the log unit. Between 97 and 125 mbsf, magnetic susceptibility is ~900 ppm; below 125 mbsf, it shifts to ~1100 ppm and coincides with an accompanying slight increase in spectral gamma ray (SGR). Although the borehole was not washed out in this upper interval (97–125 mbsf), core recovery was less than 50%, suggesting the possible occurrence of coarser grained intervals. The relatively higher uranium content in logging Unit 2, as inferred from the difference between computed gamma-ray (CGR) and SGR values, suggests that it is enriched in organic matter.

The abrupt contact at 164 mbsf between logging Units 2 and 3 (164–246 mbsf) is characterized by a distinct shift to lower values in resistivity, velocity, density, and magnetic susceptibility, accompanied by an increase in neutron porosity. Anomalously low resistivity values were recorded during both runs between 174 to 192 mbsf. The interval from 164 to 192 mbsf has anomalously low, spherically focused (SFLU) resistivity, compared to the deep- and medium-resistivity data. Resistivity values below 192 mbsf gradually increase downhole from 1.25 to 1.5 Ωm at the base of logging Unit 3. The velocity and density also gradually increase, with values that are distinctly less than those in logging Unit 2. The SGR log reveals only a subtle negative shift at the top of the logging unit, but fluctuations in uranium content suggest variation in organic matter content. Magnetic susceptibility increases rapidly from 600 ppm at the top of logging Unit 3, then gradually decreases from ~900 ppm at 172 mbsf to ~600 ppm at 210 mbsf. In general, the data from logging Unit 3 are similar to those in logging Unit 1, reflecting the similarity of lithology between lithostratigraphic Units II and IV.

Table 12. Electrical resistivity at Site 933.

Core, section, interval (cm)	Depth (mbsf)	Longitudinal resistivity (Ωm)	Transverse resistivity (Ωm)
155-933A-			
1H-1, 102	1.02	0.26	0.27
1H-2, 77	2.27	0.26	0.25
1H-3, 78	3.78	0.25	0.25
1H-4, 76	5.26	0.25	0.26
2H-1, 111	6.81	0.30	0.28
2H-2, 58	7.99	0.26	0.26
2H-3, 61	9.52	0.26	0.26
2H-4, 65	11.06	0.28	0.28
2H-5, 66	12.57	0.29	0.28
2H-6, 97	14.38	0.29	0.28
2H-7, 53	15.44	0.29	0.30
3H-2, 82	16.40	0.31	0.31
3H-3, 79	17.87	0.31	0.31
3H-4, 54	19.12	0.30	0.30
3H-5, 71	20.79	0.32	0.31
3H-6, 59	22.17	0.31	0.31
3H-7, 142	24.50	0.32	0.32
3H-8, 47	25.05	0.32	0.32
4H-1, 86	25.56	0.35	0.37
4H-2, 40	26.60	0.40	0.38
4H-3, 55	28.25	0.41	0.38
4H-4, 31	29.51	0.38	0.38
4H-5, 74	31.44	0.39	0.35
4H-6, 50	32.70	0.43	0.37
4H-7, 69	34.39	0.46	0.42
5H-1, 49	34.69	0.40	0.41
5H-2, 70	36.40	0.40	0.36
5H-3, 145	38.65	0.42	0.40
5H-4, 104	39.74	0.41	0.39
5H-5, 64	40.84	0.40	0.38
5H-6, 60	42.30	0.43	0.39
5H-7, 10	43.30	0.38	0.42
6H-2, 56	44.56	0.43	0.41
6H-3, 94	46.44	0.49	0.42
6H-5, 59	49.09	0.43	0.39
6H-6, 62	50.62	0.49	0.45
6H-7, 40	51.90	0.46	0.44
6H-8, 26	53.26	0.49	0.45
7H-1, 20	53.40	0.44	0.42
7H-2, 20	53.88	0.49	0.44
7H-3, 60	55.78	0.45	0.46
7H-4, 33	57.01	0.45	0.42
7H-5, 84	59.02	0.50	0.43
7H-6, 90	60.58	0.45	0.48
7H-7, 84	62.02	0.42	0.41
7H-8, 77	63.45	0.46	0.44
8H-1, 17	62.87	0.42	0.41
8H-2, 15	63.20	0.45	0.44
8H-2, 95	64.00	0.43	0.41
8H-3, 115	65.70	0.53	0.43
8H-4, 110	67.15	0.45	0.43
8H-5, 65	68.20	0.49	0.42
8H-6, 65	69.70	0.46	0.45
8H-7, 57	71.12	0.44	0.41
8H-8, 74	72.79	0.46	0.45
9H-2, 39	72.88	0.51	0.45
9H-3, 112	75.11	0.60	0.45
9H-4, 130	76.79	0.57	0.50
9H-5, 80	77.79	0.57	0.52
9H-6, 30	78.51	0.47	0.51
9H-7, 109	80.80	0.55	0.50
10H-1, 111	82.81	0.44	0.43
10H-2, 91	84.11	0.42	0.44
10H-4, 80	85.69	0.42	0.42
10H-5, 102	87.41	0.42	0.42
10H-6, 61	88.50	0.43	0.43
10H-7, 54	89.93	0.44	0.44
11X-1, 142	92.62	0.41	0.39
11X-2, 34	93.04	0.38	0.39
11X-3, 85	95.05	0.38	0.37
11X-4, 91	96.61	0.39	0.40
12X-1, 118	100.98	0.45	0.45
12X-2, 119	102.49	0.45	0.44
12X-3, 68	103.48	0.44	0.45
13X-1, 77	110.17	0.44	0.45
14X-1, 140	120.40	0.43	0.42
14X-2, 43	120.93	0.42	0.44
14X-3, 44	122.44	0.43	0.43
15X-1, 132	130.02	0.43	0.43
15X-2, 138	131.58	0.47	0.50
15X-3, 113	132.83	0.41	0.44
15X-4, 75	133.95	0.48	0.53
15X-5, 16	134.86	0.48	0.50
16X-1, 83	139.13	0.52	0.50
16X-2, 84	140.64	0.53	0.54
16X-3, 24	141.54	0.50	0.56
17X-1, 72	148.62	0.49	0.50
17X-2, 74	150.14	0.49	0.50

Table 12 (continued).

Core, section, interval (cm)	Depth (mbsf)	Longitudinal resistivity (Ωm)	Transverse resistivity (Ωm)
17X-3, 12	151.02	0.48	0.49
18X-1, 38	157.98	0.45	0.44
18X-2, 87	159.97	0.48	0.49
18X-2, 130	160.40	0.47	0.48
18X-2, 148	160.58	0.54	0.49
19X-1, 52	167.72	0.36	0.37
19X-2, 90	168.97	0.36	0.38
20X-1, 77	177.67	0.38	0.39
20X-2, 52	178.92	0.36	0.36
20X-3, 77	180.67	0.38	0.39
20X-4, 77	182.17	0.39	0.43
20X-5, 86	183.76	0.40	0.39
20X-6, 20	184.60	0.40	0.43
21X-1, 90	187.40	0.44	0.45
21X-2, 96	188.96	0.45	0.41
21X-3, 99	190.49	0.45	0.45
21X-4, 54	191.33	0.52	0.46
21X-5, 31	192.60	0.49	0.54
22X-1, 74	196.94	0.47	0.44
22X-2, 80	198.09	0.46	0.46
22X-3, 80	199.59	0.51	0.48
22X-4, 61	200.90	0.48	0.45
22X-5, 66	202.45	0.51	0.46
23X-2, 7	206.56	0.55	0.61
23X-2, 122	207.71	0.58	0.49
24X-2, 76	217.32	0.53	0.46
24X-1, 50	216.00	0.47	0.52
24X-3, 82	218.74	0.48	0.52
24X-4, 124	220.66	0.56	0.49
25X-1, 123	226.43	0.51	0.48
26X-1, 105	235.85	0.51	0.52
26X-2, 117	237.47	0.54	0.65
26X-3, 70	238.54	0.58	0.52
27X-1, 45	244.95	0.49	0.49
27X-2, 42	246.42	0.48	0.45
27X-3, 130	248.80	0.48	0.47

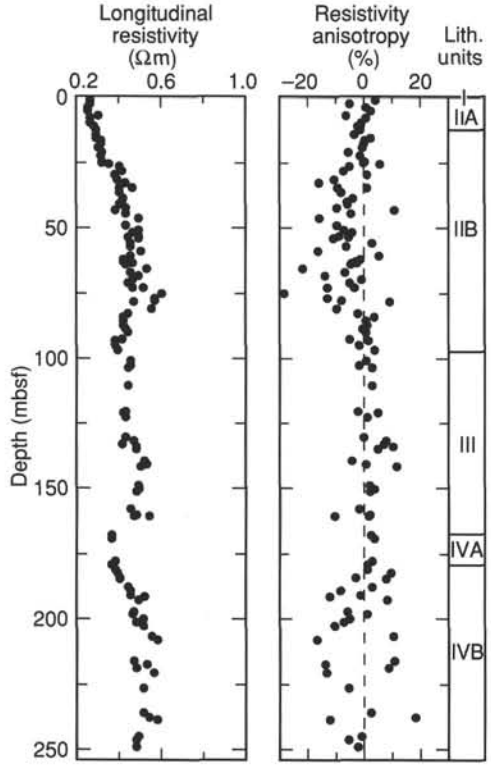

Figure 22. Longitudinal resistivity and resistivity anisotropy in Hole 933A.

Mineralogy

The gamma-ray logs, in conjunction with the photoelectric effect (PEF) (Fig. 24), show that sediment mineralogy in Hole 933A either falls within the zone of mixed-layer clays or is composed of a mixture of different clay minerals (Fig. 25). XRD results have not been interpreted to result from mixed-layer clays, but rather, there seems to be a mixture of kaolinite, illite, and montmorillonite. Crossplots of the logging data suggest that kaolinite and illite are the major clay components (Fig. 25). The Th/K log shows pronounced peaks that correspond to increases in the amount of kaolinite and/or montmorillonite at the expense of illite (Fig. 24). Such changes may indicate temporal variations in weathering patterns within the Amazon Basin. Detailed analysis of core samples and logging data will be needed to quantify these mineralogical observations.

Formation MicroScanner Tool

Formation MicroScanner images (see CD-ROM, back pocket) indicate abrupt resistivity changes at the top and base of logging Unit 2 (97 and 164.5 mbsf) that are interpreted as marking the top and base of a mass-flow unit (lithostratigraphic Unit III). Preliminary examination of the images reveals a few folds, inclined contacts, and possible clasts that alternate with horizontally bedded intervals. The data further suggest that above 125 mbsf, the inferred clasts are larger than below this depth.

The two orthogonal caliper logs (C1, C2) from the FMS reveal that the borehole in the upper section of the logged interval is nearly circular (Fig. 26). The section between 140 and 231 mbsf is slightly elliptical, with a C1/C2 ratio of about 0.9. The long axis is oriented west-southwest/east-northeast (~80°). The borehole is distinctly elliptical between 216 and 231 mbsf, with a minimum diameter of about 5 in. (12.7 cm). The ratio of the two caliper measurements in this interval is almost 1.5 (Fig. 26), and the long axis is oriented southwest-northeast (~50°).

Borehole Temperature

Borehole temperatures were recorded by the TLT attached to the bottom of the Quad-combination tool. Data from the slow-response thermistor is shown in Figure 27. We did not circulate seawater in the hole between logging runs; however, below 160 mbsf, the temperature during the second log run was an average 1°C colder than that recorded during the first run. Above 100 mbsf, the second run recorded temperatures about 0.5°C warmer than those of the first run.

Abrupt temperature changes occur at about 105, 128, and 165 mbsf and may represent distinct changes in lithology. These correspond approximately to the top, middle, and bottom of Unit III. The abrupt increase in temperature beneath Unit III indicates a warmer and possibly overpressured formation.

Geological High-sensitivity Magnetic Tool (GHMT-A) Results

Total induction and susceptibility data were recorded, respectively, by the scalar magnetometer (NMRS) and the susceptometer (SUMS). Repeat logging runs permitted us to analyze different components of the borehole magnetic environment that affect the measurement of magnetization of the surrounding formation.

Total Induction Log

In Figure 28, we illustrate the remaining "local" field $\mathbf{B}_L$ for the two runs. Two different magnetic signatures were observed in the logged interval. The highly magnetic BHA caused a shift toward high values, between 85 and 130 mbsf (first run) and 94 and 130 mbsf (second run). Apart from sharp positive peaks, the interval between 130 and 210 mbsf has little magnetic variation, and the average val-

Table 13. Intervals logged and tools employed in Hole 933A.

String	Run	Open hole (mbsf)	Open hole (mbrf)	In pipe (mbsf)	In pipe (mbrf)	Tools
Quad	Down and up 1	250–68	3627–3445	68–0	3445–3377	NGT/LSS/CNT-G/HLDT/DITE/TLT
	Up 2	245–123	3622–3500			
FMS	Up 1	238–93	3615–3470			NGT/GPIT/FMS
	Up 2	238–193	3615–3570			
		208–73	3585–3450			
GHMT-A	Up 1	214–93	3591–3570			NGT/SUMS/NMRS
	Up 2	214–86	3591–3463			

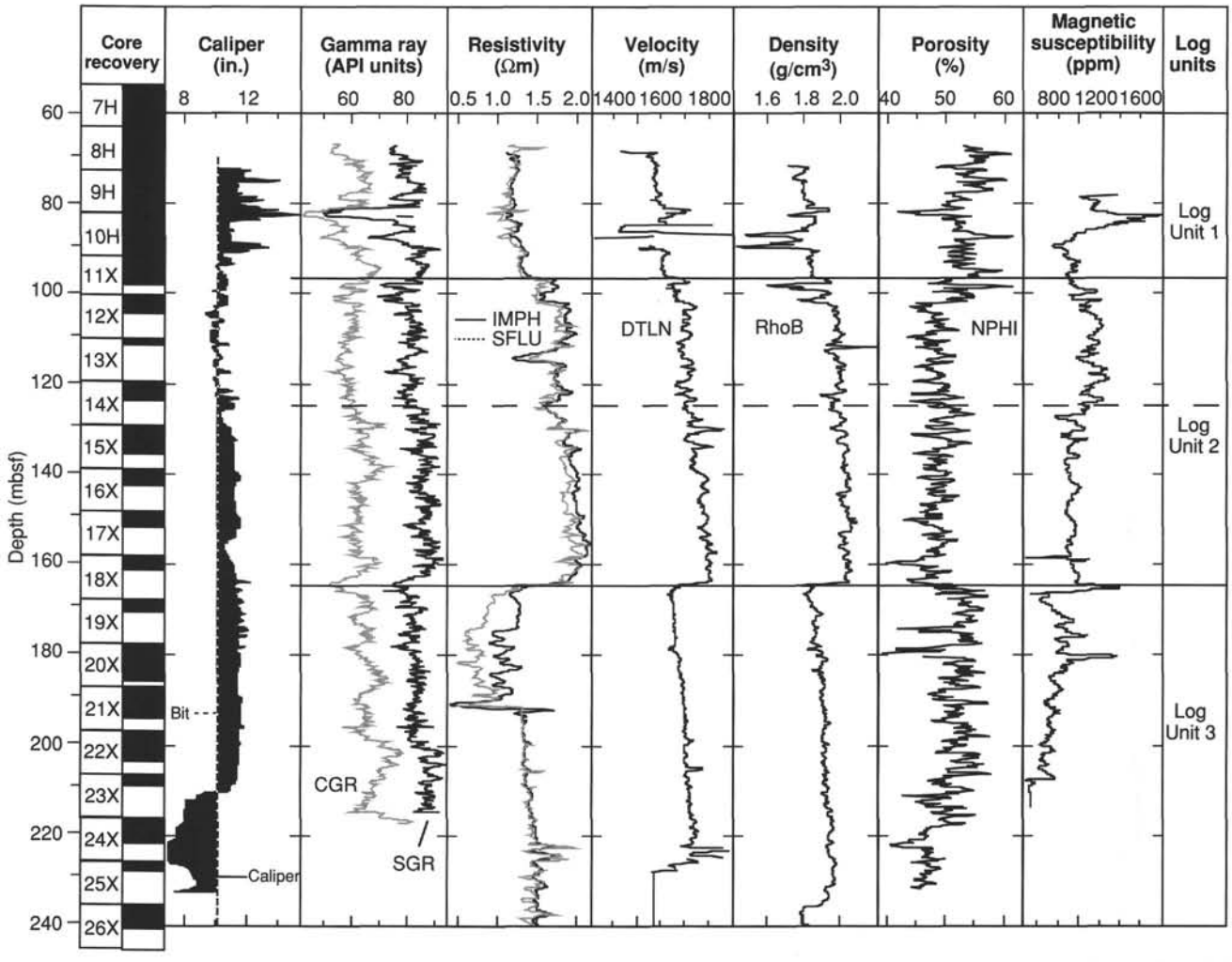

Figure 23. Results from Hole 933B Quad-combination tool. CGR (Th + K) = computed gamma ray, SGR = spectroscopy gamma ray, IMPH = medium- induction phasor resistivity, SFLU = shallow, spherically focused resistivity, DTLN = short spacing interval transit time converted to velocity, RhoB = bulk density, and NPHI = neutron porosity. For descriptive purposes, the logged section has been divided into three logging units.

ues of the "local" fields $\mathbf{B}_{L1}$ and $\mathbf{B}_{L2}$ are slightly lower than zero. The true value of **Bf**, the magnetization component of the formation, can be obtained by evaluating the anomaly field **Ba** and the transient fields **Bt**1 and **Bt**2.

Analysis of the Components of the Magnetic Induction

Data from the two runs $\mathbf{B}_{L1}$ and $\mathbf{B}_{L2}$ are similar and indicate that no significant temporal changes occurred in Earth's external field (Fig. 27). Figure 28 also shows the remaining "local" **B** field for the first run after correction for pipe effect ($\mathbf{B}_{L1}$cor). This drill-pipe perturbation can usually be corrected for by assuming a dipolar effect, which allows for data recovery up to about 10 m beneath the BHA. Only low frequency variations ($<5 \times 10^{-3}$ Hz or ~>30 m interval) affect the recorded values (skin effect) because the measurements were performed under more than 3000 m of conductive seawater.

An overall negative value of the remaining "local" field $\mathbf{B}_{L1}$cor is centered around –60 nT (Fig. 28). The average value of **Bf** is slightly higher than expected. Average susceptibility and remanent intensity values of 8×10^{-4} SI and 10^{-2} A/m, respectively, from core measurements should exert an effect of about 25 nT on the total field sensor. Because Hole 933A is located in a negative anomaly field (**Ba** < 85 nT), a precise estimation of **Ba** will require further analysis.

Comparison of Magnetic Logging with Core Data

A good correlation exists between the two susceptibility records (k1, k2), indicating that there was little thermal drift of the measure-

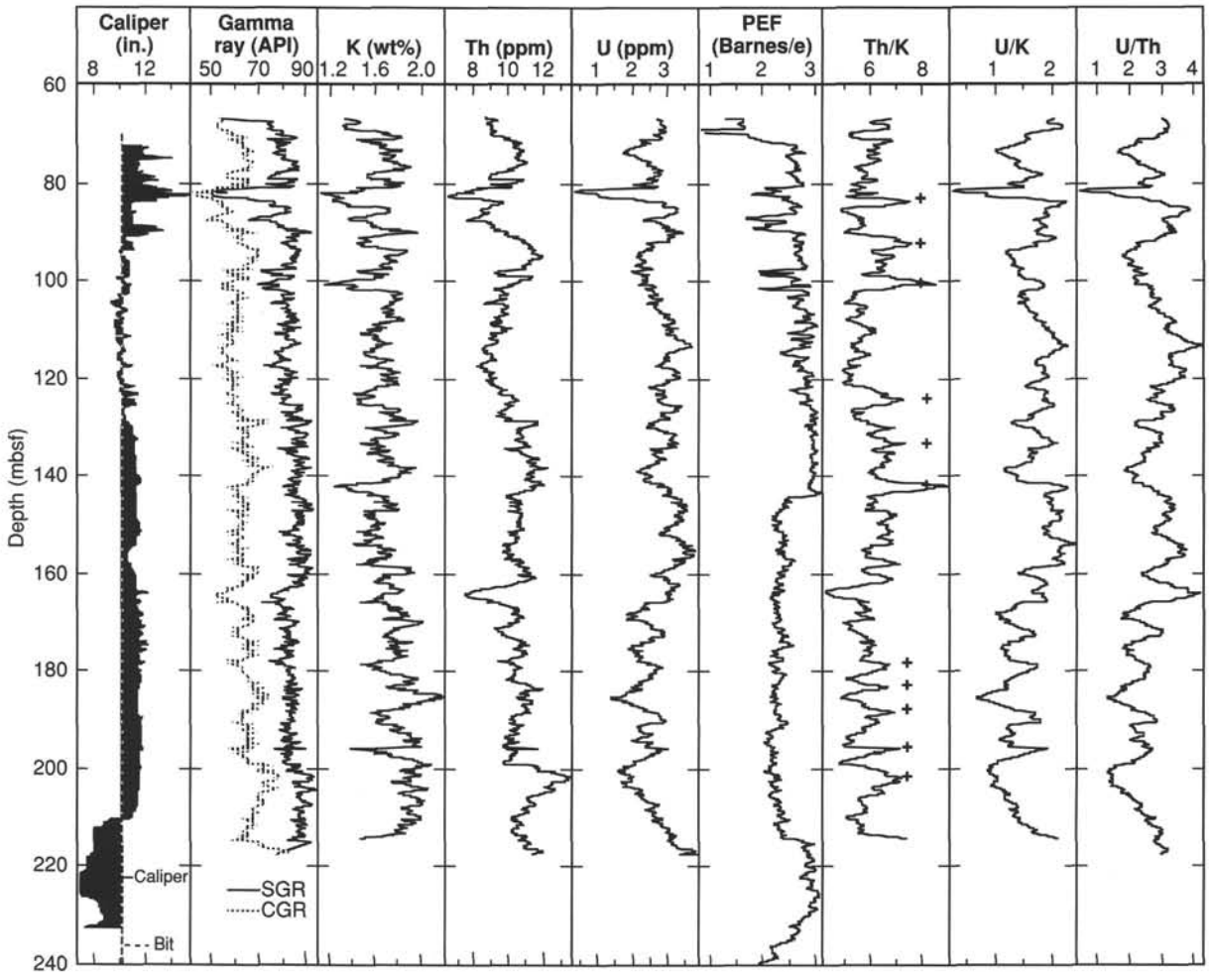

Figure 24. Gamma-ray and photoelectric effect (PEF) logs. Peaks of Th/K ratios are probably related to increases in the amount of kaolinite and/or montmorillonite at the expense of illite (plus signs).

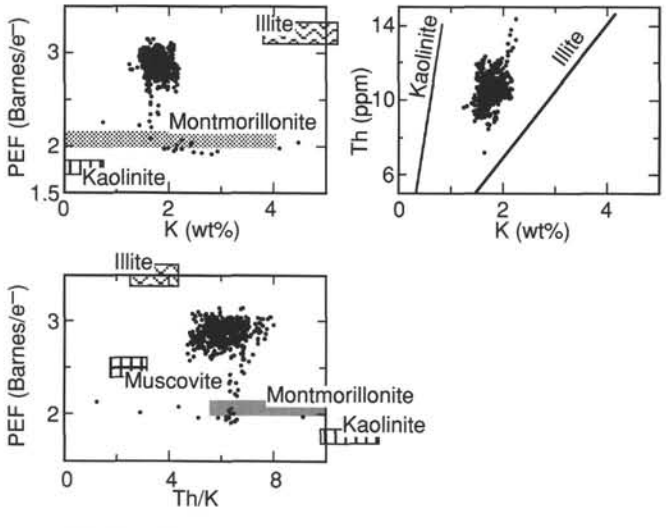

Figure 25. Crossplots of spectrometry gamma-ray and photoelectric effect (PEF) data in Hole 933A. Shaded areas show ideal response of pure minerals (Schlumberger, 1989). Most measurements cluster in a region, suggesting a mixture of clay minerals, most likely including illite, kaolinite, and/or montmorillonite. Muscovite has a higher potassium value (10%) and is probably not a major component of the mixture.

ment coils (Fig. 29). In Figure 29, we also show the comparison between logging and whole-core magnetic susceptibilities. Laboratory measurements reveal a higher vertical resolution record, although this was affected by different degrees of core expansion associated with gassy sediment (see "Paleomagnetism" section, this chapter), while the continuous downhole record reveals broader variations.

A reverse polarity interval initially was suspected below Core 933A-18X on the basis of variations in declination and intensity of the remanent magnetization measured on these cores. The correlation between the corrected "local" **B** field ($\mathbf{B}_{L1}$cor) and the induced magnetization field calculated from k1 ($\mathbf{Bf}_i$, in units of nT; Fig. 30) was evaluated by making three crossplots ($\mathbf{B}_{L1}$cor vs. $\mathbf{Bf}_i$) for each of the depth intervals that span lithostratigraphic Units II (87–99 mbsf), III (99–166 mbsf), and IV (166–210 mbsf). Each lithostratigraphic unit has a distinct cross-correlation pattern. Lithostratigraphic Unit III displays no correlation between the total field and induced magnetizations, suggesting that no remanent magnetization resulted from probable extensive reworking during mass transport. The observed difference between the overlying Units II and IV could be the result of a magnetic polarity reversal. Shore-based processing may determine if, alternatively, the difference was caused by lithologic variations.

Comparison with Lithology and Discussion

Logging Units 1 through 3 correspond approximately to lithostratigraphic Units II through IV (see "Lithostratigraphy" section,

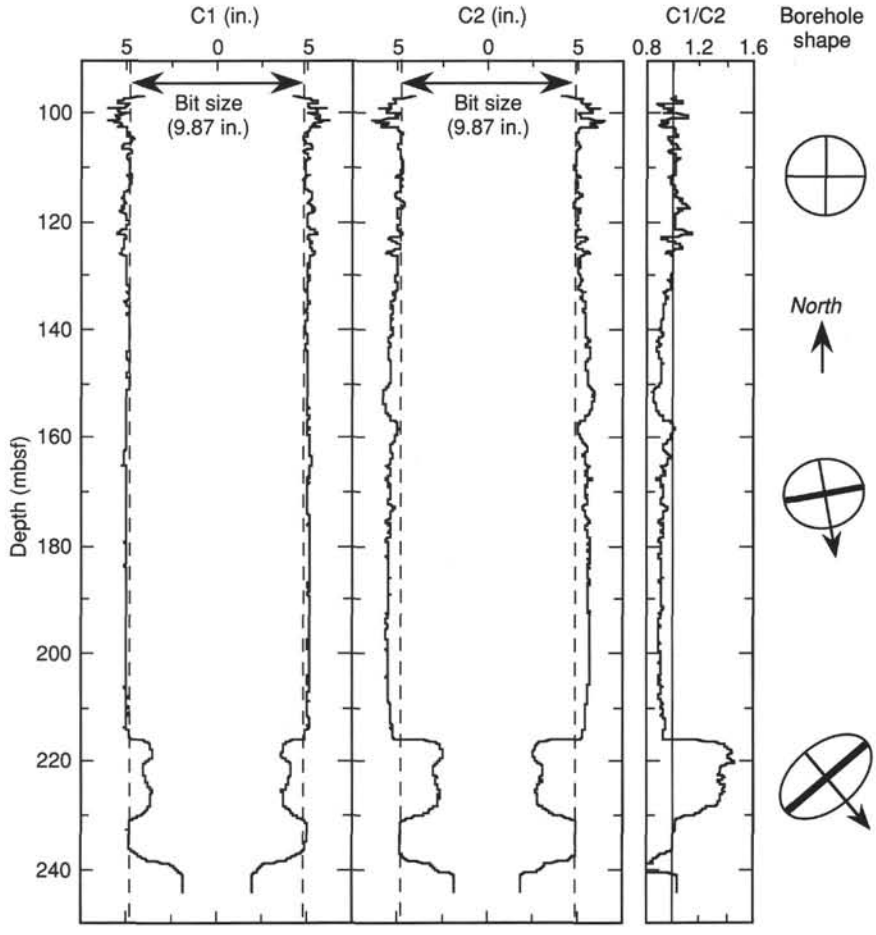

Figure 26. Caliper data (C1, C2) from the FMS tool for Hole 933A. The calipers have a maximum opening of 15 in. (38 cm). The ratio C1/C2 also is shown. True orientation of the average shape of the borehole cross section is shown on the right. (Arrow shows orientation of Pad 1.)

this chapter). Lithostratigraphic Unit III, a mass-flow deposit, is clearly delineated in the log data as an overconsolidated interval. There is an abrupt increase in resistivity, velocity, density, and magnetic susceptibility within the unit, and a marked decrease in neutron porosity (Fig. 23). FMS images also indicate sharp boundaries in resistivity and deformed strata. The upper part of Unit III (above 125 mbsf) has an overall lower radioactive mineral concentration, as indicated by gamma-ray response and lower electrical resistivity and velocity, suggesting relatively higher silt/sand content. Higher overall magnetic susceptibilities also may suggest a higher proportion of large magnetic grains. The FMS images also suggest that larger clasts occur above 125 mbsf. The downhole velocity gradient below 125 mbsf indicates different consolidation characteristics for the upper and lower sections of Unit III.

Below the mass-flow unit, logging responses in the interval between 164.5 and 180 mbsf suggest an overpressured formation. A sharp decrease in resistivity was observed, together with a subtle increase in porosity and a decrease in velocity and density. Similar characteristics are reported in the physical properties data. Borehole temperature measurements also indicate a marked increase in temperature, consistent with the expected response of an overpressured formation (Serra, 1986).

A pronounced separation is seen between shallow resistivity (SFLU) and medium and deep resistivities between 164 and 189 mbsf (Fig. 31). This separation indicates that the sediment and pore waters are more conductive proximal to the borehole wall (as measured by SFLU), in comparison to the relatively unaltered formation sensed by the deeper resistivity measurements, which may indicate shallow invasion of the formation by more conductive borehole fluid. In addition, a sharp change in resistivity occurs at about 192 mbsf (Fig. 31), although the other logging curves do not change (Fig. 23). The separation between the shallow and deeper resistivities suggests variations in the pore-fluid chemistry within the interval between 164 and 192 mbsf. Changes in pore-water chemistry were detected in the few samples analyzed within this interval (see "Inorganic Geochemistry" section, this chapter). The abrupt change in resistivity suggests anomalies exist in lithologic and pore-water chemistry that extend below the zone where overpressure can be detected from other geophysical logs.

CORE-SEISMIC INTEGRATION

Hole 933A penetrated through the Yellow Channel-levee System into a channel-levee system of the Bottom Levee Complex. Six seismic-facies units were identified on 3.5-kHz (Fig. 1) and water-gun seismic profiles (0232UTC on 10 April 1994 during Leg 155; Figs. 2 and 32). Seismic-facies Units 1 and 2 were classified using 3.5-kHz profiles, whereas seismic-facies Units 4 through 6 were classified from the water-gun profiles (Fig. 33). Five moderate-amplitude reflections mark the boundaries between seismic-facies units at 30, 65, 100, 130, and 210 ms.

Preliminary correlation was achieved between the seismic-facies units and the lithologic units by using the time vs. depth relationship determined at Site 931 (Fig. 33). Seismic-facies Unit 1 (0 to 30 ms) is characterized by high-amplitude continuous parallel reflections returned from sediment laterally equivalent to the Amazon and Blue Channel-levee systems, as well as sediment in the upper part of the

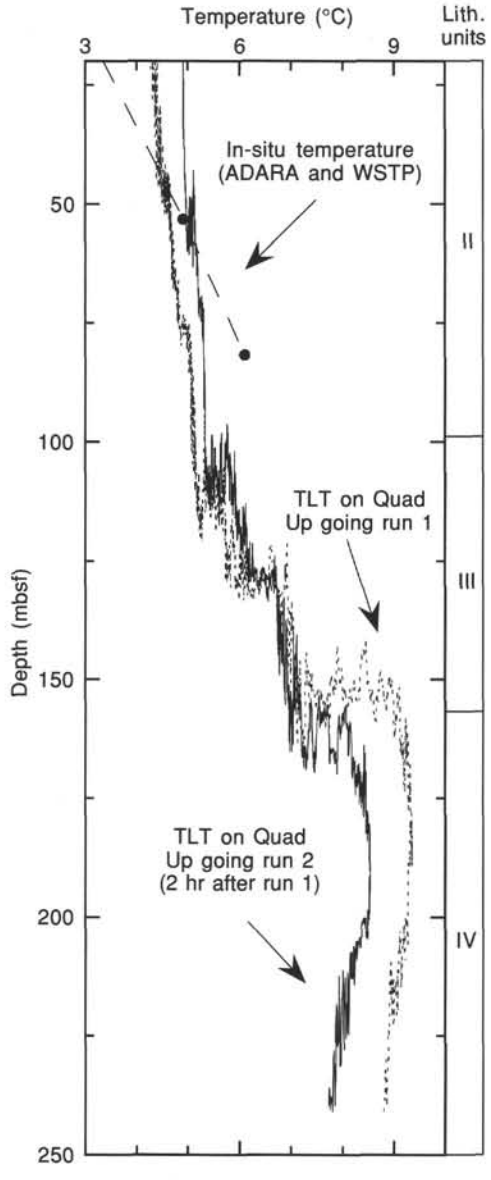

Figure 27. Borehole temperature logs for Hole 933A. A delay of 2 hr occurred between the two runs. There is a marked increase in temperature below lithostratigraphic Unit III.

Yellow Channel-levee System. This seismic-facies unit also shows high-amplitude acoustic artifacts apparently caused by focusing of the acoustic energy by the irregular seafloor (Fig. 1). Seismic-facies Unit 1 correlates with lithologic Unit I, Subunit IIA, and the upper 6 m of Subunit IIB. Seismic-facies Unit 2 (30–65 ms) exhibits low-amplitude discontinuous, divergent reflections plus regular migrating reflections plus the base of the unit (Fig. 1). Seismic-facies Unit 2 apparently correlates with the upper portion of lithologic Subunit IIB (22–50 mbsf); the reflections are probably returned from the silt and sand turbidites interbedded within the hemipelagic sediment.

Low-amplitude discontinuous divergent reflections characterize seismic-facies Unit 3 (65–100 ms), which can be correlated with the lower section of Subunit IIB (50 to 75 mbsf). Subunit IIB is composed of turbidites within the flank of the Yellow Channel-levee System. Seismic-facies Unit 4 is characterized by two very high-amplitude, continuous parallel reflections between 100 and 130 ms and represents overbank sediment of Channel-levee Systems 5, 6A,

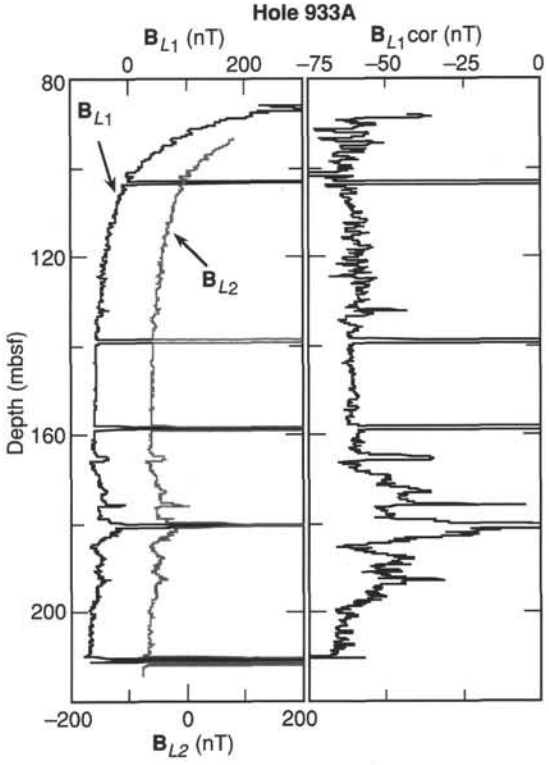

Figure 28. "Local" total magnetic induction for the two logging runs ($\mathbf{B}_{L1}$ and $\mathbf{B}_{L2}$) and the resulting $\mathbf{B}_L$ after correction for pipe effect of first run ($\mathbf{B}_{L1}$cor). Part of the total induction has been obtained by correcting the total induction for the main dipolar field; scale shift between runs is 100 nT.

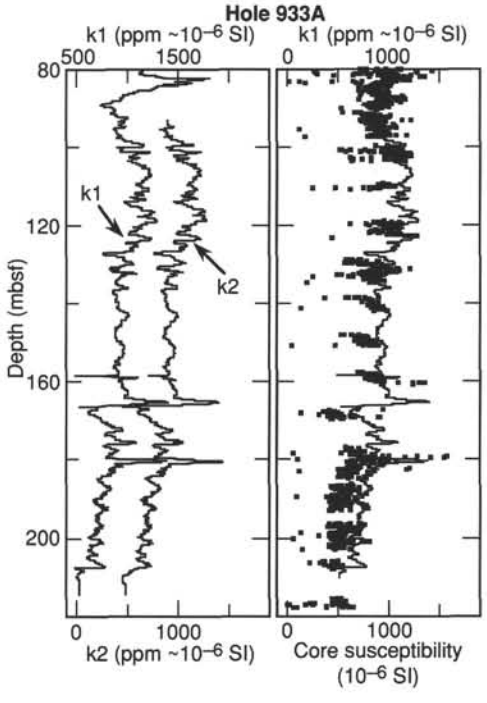

Figure 29. Downhole magnetic susceptibility (left; two runs: k1, k2). Comparison (right) of logging magnetic susceptibility (k1, solid line) with MST core susceptibility (squares).

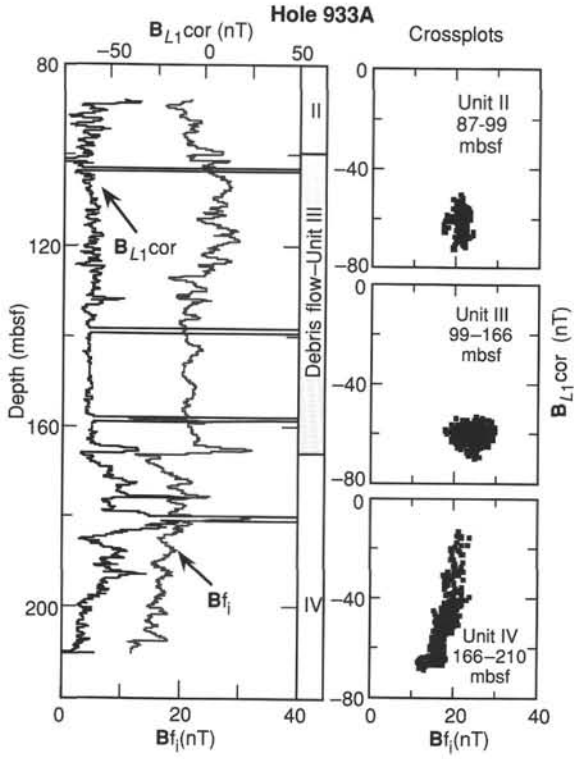

Figure 30. "Local" total induction (left) after correction for pipe effect ($\mathbf{B}_{L1}$cor) and downhole induction ($\mathbf{Bf}_i$) calculated from susceptibility (k1; Fig. 29). Crossplots of $\mathbf{B}_{L1}$cor vs. $\mathbf{Bf}_i$ for the intervals that span lithostratigraphic Units II, III, and IV are shown at right.

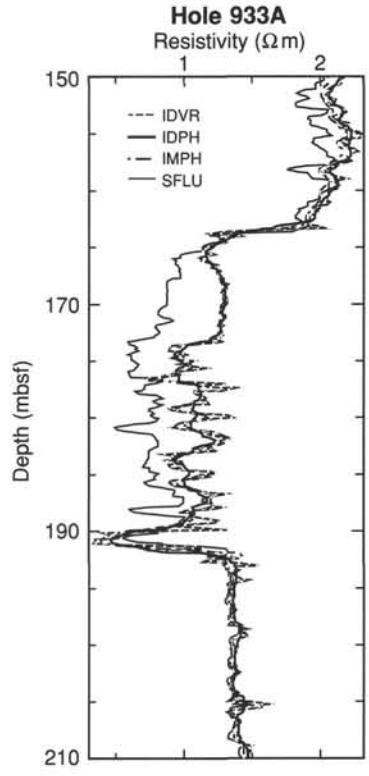

Figure 31. Resistivity logs reveal an anomalous interval between 164 and 192 mbsf, characterized by separation between the shallow, spherically focused resistivity (SFLU) and the deeper penetrating medium (IMPH), deep (IDPH), and enhanced-resolution deep-phasor induction (IDVR) resistivity. This suggests that invasion of the formation by borehole seawater has lowered the conductivity of the formation, which probably contains fresher and less conductive interstitial water.

and 6B. Seismic-facies Units 5 and 6 can be correlated with lithologic Units III and IV, respectively. A good correlation exists between the hummocky to chaotic reflections of seismic-facies Unit 5 and the debris-flow deposits of lithologic Unit III. Prominent reflections occur at both the top and bottom of seismic-facies Unit 5. The subparallel irregular to hummocky reflections characteristic of seismic-facies Unit 6 appear to originate from the turbidite deposits of lithologic Unit IV.

Synthetic Seismogram

A synthetic seismogram was generated using the two-way traveltime from the seafloor to the first log data (55 mbsf) using an average constant velocity of 1540 m/s for this interval (Fig. 34). The synthetic seismogram shows the locations of prominent reflections at the top and bottom of seismic-facies Unit 5. The complex nature of the source signature precludes direct comparison to the reflection at the base of seismic-facies Unit 5; however, the reflection coefficient shows a negative contrast at that level, and indicates a polarity reversal.

IN-SITU TEMPERATURE MEASUREMENTS

Temperature gradients and heat flow were determined using two downhole measurements and the bottom-water (mud-line) temperature. Two ADARA measurements were made during Cores 933A-6H (53.2 mbsf) and -9H (81.7 mbsf) using instrument number 12. The mud-line temperature of 2.40°C measured from this instrument was used as the reference bottom-seawater temperature at Site 933. Successful measurements resulted in extrapolated equilibrium temperatures of 4.91°C at 53.2 mbsf, and 6.11° at 81.7 mbsf.

Equilibrium temperatures, extrapolated from synthetic curves constructed to fit transient temperature data, are plotted as a function of depth (mbsf) in Figure 35. Using the ADARA mud-line temperature, and the sub-bottom temperatures from the two ADARA measurements downhole, the geothermal temperature gradient can be approximated by a linear mean of 45.6°C/km. We calculated heat flow by adopting the constant geothermal temperature gradient of 45.6°C/km and a linear increase in thermal conductivity, K, of 1.1 ± 0.15 W/(m·K), which is an average of regression estimates at 80 mbsf. This results in a calculated heat flow of 50.2 mW/m^2.

SYNTHESIS AND SIGNIFICANCE

Stratigraphic Synthesis

Surficial Nannofossil-rich Clay (Unit I)

Surficial sediment consists of Holocene brown calcareous clay (0.52 m thick) containing foraminifers and nannofossils (Fig. 36) overlying a brown diagenetic crust.

Mud Equivalent to the Amazon to Blue Channel-levee Systems (Subunit IIA)

Subunit IIA (0.52–14.35 mbsf) consists of moderately bioturbated or color-banded mud and lithologically resembles Subunit IIA of Sites 930 and 931.

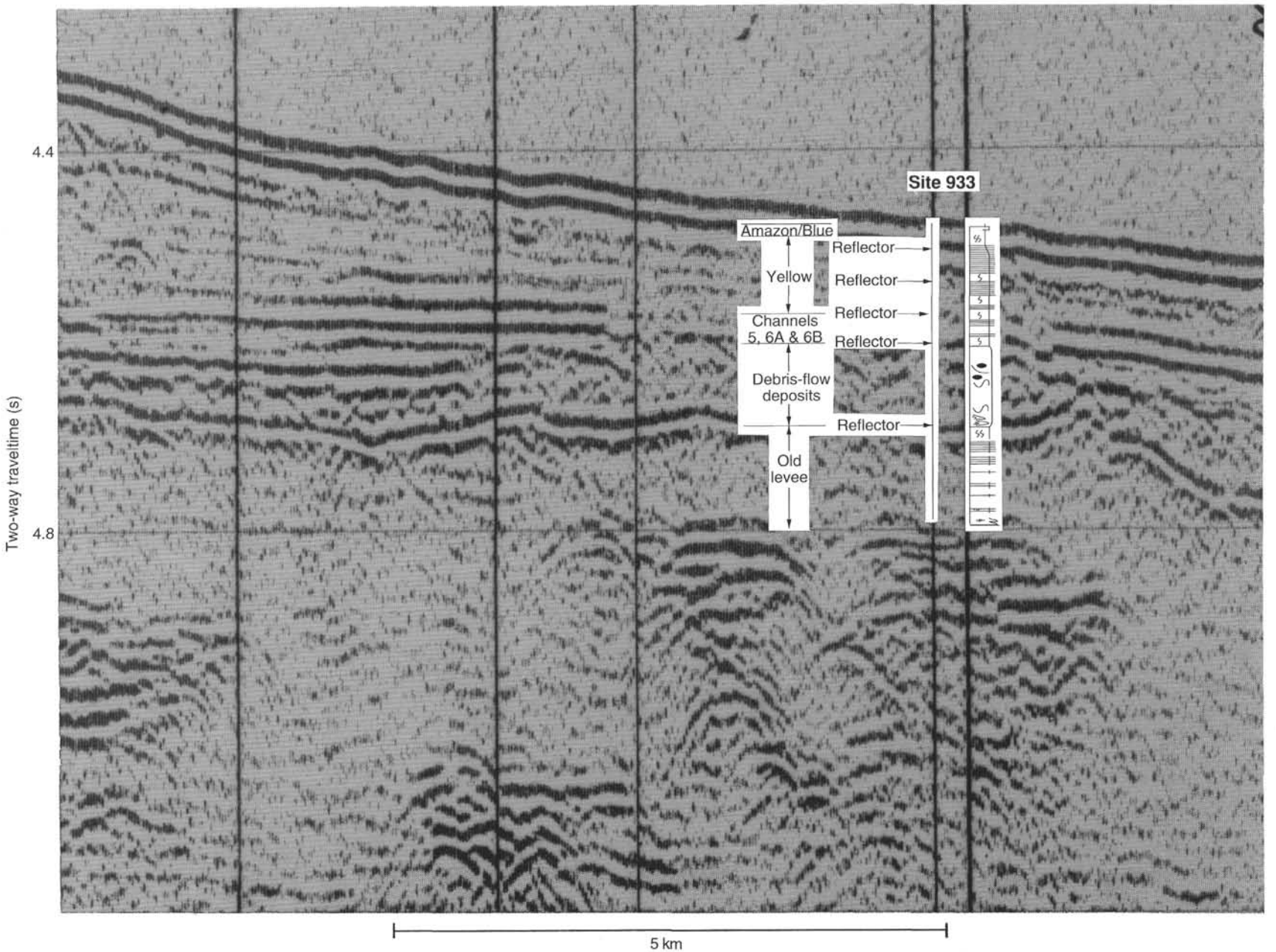

Figure 32. Seismic-reflection profile showing Site 933 with the corresponding lithostratigraphic section for Hole 933A. Location of profile shown in Fig. 1 of the "Site 931" chapter, this volume (c.f. Fig. 2A).

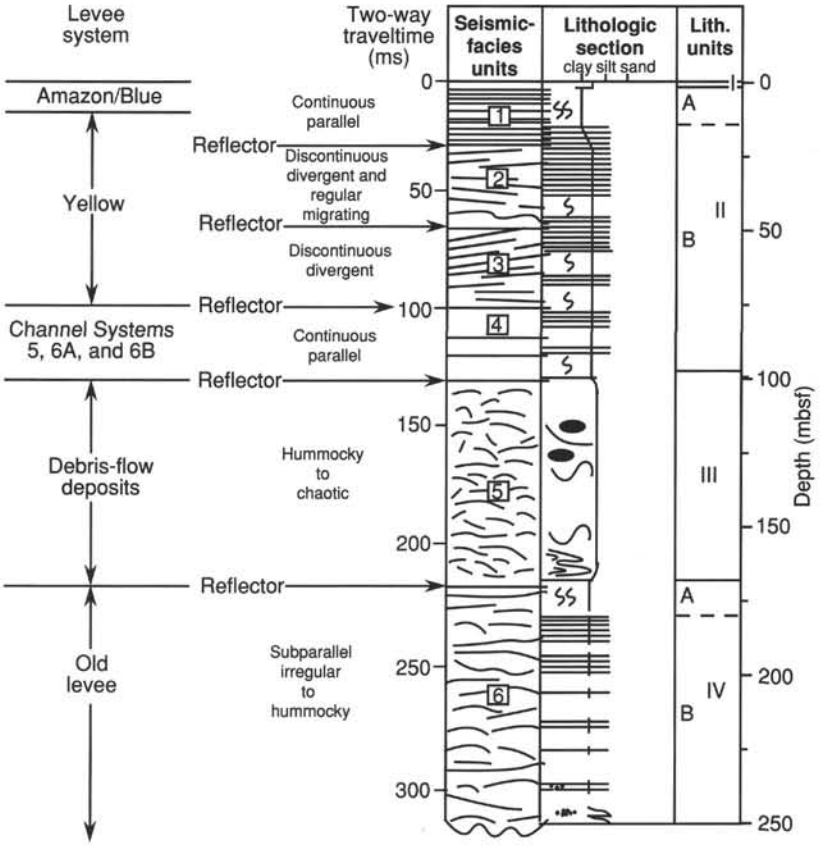

Figure 33. Correlation of lithostratigraphic observations with seismic-facies units and prominent reflections (arrows) at Site 933.

Levee Flank of the Yellow Channel-levee System (Upper Part of Subunit IIB)

The upper part of Subunit IIB (14.35 to about 70 mbsf) corresponds to the levee flank of the Yellow Channel-levee System, about 7 km from the channel, and comprises mud with thin to medium beds of silt and fine sand. Several zones with abundant silt and sand alternate with thinner intervals (3–8 m thick) of moderately bioturbated mud with few silt laminae. At 60–64 mbsf a massive black clay contains abundant plant detritus, shell fragments, upper- to mid-bathyal benthic foraminifers, and rounded quartz sand grains.

Stratigraphic Interval of Channel-levee Systems 5 and 6 (Lower Part of Subunit IIB)

In the lower part of Subunit IIB, sediment from about 70 to 83 mbsf consists of mud with thin beds of silt and sand that are most abundant at the base of this sequence. This interval corresponds to the distal levee flank of Channel-levee System 5, about 20 km from the channel. From about 83 mbsf to 97.62 mbsf, the sediment consists of slightly bioturbated and color-mottled mud with minor silt laminae. This interval corresponds to Channel-levee System 6 and is about 20 km from the channel.

Mass-flow Deposit (Unit III)

Unit III (99.80–167.31 mbsf) consists of various types of mud, apparently as discrete blocks and commonly showing deformational structures. The unit is interpreted as a mass-transport deposit. Wet-bulk density increases downhole, with values elevated above the "normal" consolidation effects defined by Units II and IV, suggesting that Unit III is made up principally of overconsolidated blocks.

Wireline log data suggest that Unit III can be divided into two parts, above and below 125 mbsf. There is a downhole decrease in magnetic susceptibility and an increase in natural gamma-ray emission, sonic velocity, and density at 125 mbsf. The FMS log indicates larger blocks above this level and smaller clasts below. The lower part of the unit contains *P. obliquiloculata, G. tumida,* and rare *G. menardii,* which are absent in the upper part of the unit. Benthic foraminifers of an upper bathyal assemblage occur throughout the unit and suggest that the sediment was derived from the continental slope. Chlorinity levels in the lower part of Unit III and in Unit IVA are low (around 550 mM) compared with most of the section (around 560 mM) and are similar to the typical interglacial values of Holocene Unit I. Pore-water sulfate (in concentrations of 1–2 mM) is also found in the lower part of Unit III. Total nitrogen, which averages 1.0% to 1.2% in Unit II, drops to 0.06–0.08 in Unit III, with a low [C/N]a. Taken together, these data suggest that the lower part of the mass-flow unit was derived from more deeply buried slope sediment that accumulated during a period of relatively warm climate, whereas the upper part was derived from less-consolidated glacial stage sediment.

Top of Bottom Levee Complex (Unit IV)

Unit IV (167.31–249.72 mbsf) consists of a sequence similar to Subunits IIA and IIB, with moderately bioturbated or color-banded mud (Subunit IVA, to 179.03 mbsf) overlying mud with silt laminae (Subunit IVB). At the top of Section 933A-19X-1, 11 cm of dark mud, which may have fallen down the hole, contains more abundant foraminifers than any other samples in this unit.

Implications

The Lake Mungo paleomagnetic excursion (30 ka) was observed at 81.5 mbsf. The $Y_{P.\ obliq.}$ marker (40 ka) was not found in the site.

Unit IVA has a warm-water planktonic assemblage, including *G. tumida,* but lacking *G. menardii*. The absence of *P. lacunosa* and *E. huxleyi* constrains the age to 0.26 to 0.46 Ma. Unit IV at Site 933 is

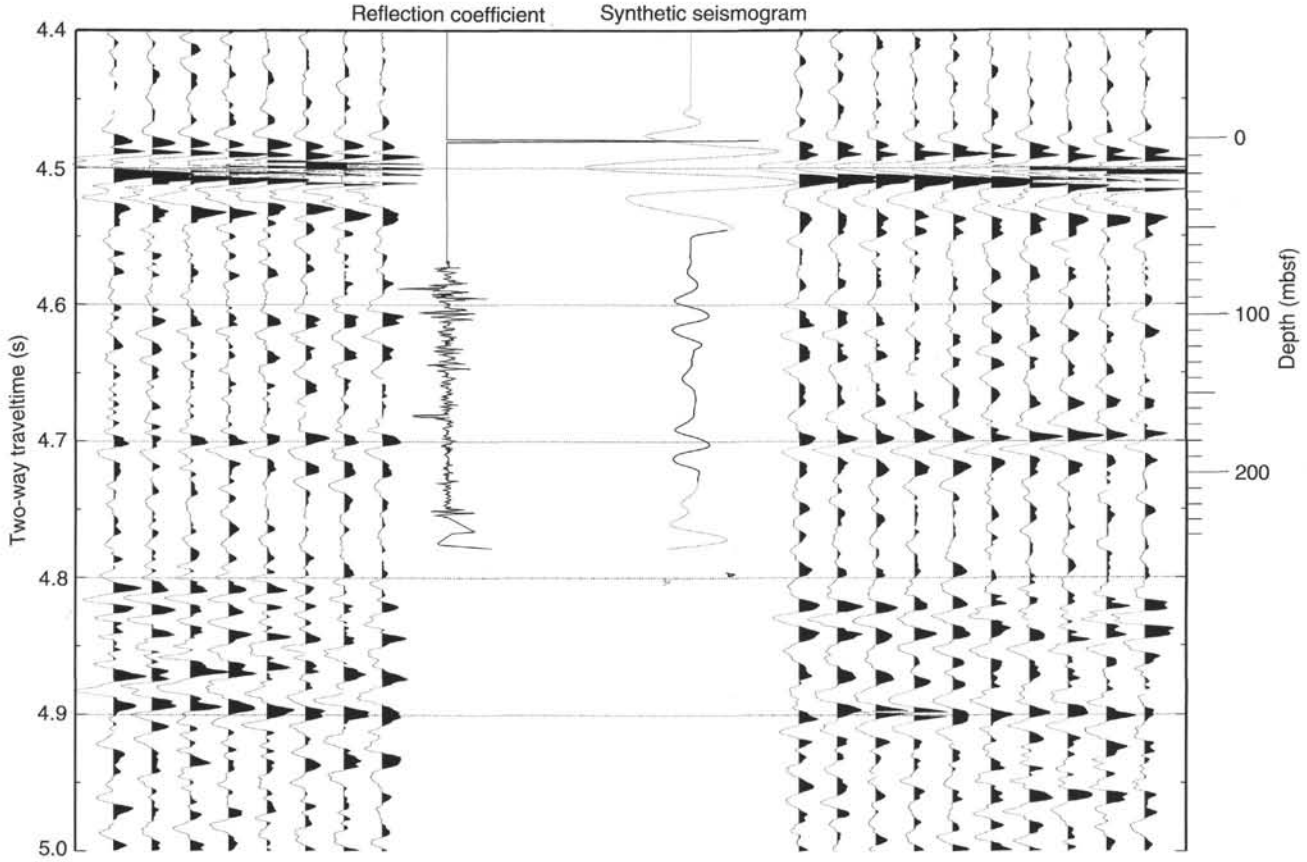

Figure 34. Synthetic seismogram for Site 933. Solid portion of synthetic seismogram curve calculated from log data, dotted portion calculated from physical property data and log extrapolation.

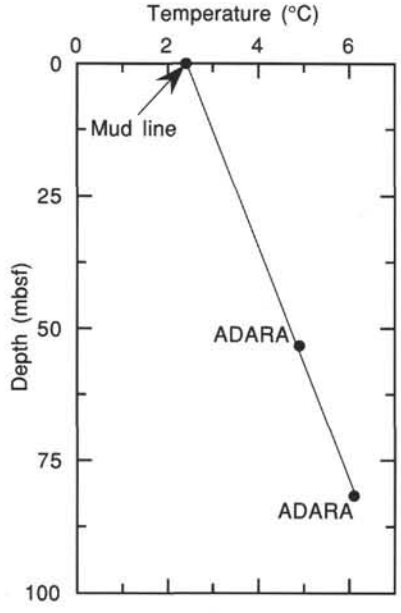

Figure 35. Estimated equilibrium temperatures in Hole 933A. A linear curve fit through the data suggests that reliable equilibrium temperatures were acquired that indicate a geothermal gradient of 45.63°C/km.

thus correlated with Unit V at Site 931 on the basis of seismic-reflection continuity and similar lithology and biostratigraphy, and is assigned a probable age of 0.26 to 0.46 Ma.

As at Site 932, downhole variations in mud mineralogy (determined by XRD) show much scatter. Clay mineral content (relative to quartz) is higher in the mass-transport deposit (Unit III). Kaolinite/smectite ratio is higher in Unit IV than elsewhere in the hole.

Many of the sedimentological features of this site confirm observations made at earlier sites. The levee of the Bottom Levee Complex shows an overall fining-upward sequence. In contrast, the younger levee deposits of Unit II show multiple cycles, marked by intervals with many turbidite sand and silt beds alternating with bioturbated, predominantly muddy intervals. In the deeper part of Unit II, these changes can be related to distance from the active channel. The deposits equivalent to Channel-levee System 5 show an overall fining- and thinning-upward sequence; however, the more proximal deposits of the Yellow levee include several alternations of turbidite-silt packets with more muddy sequences, suggesting some allocyclic control of turbidite deposition. In general, the levee flank turbidite sand of Unit II includes common cross-lamination (approximately 20% of sand beds), compared with an apparent absence of cross-lamination in levee-crest turbidite sand of Subunit IVB.

The sedimentological character of the mass-flow deposit is difficult to discern and will require further shore-based work, especially on the FMS log data. The lower part of Unit III includes inferred tilted blocks in cores, and the FMS log data suggest the presence of small blocks and deformed strata. Evidence of a significant debris-flow matrix is lacking. Blocks in the upper part of the unit appear to be a few meters thick and less obviously tilted. They may represent slide deposits.

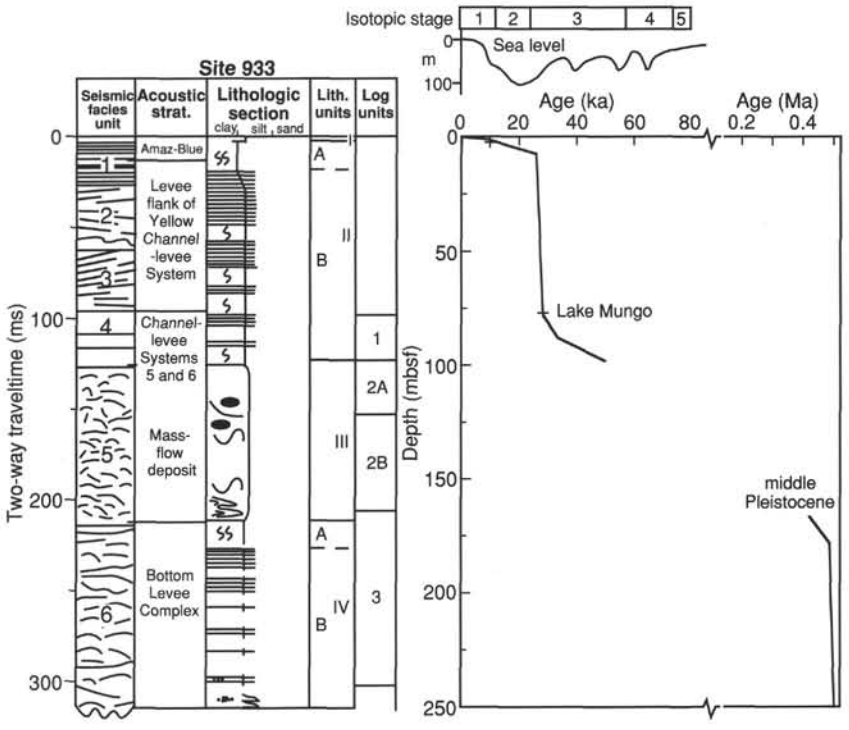

Figure 36. Summary of Site 933 showing seismic-facies units, acoustic stratigraphy, schematic lithologic column, lithologic units, chronological picks, and interpreted age-depth curve.

The massive black clay containing abundant plant and shell fragments at 60–64 mbsf differs from other minor mass-transport deposits on levees (e.g., at 40 and 125 mbsf at Site 932) in that it appears to have an upper slope provenance rather than being derived by local levee failure.

Unit IV sediment has a higher water content than would be expected under normal consolidation, suggesting that dewatering has been inhibited. A pronounced reduction in the size of the borehole at 215 mbsf, with a marked elliptical cross-section, corresponds to an abrupt decrease in wet-bulk density from 2.0 to 1.9 g/cm^3 and changes in water content and porosity, indicating an overpressured formation. Above this interval, the upper part of Unit IV shows a 1.3°C positive temperature anomaly during logging (200–170 mbsf; TLT), together with anomalously low log resistivity values (167–192 mbsf) and elevated interstitial-water concentrations for several chemical species, particularly alkalinity and phosphate. This may suggest that either formation water has been trapped beneath the less permeable debris flow, or that flow of slightly deeper formation water is occurring along the top of the Bottom Levee Complex.

REFERENCES*

Damuth, J.E., 1977. Late Quaternary sedimentation in the western equatorial Atlantic. *Geol. Soc. Am. Bull.*, 88:695–710.

Manley, P.L., and Flood, R.D., 1988. Cyclic sediment deposition within Amazon deep-sea fan. *AAPG Bull.*, 72:912–925.

Schlumberger, 1989. *Log Interpretation Principles/Applications:* Houston, TX (Schlumberger Educ. Services).

Serra, O., 1986. *Fundamentals of Well-Log Interpretation* (Vol. 2): *The Interpretation of Logging Data:* Amsterdam (Elsevier).

*Abbreviations for names of organizations and publications in ODP reference lists follow the style given in *Chemical Abstracts Service Source Index* (published by American Chemical Society)

Ms 155IR-109

NOTE: For all sites drilled, core-description forms ("barrel sheets") and core photographs can be found in Section 4, beginning on page 703. Forms containing smear-slide data can be found in Section 5, beginning on page 1199. GRAPE, index property, magnetic susceptibility, and natural gamma data are presented on CD-ROM (back pocket).

SHORE-BASED LOG PROCESSING

HOLE 933A

Bottom felt: 3376.8 mbrf
Total penetration: 254.2 mbsf
Total core recovered: 177.38 m (69.8%)

Logging Runs

Logging string 1: DIT/LSS/HLDT/CNTG/NGT
Logging string 2: FMS/GPIT/NGT (pass 1, pass 2–top, pass 2–bottom)
Logging string 3: GHMT/NGT (two passes)
Wireline heave compensator was used to counter ship heave.

Bottom-hole Assembly

The following bottom-hole assembly depths are as they appear on the logs after differential depth shift (see **Depth shift** section below) and depth shift to the seafloor. As such, there may be a discrepancy with the original depths given by the drillers on board. Possible reasons for depth discrepancies are ship heave, use of wireline heave compensator, and drill-string and/or wireline stretch.

DIT/LSS/HLDT/CNTG/NGT: Bottom-hole assembly at 67 mbsf.
FMS/GPIT/NGT: All passes recorded open hole.
GHMT/NGT: Both passes recorded open hole.

Processing

Depth shift: The NGT (SGR curve) from the FMS passes correlated very poorly with the SGR from the reference run (DIT/LSS/HLDT/CNTG/NGT). Therefore, FMS pass 1 was correlated to FMS pass 2–top using the caliper; then both depth-shifted FMS pass 1 and FMS pass 2–top were depth shifted with reference to DIT/SDT/HLDT/CNTG/NGT, using SGR for correlation. Finally, FMS pass 2–bottom was correlated to the depth-shifted FMS pass 1 using SGR, and the DIT/LSS/HLDT/CNTG/NGT repeat run was correlated to DIT/HLDT/CNTG/NGT main pass using resistivity. The second pass of the GHMT logs has been first depth-shifted to match the first pass, using the susceptibility curves for correlation. Both passes then were depth shifted with reference to the main DIT/LSS/HLDT/CNTG/NGT pass, using the NGT for correlation. The match, however, is generally poor, due to the different NGT signature. All logs have then been depth shifted to the seafloor as detected by the NGT (–3376 m). A list of the amount of differential depth shifts applied at this hole is available upon request.

Gamma-ray processing: NGT data have been processed to correct for borehole size and type of drilling fluid.

Acoustic data processing: The sonic logs have been processed to eliminate some of the noise and cycle skipping experienced during the recording.

Quality Control

During the processing, quality control of the data is mainly performed by cross-correlation of all logging data. Large (>12 in.) and/or irregular borehole affects most recordings, particularly those that require eccentralization and a good contact with the borehole wall (CNTG, HLDT).

Hole diameter was recorded by the hydraulic caliper on the HLDT tool (CALI), and the caliper on the FMS string (C1 and C2). The HLDT caliper, however, did not work properly during the main pass in the lower 145 m of the hole. For this reason, both caliper and density data have been spliced with the data from the repeat run, during which the caliper worked properly, allowing for an appropriate correction of the density data. The high density data have also been spliced.

Data recorded through the bottom-hole assembly, such as the CNTG and NGT data above 67 mbsf, should be used only qualitatively because of the attenuation on the incoming signal.

Note: Details of standard shore-based processing procedures are found in the "Explanatory Notes" chapter, this volume. For further information about the logs, please contact:

Cristina Broglia
Phone: 914-365-8343
Fax: 914-365-3182
Email: chris@ldeo.columbia.edu

Elizabeth Pratson
Phone: 914-365-8313
Fax: 914-365-3182
Email: beth@ldeo.columbia.edu

933A Natural Gamma Ray-Density-Porosity Logging Data

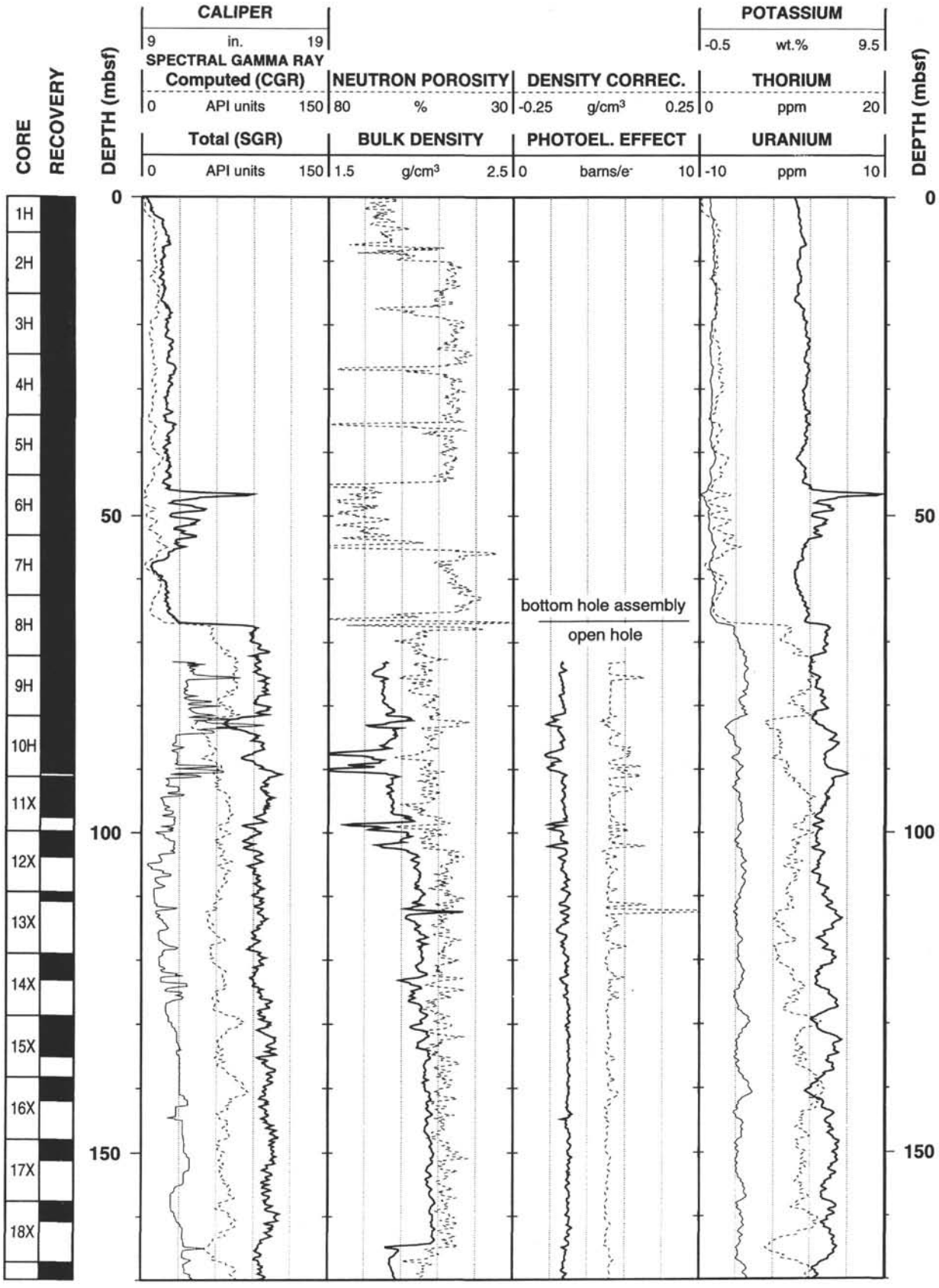

933A Natural Gamma Ray-Density-Porosity Logging Data (cont.)

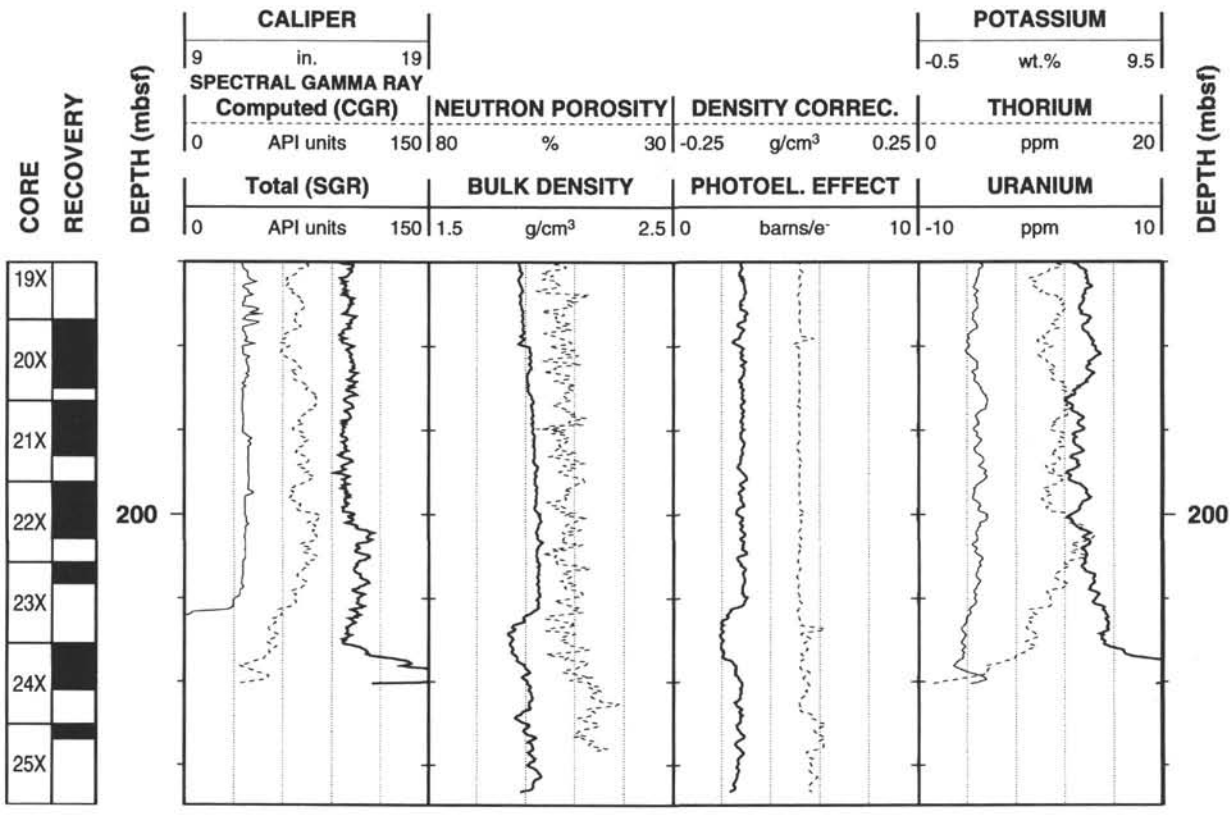

933A Natural Gamma Ray-Resistivity-Velocity Logging Data

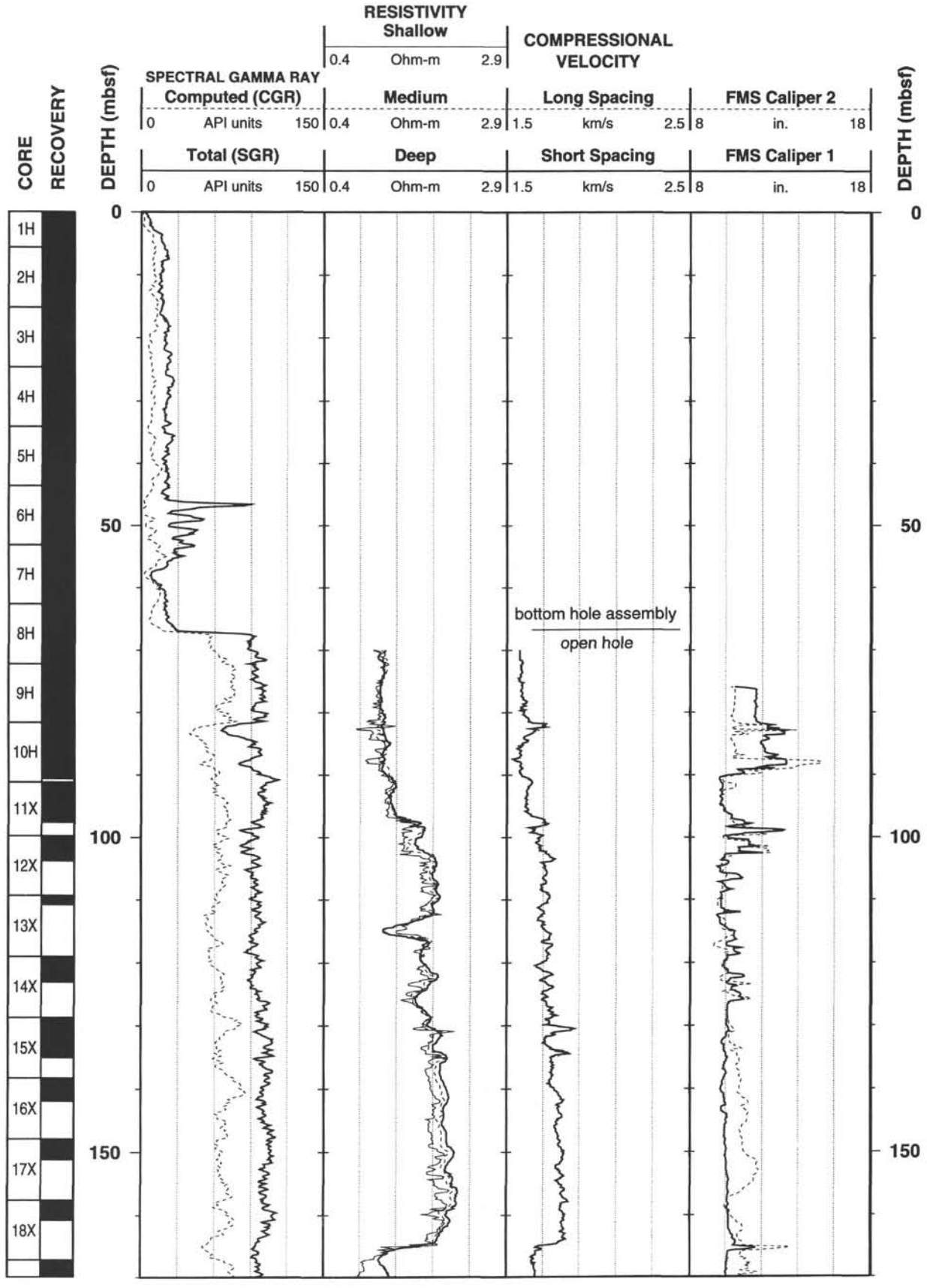

933A Natural Gamma Ray-Resistivity-Velocity Logging Data (cont.)